BUILDING AND CHARACTERIZING GRAPHENE NANOMECHANCIAL RESONATOR NETWORKS

by

BRITTANY ELIZABETH CARTER

A DISSERTATION

Presented to the Department of Physics
and the Division of Graduate Studies of the University of Oregon
in partial fulfillment of the requirements
for the degree of
Doctor of Philosophy

June 2023

DISSERTATION APPROVAL PAGE

Student: Brittany Elizabeth Carter

Title: Building and Characterizing Graphene Nanomechanical Resonator Networks

This dissertation has been accepted and approved in partial fulfillment of the requirements for the Doctor of Philosophy degree in the Department of Physics by:

Jayson Paulose	Chairperson
Benjamín Alemán	Advisor
Hailin Wang	Core Member
Mark Lonergan	Institutional Representative

and

Krista Chronister	Vice Provost for Graduate Studies

Original approval signatures are on file with the University of Oregon Division of Graduate Studies.

Degree awarded June 2023

© 2023 Brittany Elizabeth Carter
This work is licensed under a Creative Commons
Attribution-NonCommercial-NoDerivs (United States) License.

DISSERTATION ABSTRACT

Brittany Elizabeth Carter

Doctor of Philosophy

Department of Physics

June 2023

Title: Building and Characterizing Graphene Nanomechanical Resonator Networks

Networks of nanoelectromechanical (NEMS) resonators are useful analogs for a variety of many-body systems and enable impactful applications in sensing, phononics, and mechanical information processing. Two main challenges are currently limiting progress toward realizing practical NEMS networks. The first is building a platform of interconnected resonators that is scalable in both size and tunability. The second is spatially quantifying the mechanical parameters of each resonator in the network and their coupling. In this work, we address these two main challenges with a novel scalable platform to build the network and a compatible method to characterize mechanical parameters. Together, this work fills in a vital gap for the experimental realization of programmable NEMS networks.

We first present a novel platform of suspended graphene resonators that hosts strong coupling and is scalable in 2D. In this platform, we suspended graphene over pillar arrays, in which large areas of suspended graphene act as drumhead resonators and shared membrane between adjacent resonators allows for direct coupling through strain. We demonstrate the versatility advantages of our graphene-based resonator network by providing evidence of strong coupling through two different tuning methods. We demonstrate the 2D scalability potential of this platform with evidence of coupling between three resonators. Finally, we show noteworthy coupling dynamics of inter-resonator higher order mode coupling that is enabled by our versatile platform.

We then demonstrate a scalable optical technique to spatially characterize graphene NEMS network. In this technique, we read out the fixed-frequency collective response as a single vector. Using just two response vectors, we solve for the site-specific elasticity, mass, damping, and coupling parameters of network clusters. Compared to multiple regression, our algebraic fully characterizes the network parameters without requiring *a priori* parameter estimates or iterative computation. We apply this technique to single-resonator and coupled-pair clusters and find excellent agreement with expected parameter values and spectral response. Our approach offers a direct means to accurately characterize both classical and quantum resonator systems.

CURRICULUM VITAE

NAME OF AUTHOR: Brittany Elizabeth Carter

GRADUATE AND UNDERGRADUATE SCHOOLS ATTENDED:

University of Oregon, Eugene, OR
Boston College, Chestnut Hill, MA

DEGREES AWARDED:

Doctor of Philosophy, Physics, 2023, University of Oregon
Master of Science, Physics, 2019, University of Oregon
Bachelor of Science, Physics, 2017, Boston College

AREAS OF SPECIAL INTEREST:

Nanotechnology
Nanofabrication
Nanoelectromechanical Systems (NEMS)
Metrology and optics

PROFESSIONAL EXPERIENCE:

Graduate Research Assistant, Alemán Lab, University of Oregon, 2021-2023
Graduate Teaching Fellow, Department of Physics, University of Oregon. 2017-2021

GRANTS, AWARDS, AND HONORS:

Weiser Senior Teaching Award, University of Oregon, 2020

PUBLICATIONS:

Miller, D., Blaikie, A., Carter, B. & Aleman, B. Engineering the Modal Shape of Graphene Nanoelectromechanical Systems Using Focused Ion Beam Milling. *2018 IEEE 13th Nanotechnol. Mater. Devices Conf.* 1–4 (2018)

Carter, B., Horowitz, V. R., Hernandez, U., Miller, D. J., Blaikie, A., and Alemán, B. J., "Spatial mapping and analysis of graphene nanomechanical resonator networks". *ArXiv* (2023) doi:10.48550/arXiv.2302.03680.

ACKNOWLEDGMENTS

I first and foremost would like to thank my advisor Benjamín Alemán. I appreciate all you have done to support me in becoming an independent researcher. In the lab, you have given me guidance on how to formulate research questions, design efficient experiments, and effectively communicate my science to every type of audience. Outside of the lab, you have helped me cultivate my own confidence and now I can truly see myself as a scientist.

I would like to express my deepest appreciation to my parents and my sister, Chelsey. Thank you for providing me with every type of support imaginable. Thank you for listening to me for hours over the phone through the good and the bad, for visiting me across the country, for helping me work my way out of any situation, and for all the dog photos and sunsets. Thank you for doing everything you could to ensure my success, I truly would not be where I am today without each of you.

In the Alemán Lab, I have met friends who have also become my most valued mentors. To Kara Zappitelli, thank you for teaching me how to survive graduate school, for taking me on my first backpacking trip and for the many adventures after that, and for always having the best advice. To David Miller, thank you for the mentorship as I joined the lab and worked through designing a project. And thank you for all the support and career advice you have continued to provide to me over the years.

Through my cohort, I have met many lifelong friends. To Amy Turner, thank you for the late nights of Gilmore Girls, the backpacking adventures, and Morning Glory breakfasts. To Rachael Klaiss, thank you for always being willing to listen and for your openness in return. And to Deepika Sundarraman, thank you for helping me through some of the most difficult situations.

Finally, I would like to thank the many others who have always provided me with encouragement and accompanied me on adventures to keep me grounded. An enormous thank you to Cody Titus, Stacy Levichev, Nick Cady, Lucy Barton, and Justin Kittell and many others for the rock climbs, ski trips, mountain hikes, board games, marathons, bike rides, and trail runs. Thank you all for making Oregon feel like home.

To Mom, Dad, and Chelsey.

Thank you for your endless support.

TABLE OF CONTENTS

1 Introduction 12

1.1 Background of many-body systems 12

1.2 Coupled NEMS resonators as a model system for many-body physics 12

1.3 Graphene NEMS resonators 14

1.4 Characterizing graphene NEMS resonators 15

1.5 Outline thesis chapters 16

2 Theoretical background 18

2.1 Infinite chain of masses and springs 18

2.2 Single resonator 19

2.3 Two coupled resonators 22

2.4 Single graphene resonators modeled as mass and springs 25

3 Experimental methods 28

3.1 Fabrication of device platforms 28

3.2 Wet transfer method of graphene 31

3.3 Actuation and tuning of graphene resonators 32

3.4 Interference measurement of amplitude and phase and SIM 34

3.5 Phase lag in measurements 36

4 Novel platform for coupled NEMS resonator networks 38

4.1 Introduction 38

4.2 Methods 39

4.3 Results 41

4.4 Discussion 47

4.5 Conclusion 48

5 Characterization of coupled NEMS resonator networks 49

5.1 Introduction 49

5.2 Mathematical background 50

5.3 Methods 51

5.4 Results for resonator clusters of size $N = 1$ 54

5.5 Results for resonator clusters of size $N = 2$ 59

5.6 Discussion 65

5.7 Conclusion 67

6 Conclusion 69

6.1 Remarks regarding future directions 69

6.2 Resolution 69

Appendices 71

APPENDIX A: Resonance frequency dependence on drumhead size 71

APPENDIX B: Error distributions of NetMAP parameters 72

APPENDIX C: Supplementary information regarding NetMAP evaluation 74

References 79

LIST OF FIGURES

Figure 1.1 Suspended graphene drumhead resonator 15
Figure 2.1 Linear mass and spring infinite chain model....................18
Figure 2.2: Single resonator cluster 19
Figure 2.3: Simulated amplitude and phase of single drive damped resonator 21
Figure 2.4: Two coupled resonator model 22
Figure 2.5: Simulation of amplitude and phase curves of two coupled resonators 23
Figure 2.6: Simulated amplitude spectra for range of coupling strengths 24
Figure 2.7: Simulated avoided crossing spectrographs 25
Figure 2.8: Mode shapes of vibrating circular plate 27
Figure 3.1: Substrate fabrication process flows....................28
Figure 3.2: Images of completed fabricated sample 30
Figure 3.3: Graphene transfer process flow....................31
Figure 3.4: Electrical actuating of suspended graphene and equivalent circuit....................32
Figure 3.5: Tuning response of graphene resonator to applied electrical DC bias 34
Figure 3.6: Optical pump/probe measurement schematic....................36
Figure 3.7: Experimental phase lag 37
Figure 4.1: Design and fabrication of suspended graphene resonators 39
Figure 4.2: SEM images of suspended graphene on pillar arrays....................40
Figure 4.3: Strong coupling between two suspended graphene resonators 41
Figure 4.4: Strong coupling between additional set of two resonators....................43
Figure 4.5: Coupling between three resonators 44
Figure 4.6: Simulated spectra from three coupled resonator model....................45
Figure 4.7: Inter-resonator higher order mode coupling....................46
Figure 5.1: Suspended graphene platform and measurement scheme 52
Figure 5.2: NetMAP analysis of first $\mathrm{N} = 1$ cluster....................55
Figure 5.3: Netmap analysis of second $N = 1$ cluster....................58
Figure 5.4: NetMAP analysis of first $N = 2$ cluster....................60
Figure 5.5: NetMAP analysis of second $N = 2$ cluster 64

LIST OF TABLES

Table 5.1: First set of normalized values of p from NetMAP and Unity LS for $N = 1$ Cluster 56
Table 5.2: Results for additional $N = 1$ cluster from NetMAP and Unity LS 59
Table 5.3: Normalized values of p from NetMAP and Unity LS for $N = 2$ cluster 62
Table 5.4: Normalized values of p from NetMAP and Unity LS for second $N = 2$ cluster 65

1 Introduction

1.1 Background of many-body systems

Coupled resonators are abundant in both nature and technology; existing in many different forms from multiple strings vibrating on a guitar to rhythmic applause at a concert hall[1]. Coupled resonators operate on the principle that if there is a medium connecting two or more oscillators, such as the neck of a guitar, then the oscillators can exchange energy. When coupling is present, and energy is transferred between resonators, specific amplitude and phase patterns emerge between the resonators in the system, commonly referred to as collective dynamics.

Collective dynamics in many-body systems, or networks of interconnected resonators, can give rise to many fascinating phenomena when observed over time. For example, coupled resonators with differing natural frequencies may spontaneously sync up in phase if there is a weak connection between them, through a phenomenon called synchronization[23]. While collective behavior like synchronization can be captivating to observe in nature[4], dynamics of many-body networks can have prominent effects on vital systems including health[5,6] and technology[7,8], governing the collective beating of pacemaker cells[9] and the operation of the national power grid [10,11]. To better predict network behavior, research in the field of many-body physics has become widespread.

Understanding the collective behavior of many body systems is also essential for a wide range of fields in physics, from quantum mechanics[8,12] to astronomy[13]. While modeling physical systems can give insight into the natural world, tunability of each network node and their connectivity would provide a means to experimentally realize systems that do not occur naturally. The idea of network programmability has led to the pursuit of new computing schemes, including both quantum and classical, that can be used to explore and understand problems with high dimensional parameter spaces, necessary for complex computation. Therefore, it is not only essential to develop ways to thoroughly understand how energy moves between coupled resonator networks[14], but to also develop programmable platforms to achieve new technologies that utilize the power of collective dynamics.

1.2 Coupled NEMS resonators as a model system for many-body physics

One way to enhance understanding of large coupled systems is by implementing physical nanoscale models, in which we can set the initial conditions and observe the system as it evolves. There are many options to use as the building blocks of these nanoscale models, including LCR circuits[15], Josephson junctions[7], and semiconductor lasers[16]. One method that is particularly attractive is to use micro/nanoelectromechanical systems (MEMS/NEMS) as the building blocks[17–19] because they are dimensionally small for scalability, evolve on fast time scales, couple strongly to their environment, and are low power compared to their electrical counterparts[20].

In addition to functioning as a modeling platform, NEMS networks are also attractive for technological advancements. For example, the vibrations of atoms in a diatomic crystal lattice can be modeled as a linear chain of masses and springs[21]. This model gives way to the formation of phononic bandgaps, or frequency ranges in which phonons cannot propagate through the lattice. This property extends to linear chains of coupled NEMS and can be used for applications such as signal filtering[22] and phononic shielding[23].

The scope of NEMS networks can be expanded for novel technologies by developing methods to control the mechanical parameters of the network; meaning techniques to tune the masses, intrinsic spring constants, coupling spring constants, and damping. With the ability to tune these parameters, we also move towards exploring new physics that does not occur in nature. This includes the experimental realization of dynamic phononic bandgaps[24–27], essentially transforming a vibrational insulator to a conductor. Additionally, we can create tunable defects[27] to dynamically control phonon propagation and metamaterials[28,29] to achieve counterintuitive material properties, such as thermal rectification[30] for unidirectional heat flow. With large enough networks and precise enough control, coupled NEMS resonators can even be used to achieve alternative computing schemes with mechanical logic[31] and neuromorphic computation[32,33]. Multi-level quantum systems can also be simulated with coupled NEMS resonators[34–36] and NEMS waveguides can be used as energy transducers to connect components of quantum circuits in quantum computers[37] and networks[38].

While there has been great progress in the development of tuning methods in coupled NEMS resonators, scalability of the platforms remains an outstanding challenge. A typical method of achieving strong coupling between resonators is through a shared clamping point, which has been investigated in multiple systems including GaAs pillars[19] and SiN beams[39]. However, modifying the mechanical coupling strength in these systems requires fabricating new devices to alter the clamping lengths, which limits the overall tunability. Another common method of tuning the coupling strength that can be achieved dynamically is through a parametric drive, in which the coupling strength is dependent on the amplitude of the pump modulation. This method has been demonstrated between SiN[39,40], Si[17], and GaAs beams[41]. Parametric driving, however, has limited scalability because this method requires persistent individual addressing of each resonator in the network.

Once a scalable platform of coupled resonators has been achieved, it will be essential to develop robust characterization methods to read out the current conditions of the network and to inform further programming. Typically, the mechanical parameters – masses, spring constants, damping, and driving forces – are characterized by fitting amplitude spectra using least squares fitting[19,42]. While this method is effective for determining resonance frequencies and damping, the individual values of masses and spring constants are highly dependent on user input guesses and the correlations between these parameters often leads to large associated errors[43]. Additionally, spectra analysis does not give insight into the spatial location of the characterized parameters. Spatial information is important for fully understanding the state of the network and for determining which nodes may need further tuning. Weak coupling will need to be characterized as it is an essential component in phenomena such as synchronization[5,18]. To reach the full potential of using NEMS resonators as large-scale networks, we need to develop a method of characterizing and subsequently spatially mapping each mechanical parameter.

To investigate and employ collective behavior in many-body NEMS systems, it is imperative to overcome the current challenges in scalability and characterization of coupled NEMS resonators. To build a scalable platform, we need a device design that is optimized for strong coupling, tunability, and scalability. We then need to develop a method to characterize all the mechanical parameters of the network to diagnose the initial state and determine how to tune each component the system[44].

1.3 Graphene NEMS resonators

The distinct properties of graphene make suspended graphene resonators an attractive platform for a coupled NEMS network. A suspended graphene resonator in a drumhead platform is shown in **Figure 1.1**. Graphene, a single layer of hexagonally bonded carbon atoms, is both the thinnest and strongest material known today[45,46]. The combination of low mass and high strength allows for the out of plane deflection of suspended membranes up to about 4% without rupturing[47]. Static deflection causes an increase in the membrane tension, which can tune a drumhead resonance frequency up to several hundred percent[42]. Graphene has a large in-plane elastic modulus[46,48], setting the operating frequency of suspended resonators in the MHz regime and generating strong non-linearities[49], which are essential for achieving higher order interactions[18,50,51] and quantum applications[52]. Because graphene is very low mass, it couples strongly to the surrounding environment, which has made single graphene resonators ideal for force[53], pressure[47], and mass sensors[54]. It also has broadband absorption, which has been utilized to create a graphene bolometer[55], or light sensor, with an RC time-constant that is fast enough to drive the graphene resonators in the MHz regime. The fast responsivity of graphene to these environmental couplings also offers multiple tuning options[56,57]. Because fabrication limitations make it nearly impossible to fabrication multiple NEMS resonators of the exact same resonance frequency, the tuning methods and general tunability of graphene make it an attractive option for aligning the frequencies of drumheads in large scale arrays.

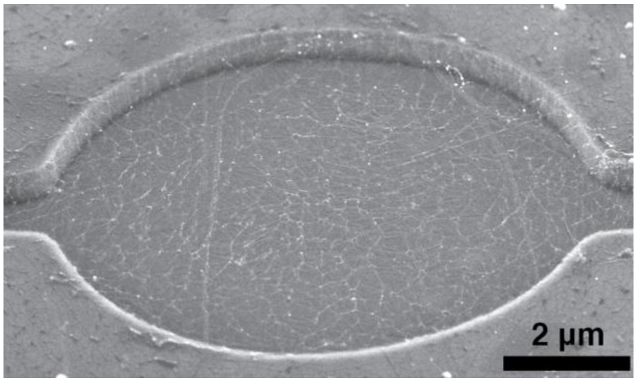

Figure 1.1 Suspended graphene drumhead resonator

Scanning electron microscope image of suspended graphene drumhead resonator. Image reproduced from co-authored manuscript in progress.

Coupled nanomechanical suspended graphene resonators have the potential to overcome the limitations in the scalability of size[58,59] and tuning. Although mechanical strain coupling has not been well studied between graphene resonators[60], multiple experiments have demonstrated strain coupling between the modes of a single resonator[50,51]. These studies indicate a high potential that graphene will support inter-resonator mechanical strain coupling as well. Graphene resonators also can be persistently tuned with the recent development of phototuning[42]; a tuning method that does not require individual back gates or continuous application of heat. Finally, these important properties of graphene exist at room temperature and many single graphene resonator experiments have been executed with no cooling[42,51,54,55,61,62]. Achieving strong coupling between graphene resonators at room temperature would be beneficial compared to materials that require cryogenic temperatures to achieved strong coupling[17,40,41,63].

1.4 Characterizing graphene NEMS resonators

To utilize suspended graphene resonators in a large-scale network, it will be critical to develop a compatible method of characterizing the mechanical parameters of each resonator node and their interactions. To enable scalability of the graphene resonator network in two dimensions, this method must provide the ability to map the spatial configuration of the current network state, including strong and weak coupling interactions, without requiring *a-priori* knowledge of the system. To spatially map the network configuration, we can use an optical scanning method to readout the amplitude and phase of each resonator node[64]. In addition to providing spatial information of the network parameters, this imaging technique would also illuminate areas of weak coupling. Additionally, we can algebraically solve for the mechanical parameters, which can be done with less data points than least squares fitting and does not require any a-priori knowledge. Combining these two aspects would provide the ability to spatially map an entire network cluster without the need for guess solutions or knowledge of the current network configuration, enabling the network to be precisely programmed.

1.5 Outline thesis chapters

As discussed, a programmable NEMS network could be used to make a significant impact on health and technology, as well as to explore new physics. As an important step towards achieving a programmable NEMS network, this dissertation addresses the two main challenges that are currently limiting progress. First, the challenge of building a scalable platform will be addressed with the demonstration of strong 2D coupling between graphene resonators. Second, a novel characterization method will be presented in which each mechanical parameter can be determined and spatially mapped to read out the current state of a network.

Chapter II will develop the model used to characterize the suspended graphene platform. We will start by discussing an infinite linear chain of masses and springs. We will then discuss subsections of this model in detail, namely the single resonator and two coupled resonators. Notable features in spectral data and important figures of merit will also be discussed for both subset cases. We will then explore how the equation of motion of a 2D membrane resonator maps onto our linear mass and spring model.

Chapter III will outline the experimental procedures in fabricating and measuring the suspended graphene resonators. This chapter includes detailed process flows that are used to fabricate the base structures and the technique used for transferring and suspending graphene over nanoscale features. This chapter then moves into a discussion of the optical and electrical methods used to measure and drive the motion of the suspended graphene resonators.

Chapter IV is based on currently unpublished work co-authored with David Miller, Uriel Hernandez, Viva Horowitz, Andrew Blaikie, and Benjamín Alemán. This chapter presents a novel platform of suspended graphene resonators that exhibit strong coupling between resonators. We discuss data that indicates strong coupling between two and three coupled resonators. Additionally, we show inter-resonator coupling of a higher order mode.

Chapter V is based on publicly posted but currently unpublished work co-authored with Viva Horowitz, Uriel Hernandez, David Miller, Andrew Blaikie, and Benjamín Alemán. This chapter will discuss an algebraic method of spatially characterizing all mechanical parameters in a network. We start by presenting the mathematical framework of this method. We then apply this method to characterize two examples of single graphene resonators and then to two examples of coupled graphene resonators.

Chapter VI will summarize the impacts of this work and the challenges in the field of programmable NEMS networks. Future directions that are now possible with this foundation will be suggested.

2 Theoretical background

This chapter introduces a linear mass and spring model that we use to capture the dynamics of 2D suspended graphene resonators. We first introduce the infinite model and then look closer at the model subsets of one resonator and two coupled resonators. We then explain how the equations of motion of a 2D resonator map to a linear mass and spring. This model is essential for both detecting strong coupling in our suspended graphene platform, as well as determining the mechanical parameters of each resonator and their connectivity in our characterization method.

2.1 Infinite chain of masses and springs

We model our graphene NEMS network as a finite chain of masses on springs. To develop a universal model that can be truncated to represent finite chains of various lengths, or clusters, we start with an infinite model of masses and springs, **Figure 2.1**. There are two types of linear springs in the model, the intrinsic springs, shown in pink and labeled as k_n in **Figure 2.1**, and the coupling springs, shown in green and labeled as c_n in **Figure 2.1**. The intrinsic springs dictate the resonance frequency of each individual mass, while the coupling springs control the energy flow between masses. The model also includes linear damping, b_n, resonator masses, m_n, and driving forces, F_n.

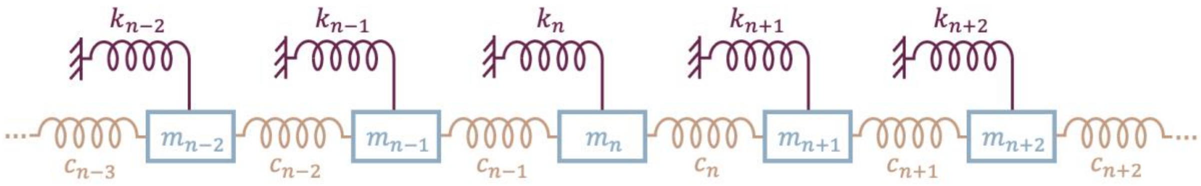

Figure 2.1 Linear mass and spring infinite chain model

Infinite chain of masses and springs. Dark maroon springs, labeled as k_n, represent intrinsic springs that dictate the individual resonance frequency of each mass, blue boxes labeled as m_n. Light tan springs, labeled as c_n, represent coupling springs that connect nearest neighbor masses.

Based on this model, we define the equations of motion for each resonator, which are shown below for three masses m_n, m_{n+1}, and m_{n-1}:

$$\vdots$$

$$m_{n-1}\ddot{x}_{n-1} + b_{n-1}\dot{x}_{n-1} + k_{n-1}x_{n-1} + c_{n-1}(x_{n-1} - x_n) + c_{n-2}(x_{n-1} - x_{n-2}) = F_{n-1}$$

$$m_n\ddot{x}_n + b_n\dot{x}_n + k_nx_n + c_{n-1}(x_n - x_{n-1}) + c_n(x_n - x_{n+1}) = F_n$$

$$m_{n+1}\ddot{x}_{n+1} + b_{n+1}\dot{x}_{n+1} + k_{n+1}x_{n+1} + c_n(x_{n+1} - x_n) + c_{n+1}(x_{n+1} - x_{n+2}) = F_{n+1}$$

$$\vdots$$

This system of equations can be organized into the matrix form:

$$\boldsymbol{M}\ddot{\vec{x}} + \boldsymbol{B}\dot{\vec{x}} + \boldsymbol{K}\vec{x} = \vec{F} \tag{2.1}$$

where the three matrices are

$$\boldsymbol{M} = \begin{pmatrix} \ddots & 0 & 0 & 0 & \cdots \\ 0 & m_{i-1} & 0 & 0 & 0 \\ 0 & 0 & m_i & 0 & 0 \\ 0 & 0 & 0 & m_{i+1} & 0 \\ \vdots & 0 & 0 & 0 & \ddots \end{pmatrix}, \quad \mathbf{B} = \begin{pmatrix} \ddots & 0 & 0 & 0 & \cdots \\ 0 & b_{i-1} & 0 & 0 & 0 \\ 0 & 0 & b_i & 0 & 0 \\ 0 & 0 & 0 & b_{i+1} & 0 \\ \vdots & 0 & 0 & 0 & \ddots \end{pmatrix},$$

$$\mathbf{K} = \begin{pmatrix} \ddots & -c_{i-2} & 0 & 0 & \cdots \\ -c_{i-2} & k_{i-1} + c_{i-2} + c_{i-1} & -c_{i-1} & 0 & 0 \\ 0 & -c_{i-1} & k_i + c_{i-1} + c_i & -c_i & 0 \\ 0 & 0 & -c_i & k_{i+1} + c_i + c_{i+1} & -c_{i+1} \\ \vdots & 0 & 0 & -c_{i+1} & \ddots \end{pmatrix}$$

2.2 Single resonator

We can reduce this system of equations to represent smaller clusters of coupled resonators. The equation of motion for the simplest cluster – a single uncoupled resonator – can be obtained by setting each neighboring coupling spring to zero. This reduction is highlighted in **Figure 2.2**, with the pink intrinsic spring and blue mass isolated from the rest of the gray components with $c_0 = c_1 = 0$ N/m. With this coupling spring condition, we are left with an independent equation of motion that represents a single driven damped harmonic oscillator.

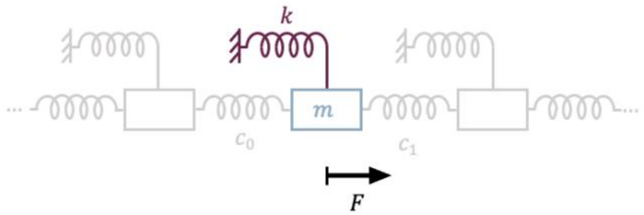

Figure 2.2: Single resonator cluster

Model of single uncoupled resonator. Highlighted maroon spring, labeled as k, and blue mass, labeled as m, are the two mechanical parameters considered in the single uncoupled resonator model. Black arrow, labeled as F, represents a driving force applied to mass m. Gray coupling springs labeled as c_0 and c_1 are both equal to zero to isolate the driven resonator from neighboring masses.

$$m\ddot{x} + b\dot{x} + kx = F \tag{2.2}$$

To solve Eq (2.2), we use a steady-state trial solution of $x(t) = Z(\omega)e^{i\omega t}$, in which $Z(\omega) = A(\omega)e^{i\delta(\omega)}$ is the complex amplitude of the driven resonator. The phase $\delta(\omega)$ corresponds to the purely mechanical phase difference between the driving force and the response $A(\omega)$. If we consider the applied driving force to be periodic, $F = F_0 e^{i\omega t}$, we can apply the steady state trial solution to simplify the differential equation of Eq (2.2) as

$$-\omega^2 mZ + i\omega bZ + kZ = F_0 \tag{2.3}$$

By re-writing $Z(\omega) = A(\omega)e^{i\delta(\omega)} = A(\omega)(\cos(\delta(\omega)) + i\sin(\delta(\omega)))$, we can split Eq.(2.3) into the real and imaginary components. By squaring each component and adding the results, we can solve for the amplitude $A(\omega)$ as

$$A(\omega) = \frac{F_o/m}{((\omega_0^2 - \omega^2)^2 + \omega^2 b^2)^{\frac{1}{2}}} \tag{2.4}$$

By dividing the imaginary component by the real component, we can solve the phase $\delta(\omega)$ as

$$\delta(\omega) = \tan^{-1}\left(\frac{2\omega b}{\omega_0^2 - \omega^2}\right) \tag{2.5}$$

The amplitude and phase as a function of drive frequency ω are shown in **Figure 2.3a**. The maximum amplitude, or resonance, occurs at a drive frequency of $\omega_r = \omega_0\sqrt{1 - \frac{1}{2}\left(\frac{b}{2\omega_0}\right)^2}$. For the limit of light damping, or very small b, we can approximate the resonance frequency as $\omega_r \approx \omega_0$. When the resonator is driven near resonance at ω_0, we can observe the characteristic $\pi/2$ phase lag between the driving force and the amplitude response, with $\delta(\omega_0) \approx \pi/2$ indicated by the black dashed line in **Figure 2.3a.**

A common figure of merit used to quantify the damping of a driven resonator, is the quality factor Q. The quality factor is the ratio between the energy stored W to the energy lost ΔW in one oscillation cycle[65].

$$Q = 2\pi\frac{W}{\Delta W} \tag{2.6}$$

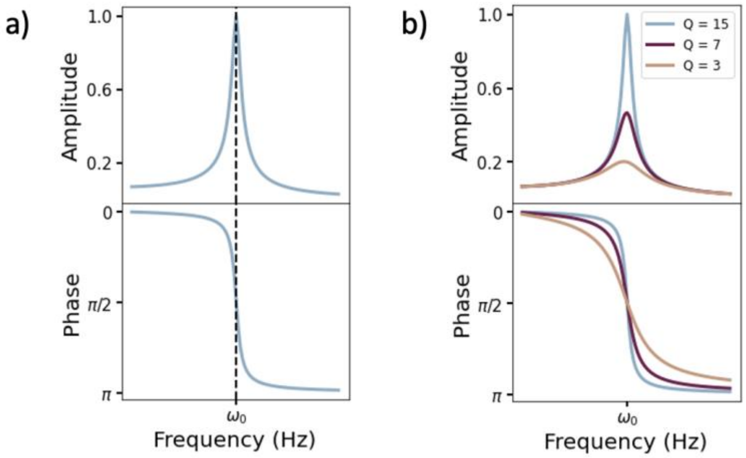

Figure 2.3: Simulated amplitude and phase of single drive damped resonator

a) Amplitude (upper) and phase (lower) spectrum of driven damped resonator with dashed vertical line marking drive frequency of $\omega_0 = \sqrt{k/m}$. Simulation for $k = 50$ N/m, $m = 1$ kg, $F = 100$ N, and $b = (\omega_0/15)$ kg/s. **b)** Amplitude (upper) and phase (lower) spectra of resonators with varying amounts of damping, with quality factors as $Q = 15$ ($b = \omega_0/15$) in for blue, $Q = 7$ ($b = \omega_0/7$) for orange, and $Q = 3$ ($b = \omega_0/3$) for green.

The total energy in the system is defined as $W = \frac{1}{2}m\dot{x}^2$. For the case of a damped resonator driven at resonance, we can calculate the maximum velocity from the steady-state solution, $\dot{x}(\omega_r) = Z(\omega_r)(i\omega_r)e^{i\omega_r t}$. If we assume light damping in the system, the maximum energy can be written as $W = \frac{1}{2}m(A\omega_0)^2$. The energy lost over one oscillation cycle can be calculated by considering the dissipative component of the net force, $F_{diss} = -b\dot{x}$. We can calculate the instantaneous energy loss, or the work done by the dissipative force, as $\Delta W = F_{diss}\dot{x}dt$. The total energy lost in one oscillation cycle can be calculated by integrating over the time it takes for the system to complete a single period[65].

$$\Delta W = -\int_0^{2\pi/w_0} F_{diss}\dot{x}dt = \pi b A^2 \omega_0 \tag{2.7}$$

This solution yields the quality factor of a driven damped resonator to be

$$\mathrm{Q} = \frac{\omega_0}{(b/m)}. \tag{2.8}$$

Figure 2.3b shows how the amount of damping in the system will affect the sharpness of the resonance amplitude. As damping increases, the quality factor will decrease, and the amplitude curve will become wider and shorter. In the case of light damping, the quality factor can be approximated by the ratio of resonance frequency to the full width half maximum of an experimentally measured amplitude peak.

2.3 Two coupled resonators

We can reduce Eq (2.1) to represent the next smallest cluster size – two coupled resonators – by again setting the outer most coupling springs equal to zero. This reduction is highlighted in **Figure 2.4**, with the two pink intrinsic springs and two blue masses connected by the green coupling spring. This highlighted section of the model is isolated from the rest of the gray components with $c_0 = c_2 = 0$ N/m. To group the active components, we will consider the parameters $\{k_1, m_1\}$ to be one resonator and $\{k_2, m_2\}$ to be a second resonator, labeled as R1 and R2 respectively in **Figure 2.4**.

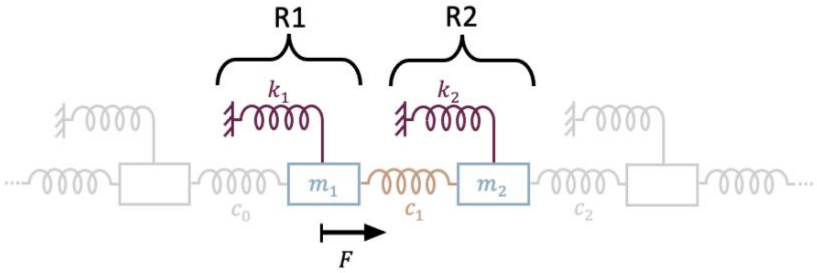

Figure 2.4: Two coupled resonator model

Model of two coupled resonators. Highlighted dark maroon intrinsic springs, labeled as k_1 and k_2, and blue masses, labeled as m_1 and m_2, and light tan coupling spring, labeled as c_1, are the mechanical parameters considered in the coupled resonator model. Upper black bracket labeled as R1 represents the grouping of k_1 and m_1 to be one resonator and upper black bracket labeled as R2 represents k_2 and m_2 grouped as a second resonator. Black arrow, labeled as F, represents a driving force applied to R1. Gray coupling springs labeled as c_0 and c_2 are both equal to zero to isolate the driven resonator from neighboring masses.

With this configuration, we are left with two coupled equations of motion. Considering Eq (2.1), the three matrices $\boldsymbol{M}$, $\boldsymbol{B}$, and $\boldsymbol{K}$ can be simplified as

$$\boldsymbol{M} = \begin{pmatrix} m_1 & 0 \\ 0 & m_2 \end{pmatrix}, \qquad \mathbf{B} = \begin{pmatrix} b_1 & 0 \\ 0 & b_2 \end{pmatrix}, \qquad \mathbf{K} = \begin{pmatrix} k_1 & -c_1 \\ -c_1 & k_1 \end{pmatrix}$$

Again, we can apply a steady-state trial solution of $x_n(t) = Z_n(\omega)e^{i\omega t}$, in which x_n represents the position of the n^{th} resonator and $Z_n(\omega) = A_n(\omega)e^{i\delta_n(\omega)}$. If we consider a periodic driving force applied only to R1, we can simplify the coupled differential equations and combine $\boldsymbol{M}$, $\boldsymbol{B}$, and $\boldsymbol{K}$ to write the system of equations as

$$\begin{pmatrix} -\omega^2 m_1 + i\omega b_1 + k_1 + c_1 & -c_1 \\ -c_1 & -\omega^2 m_2 + i\omega b_2 + k_2 + c_1 \end{pmatrix} \begin{pmatrix} Z_1 \\ Z_2 \end{pmatrix} = \begin{pmatrix} F_0 \\ 0 \end{pmatrix} \tag{2.9}$$

We can solve for the complex amplitudes each resonator, Z_1 and Z_2, by using Cramer's rule, in which each amplitude is equal to the ratio of the determinants of the coefficient matrix with one row replaced by the right-side force vector and the original coefficient matrix. We can then use $Z_n(\omega) = A_n(\omega)e^{i\delta_n(\omega)}$ to solve for the amplitude $A_n(\omega)$ and phase $\delta_n(\omega)$ of each resonator.

There are several key properties revealed by the amplitude and phase behavior of each of the two resonators, with the amplitude and phase spectra shown in **Figure 2.5a** for R1 and **Figure 2.5b** for R2. In each amplitude spectra, **Figure 2.5a,b** (upper), there are two distinct peaks, as opposed to the single amplitude peak observed for the uncoupled resonator, **Figure 2.3a.** The emergence of two peaks is called normal mode splitting and is due to the hybridization the individual resonances of R1 and R2. If we consider the system to have no driving or damping, the hybridized mode frequencies can be derived from Eq(2.9) as,

$$\omega_{\pm}^2 = \left(\frac{1}{2}\right)\left(\omega_1^2 + \omega_2^2 \pm \sqrt{(\omega_1^2 - \omega_2^2)^2 + 4\Gamma^2\omega_1\omega_2}\right) \tag{2.10}$$

in which, $\omega_{1,2} = \sqrt{\frac{k_{1,2}+c}{m_{1,2}}}$ and $\Gamma = \sqrt{\frac{(c/m_1)(c/m_2)}{\omega_1\omega_2}}$. These two modes are highlighted with gray dashed lines in the amplitude and phase spectra of **Figure 2.5a,b.**

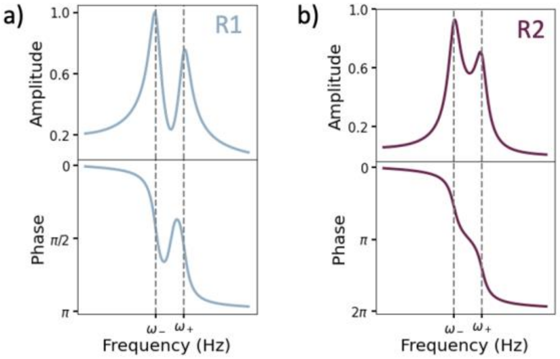

Figure 2.5: Simulation of amplitude and phase curves of two coupled resonators

Simulated model of $k_1 = k_2 = 50$ N/m, $m_1 = m_2 = 1$ kg, $b_1 = b_2 = 1$ kg/s, $F = 10$ N, and $c = 20$ N/m. **a)** Amplitude (upper) and phase (lower) spectra of driven resonator R1. **b)** Amplitude (upper) and phase (lower) spectra of neighboring coupled resonator R2. In both plots, vertical gray dashed lines are set at frequency values of ω_- and ω_+.

The phase behavior of the two resonators is important for distinguishing the two modes when only observing the resonator motion. The phase spectra, **Figure 2.5a,b** (lower), shows that at the lower frequency mode, ω_-, each resonator will oscillate with a phase lag of $\delta \approx \pi/2$, meaning they will oscillate about in phase with each other. For the higher frequency mode, ω_+, R1 will again oscillate with a phase lag of $\delta \approx \pi/2$, however, R2 will oscillate with a phase lag of $\delta \approx 3\pi/2$, meaning that in the higher frequency mode, the two resonators will typically oscillate $\sim\pi$ out of phase with each other.

A common figure of merit used to quantify the coupling between two resonators is the coupling strength, which is equal to Γ. For the case of symmetric resonators, with identical masses and spring constants, the coupling strength can be simplified to $\Gamma = \omega_+ - \omega_- = \Delta\omega$, resulting in $\Delta\omega \propto c$. This means that the distance between the normal mode peaks will increase as the coupling spring constant increases. To quantify the coupling strength as “strong coupling”, the distance between the normal mode peaks must be resolvable considering the linewidths of each mode, or $\Gamma > \frac{b_1}{m_1} + \frac{b_2}{m_2}$. **Figure 2.6** shows amplitude spectra of R1 in the coupled resonator pair for a range of coupling strengths. We see that the normal mode peaks are not resolvable for the case of weak coupling **Figure 2.6a**, but can be distinguished when the coupling strength crosses into the strong coupling regime, **Figure 2.6b,c**.

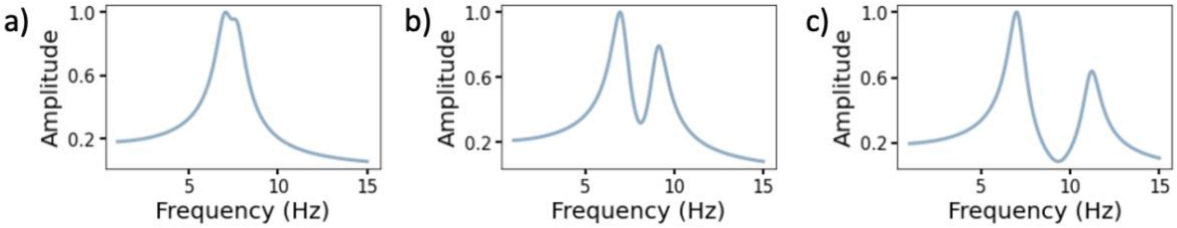

Figure 2.6: Simulated amplitude spectra for range of coupling strengths

Simulated amplitude and phase spectra of driven resonator R1 for the same masses, intrinsic spring constants, damping, and force as in Figure 2.5. Plotted for the case of **a)** weak coupling in which $\Gamma/\left(\frac{b_1}{m_1} + \frac{b_2}{m_2}\right) = 0.3$ for $c \approx 4$ N/m, **b)** exactly at the threshold of strong coupling, in which $\Gamma/\left(\frac{b_1}{m_1} + \frac{b_2}{m_2}\right) = 1$ for $c \approx 16$ N/m, and finally **c)** for coupling well within the strong coupling regime, in which $\Gamma\left(\frac{b_1}{m_1} + \frac{b_2}{m_2}\right) = 2$ for $c \approx 37$ N/m

Because $\Gamma = \Delta\omega$ only when the two resonators are symmetric, it is typical that the coupling strength is experimentally determined by sweeping the spring constant of one of the resonators and finding the minimum peak separation, which will occur when $\omega_1 \approx \omega_2$. **Figure 2.7a,b** shows how each mode frequency is tuned when sweeping the individual spring constant of the driven resonator, k_1. This curve shape is commonly referred to as an avoided crossing, as the modes will get close to each other, such as at the point labelled as Γ in **Figure 2.7a**, but will not cross.

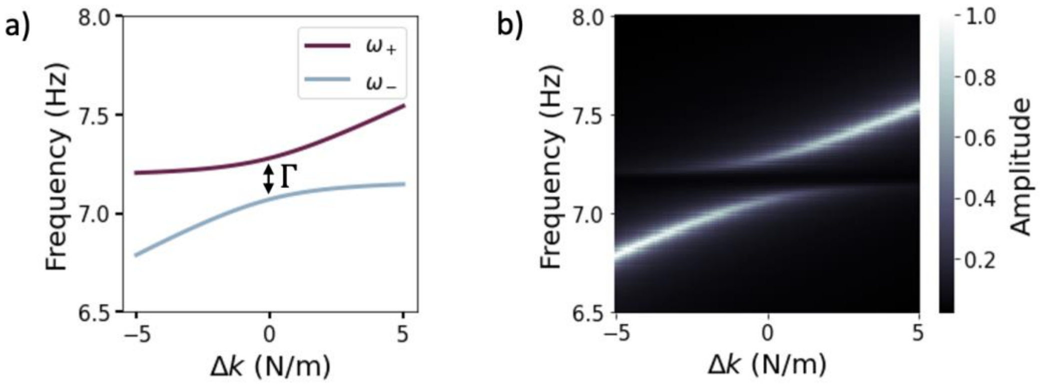

Figure 2.7: Simulated avoided crossing spectrographs

Simulated for coupled resonators with $k_2 = 50$ N/m, $m_1 = m_2 = 1$ kg, $F = 10$ N, $b_1 = b_2 = 0.05$ kg/s, and $c = 1.5$ N/m. **a)** Normal modes plotted as a function of $\Delta k = k_1 - k_2$, calculated by sweeping the spring constant k_1 of the driven resonator R1. Lower frequency mode ω_- is plotted in blue and higher frequency mode ω_+ is plotted in orange. Approximate minimum value of mode separation $\Delta\omega$ is denoted by doubled-sided arrow, labeled as Γ. **b)** Avoided crossing spectra plotted with corresponding mode amplitudes for strongly coupled resonators.

2.4 Single graphene resonators modeled as mass and springs

In this work, we utilize this linear mass and spring chain, **Figure 2.1**, as an effective lumped-element model to capture the dynamics of 2D graphene drumhead resonators. To outline how each effective parameter of the continuum mechanical 2D resonator maps to a physical parameter in the lumped-element model, we will compare the continuum mechanics model of a single drumhead resonator to a damped driven mass on a spring. We will start by considering the equation of motion for a vibrating plate[66] with a mode shape defined as $u(r, \theta, t)$.

$$\rho\left(\frac{\partial^2 u(r,\theta,t)}{\partial t^2}\right) - \Gamma\left(\frac{\partial u(r,\theta,t)}{\partial t}\right) + D\nabla^4 u(r,\theta,t) - T\nabla^2 u(r,\theta,t) = F(r,\theta,t) \tag{2.11}$$

In this equation ρ is the material density, Γ is the damping, T is the tension, and D is the bending stiffness. We can separate the mode shape function into its spatial and temporal components as $u(r,\theta,t) = \sum_{n=1}^{\infty}\sum_{m=1}^{\infty}\phi_{nm}(r,\theta)u_{nm}(t)$. If we assume that all vibrations in the plate are due to a single vibrational mode, we can focus on a single term of the sum as $u(r,\theta,t) \rightarrow \phi_{nm}(r,\theta)u_{nm}(t)$. From here, we can recover the equation of motion for a driven damped resonator, as in Eq(2.2), by multiplying Eq(2.11) by the mode shape, $\phi_{nm}(r,\theta)$ and integrating over the area of the circular drumhead[65].

$$m_{eff}\ddot{u}_{nm}(t) - \gamma_{eff}\dot{u}_{nm}(t) + k_{eff}u_{nm}(t) = F_{eff}\cos(\omega t) \tag{2.12}$$

$$m_{eff} = \rho\int_0^{2\pi}\int_0^R \phi_{nm}^2(r,\theta)rdrd\theta$$

$$k_{eff} = D\int_0^{2\pi}\int_0^R \phi_{nm}\nabla^4\phi_{nm}(r,\theta)rdrd\theta - T\int_0^{2\pi}\int_0^R \phi_{nm}\nabla^2\phi_{nm}(r,\theta)rdrd\theta$$

$$\gamma_{eff} = \Gamma\int_0^{2\pi}\int_0^R \phi_{nm}^2(r,\theta)rdrd\theta$$

$$F_{eff} = \int_0^{2\pi}\int_0^R f(r,\theta)\phi_{nm}rdrd\theta$$

The 2D nature of the drumhead resonators in this work enables complex dynamics, including the existence of higher order modes, in which the membrane can experience multiple resonances, each with a specific vibrational pattern of amplitude and phase within a single resonator. We can calculate these mode shapes by solving the partial differential equation in Eq(2.11) for the case of zero damping and no driving force. The resulting mode shape $u(r,\theta,t)$ can be written in the spatial and temporal components as [66]

$$\phi_n(r,\theta)\sin(\omega_0 t) = \left(A_nJ_n\left(\frac{\alpha r}{R}\right) + B_nI_n\left(\frac{\beta r}{R}\right)\right)(\cos(n\theta) + \lambda_n\sin(n\theta))\sin(\omega_0 t) \tag{2.13}$$

$$\alpha^2 = \frac{TR^2}{2D}\left(\left(1 + \frac{4\omega_0\rho D}{T^2}\right)^{1/2} - 1\right)$$

$$\beta^2 = \frac{TR^2}{2D}\left(\left(1 + \frac{4\omega_0\rho D}{T^2}\right)^{1/2} + 1\right)$$

in which $J_n(x)$ and $I_n(x)$ are the Bessel functions of the first kind and the modified Bessel function respectively, R is the radius of the plate, and A_n, B_n, λ_n are arbitrary constants. We can simplify this equation further by approximating the vibrating plate as a membrane, in which the tension is much larger than the bending stiffness, $R^2T \gg D$, to write our spatial mode shape term as

$$\phi_n(r,\theta) \approx AJ_n\left(\frac{\alpha_{nm}r}{R}\right)\cos(n\theta) \tag{2.14}$$

We can use the approximation in Eq(2.14) to plot the spatial mode shapes of a circular membrane. The first four lowest energy modes plotted in **Figure 2.8**. We can see in **Figure 2.8a,d,** that some modes are radially symmetric in amplitude and phase, while others, such as **Figure 2.8.b,c,** are not. The modes that are not radially symmetric are degenerate due to the additional solution set of $\phi_n(r,\theta) \sim \sin(n\theta)$ supplementing the solution set in Eq(2.14).

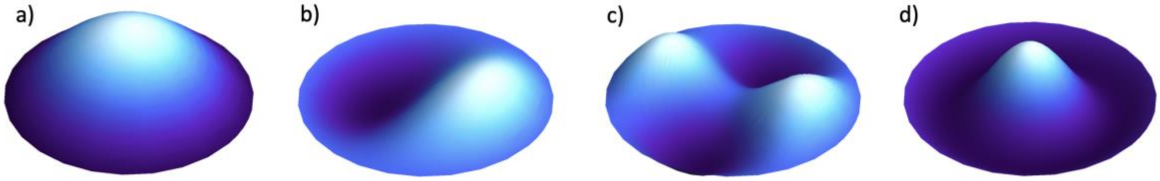

Figure 2.8: Mode shapes of vibrating circular plate

First four mode shapes of vibrating circular plate for **a)** fundamental (1,0) mode for $\alpha_{1,0} = 2.404$, **b)** (1,1) mode for $\alpha_{1,1} = 3.832$, **c)** (1,2) mode for $\alpha_{1,2} = 5.135$, and **d)** (2,0) mode for $\alpha_{2,0} = 5.520$.

We can model these higher order modes with a lumped-element discrete mass and spring model by introducing additional degrees of freedom. For example, the first and second order modes of a 2D drumhead can be modeled as two coupled masses on springs, in which the symmetric mode would correspond to the lower frequency fundamental drumhead vibration and the antisymmetric mode would correspond to the higher frequency out of phase drumhead vibration.

3 Experimental methods

In this chapter, we review the experimental methods used in this work. We explain in detail the procedure used to fabricate the base structure of our devices and our technique for graphene suspension, which together results in a new platform to host strong coupling between resonators. We then explain our measurement technique that is used to drive and measure the motion of the resonators, which is essential for detecting coupling and for spatially characterizing the mechanical parameters of the network.

3.1 Fabrication of device platforms

We fabricated the suspended graphene resonator devices using standard nanofabrication processes to pattern the base substrate, followed by a wet transfer method of the graphene. We began our process with degeneratively doped conductive silicon (Si) wafers with 1-2 μm of commercially grown wet silicon oxide (SiO_2), shown in the first block diagram of **Figure 3.1a**.

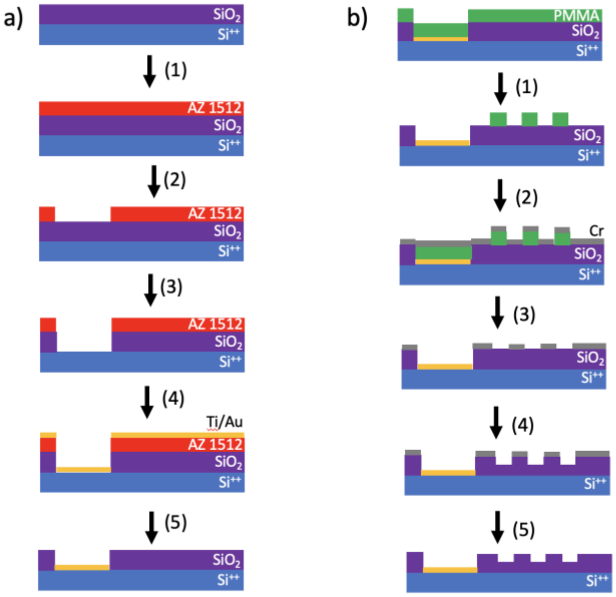

Figure 3.1: Substrate fabrication process flows

a) Process flow for photolithography, specifically for fabricating vias. Start with SiO_2 on Si and (1) spin on AZ1512 photoresist. (2) Expose the resist with a laser to pattern and develop to remove exposed regions of resist. (3) REI to etch exposed SiO2. (4) Deposit Ti/Pt or Ti/Au electrode and finally (5) lift off remaining AZ1512 resist. **b)** Process flow for masked electron beam lithography. Start with sample that has vias and spin on PMMA resist. (1) Expose the resist with electron beam and develop to remove exposed regions of resist. (2) Deposit Cr layer and (3) liftoff PMMA such that only the Cr mask remains on the sample. (4) REI to etch exposed regions of SiO2. (5) Etch Cr layer.

The first step in our process was to make a via on the sample, or a small hole through the SiO_2 that allows for an electrical connection to the doped silicon wafer, **Figure 3.1a**. We began this process by cleaning the Si/SiO_2 substrates with acetone sonication, followed by isopropyl alcohol, and finally rinsing with deionized water. To prepare the surface of the substrate to be hydrophobic for better photoresist adhesion, the samples were dehydrated on a hotplate at 400°C for 30 minutes and afterwards exposed to hexamethyldisilazane (HMDS) for 20 minutes. We used a spin coater to disperse an even layer of photoresist (MicroChem AZ1512) on the substrate, with a spin speed of 4000 rpm for a resulting photoresist thickness of ∼1.2 μm, step (1) in **Figure 3.1a**. Any remaining solvent was evaporated from the photoresist with a soft bake on a hot plate for two minutes at 105°C. We then applied a second layer of photoresist and repeated the soft bake. This extra thick layer of photoresist would reduce the likelihood of etching pin holes through the SiO_2, which could later lead to electrical shorting of the sample. Although we typically avoid thick layers of resist for lithography, as it will limit the pattern resolution, because the vias were millimeters in size, resolution was not a limiting factor in this process flow. We patterned the photoresist with a 405 nm laser in a Microtech direct write laser lithography system. The pattern was developed (MicroChem AZ300 developer) for one minute and the photoresist was further solidified with a hard bake at 100°C for one minute, step (2) in **Figure 3.1a**. We etched the exposed SiO_2 in a 5:1 hydrofluoric acid (49% concentration in water) buffered with ammonium fluoride, at an etch rate of about 100 nm/min[67], to open a via to the bare silicon, step (3) in **Figure 3.1a**. We then deposited an electrode of 10 nm of titanium and 40 nm of platinum that directly contacted the silicon substrate with a physical vapor deposition system (Angstrom Instruments E-Beam/Thermal Deposition), step (4) in **Figure 3.1a**. Finally, we soaked the sample in acetone for 10 minutes to liftoff the remaining photoresist, resulting in a metal electrode that directly contacted the silicon substrate from the top of the sample, step (5) **Figure 3.1a**.

After fabricating the via contact, we conducted a second lithography process to pattern and etch the SiO_2 with the desired resonator geometries. If these geometries had feature sizes all larger than 1 μm, we would repeat the photolithography procedure outlined above to pattern the substrate, this time using a single layer of photoresist, as opposed to the two layers used for the vias. However, for feature sizes smaller than 1 μm, we typically used electron beam lithography to increase the pattern resolution to sub-optical wavelengths. For electron beam lithography, we followed the cleaning and dehydrating procedure as outline above and then applied PMMA A4 resist (MicroChem) with a film thickness of ∼200 nm, shown in the first block diagram in **Figure 3.1b**. The samples were then placed on a hotplate for a soft bake at 180°C to evaporate any remaining solvent from the resist. We patterned the resist using a Zeiss scanning electron microscope (SEM), adapted for direct write electron beam lithography. The pattern was developed in a 1: 3 solution of methyl isobutyl ketone (MIBK) and IPA for 60 seconds, step (1) in **Figure 3.1b**. The sample was then placed on a hotplate at 100°C for one minute to harden and ensure good adhesion of the remaining resist. From here, we either used the resist as a mask and skipped straight to etch the etch step, or we deposited chromium (Cr) to form a negative mask to etch the regions that were not exposed during lithography, with the Cr mask procedure outlined in **Figure 3.1b**. For the Cr mask, we deposited a thin layer (~ 20 nm) using thermal physical vapor deposition, step (2) in **Figure 3.1b**. We then soaked the sample in Remover PG (MicroChem) on a hotplate at $50°C$ for one hour to gently liftoff the resist, step (3) in **Figure 3.1b**. Before removing the sample from the Remover PG, we sonicated the solution to ensure complete resist removal, resulting in a negative Cr mask. To etch the smaller pattern features, we used a dry reactive ion etch (RIE), rather than an isotropic wet etch. We would typically etch $500 - 1000$ nm of the SiO_2 using CHF_3 and Ar in an inductively coupled plasma instrument (Oxford Instruments PlasmaPro 80 ICP RIE) at a rate of ~ 50 nm/min, step (4) in **Figure 3.1b**. During this step, it was important not to etch all the way through the SiO_2 to avoid electrically shorting the sample in the event of collapsed graphene. Finally, we removed the Cr mask with a wet etch, resulting in a sample with both a via and SiO_2 structures for suspending graphene, step (5) in **Figure 3.1b**.

Finally, we patterned electrodes on top of the SiO_2 that would electrically contact the graphene. To pattern the top electrodes, we repeated the photolithography process outlined above with a single layer of photoresist. After developing the pattern, we deposited 10 nm of Ti followed by a 40 nm of Pt. Finally, we removed the remaining photoresist by soaking the samples in acetone for $1 - 3$ hours. An image of a final device is shown in **Figure 3.2a**.

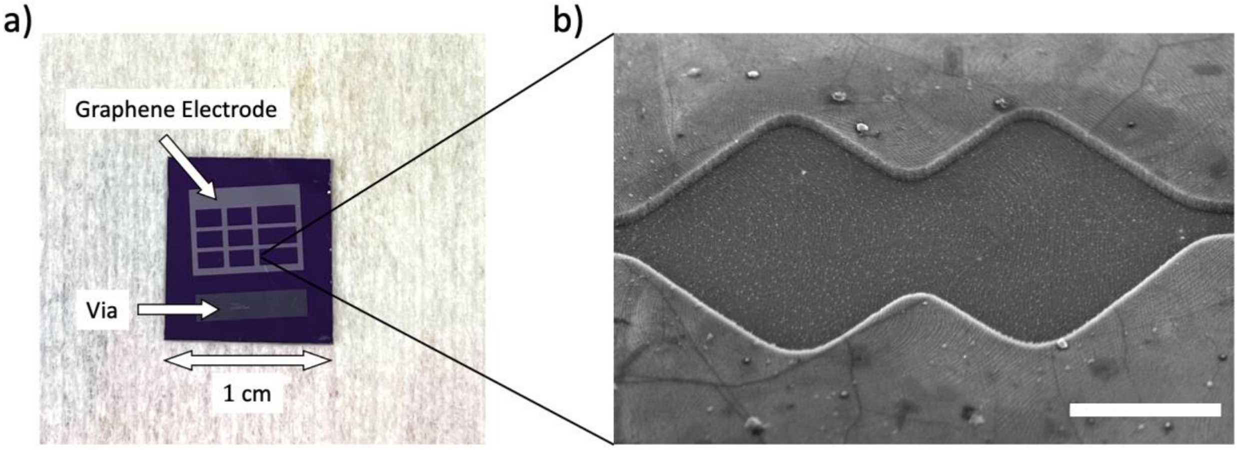

Figure 3.2: Images of completed fabricated sample

a) Camera photograph of sample showing the platinum Graphene Electrode deposited on SiO_2. The etched Via deposited onto the Si substrate. **b)** SEM image of suspended graphene device that would be within the Graphene Electrode grid. Overlapping square outline is etched SiO_2 and graphene is suspended over the trench, which can be seen in the fine continuous grain lines over the area. Graphene extends to sit directly on the non-etched SiO_2 outside of the overlapping square region. Scale bar is 5 µm.

3.2 Wet transfer method of graphene

We used a wet transfer method to suspended graphene over the etched SiO_2 features. We started our transfer with commercially grown graphene on copper foil (ACS Material), shown as the first block diagram in **Figure 3.3**. To begin the process, we applied a layer of PMMA A11 resist (~800 nm) onto one side of the graphene/copper sheet to support to the graphene layer during the transfer, step (1) in **Figure 3.3**. After applying the resist, we dried the sheets in air for $10 - 15$ min before carefully floating the PMMA/graphene/copper sheet copper side down in a solution of 40 mg/mL ammonium persulfate to etch the copper, step (2) in **Figure 3.3**. Once the copper foil was completely etched, usually after $1 - 2$ hours, we transferred the PMMA/graphene sheet to float in three successive water baths to dilute any remaining ammonium persulfate. While the PMMA/graphene sheet was in the final water bath, we prepared the Si/SiO_2 substrate for the transfer. We soaked the substrate in a of $3:1$ Pirahna solution of sulfuric acid and hydrogen peroxide for $4 - 5$ minutes to clean the surface and make it hydrophilic for better adhesion. We then used the substrate to scoop the PMMA/graphene sheet directly from the surface of the final water bath, step (3) in **Figure 3.3**, and dried it overnight in air to minimize any liquid trapped between the graphene and SiO_2. The sample was then baked for 5 minutes at 105°C to soften the PMMA and allow the graphene to adhere better to the surface of the sample. We removed the PMMA layer by soaking the sample in Remover PG for $5 - 6$ hours, step (4) in **Figure 3.3**. To minimize tensions in the graphene that occur when drying, we used a critical point dryer (Tousimis Autosamdri) to transfer the sample from solution into air. The final sample consisted of graphene adhered to the SiO_2 substrate, suspended over the lithography defined and etched geometries, shown in **Figure 3.2b**.

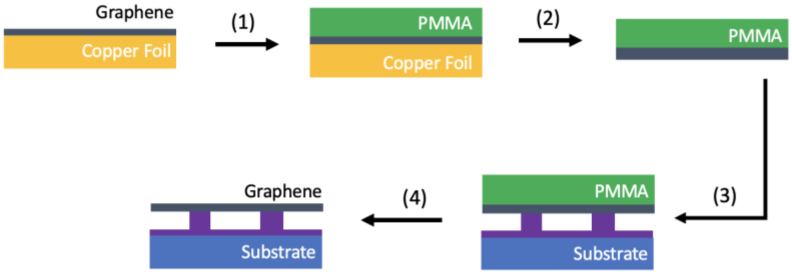

Figure 3.3: Graphene transfer process flow

Starting with graphene on copper foil, (1) spin PMMA resist over the graphene. (2) Etch the copper foil such that only the PMMA/graphene layer remains and then float in water bath. (3) Scope the PMMA/graphene layer from water bath with substrate and allow to dry. (4) Etch PMMA with PG remover and critical point dry to leave only graphene suspended across the substrate.

3.3 Actuation and tuning of graphene resonators

We utilize two methods of actuating the out of plane motion of the suspended graphene resonators, both of which can also be used to tune the tension of the graphene, thereby tuning the resonance frequency of the suspended resonator. The first method shown in **Figure 3.4,** is to electrically drive and tune the resonator and the second is to thermally drive and tune the resonator. In this work, we use a combination of both methods.

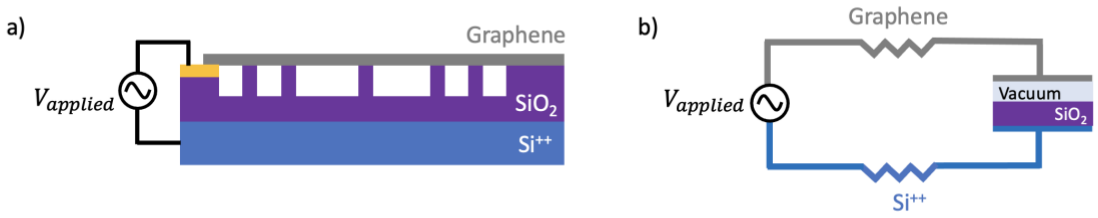

Figure 3.4: Electrical actuating of suspended graphene and equivalent circuit

a) Block diagram showing applied alternating bias to gold electrode contacting the graphene and to the doped silicon. **b)** Equivalent circuit diagram showing applied bias with resistive graphene and silicon wires leading to parallel plate capacitor with a two layered dielectric.

We can electrically tune and drive the out of plane motion of the resonators by applying a DC offset with an alternating bias across the silicon substrate and the suspended graphene, shown in **Figure 3.4a**. The amplitude and frequency of the alternating bias will control the drive of the resonator and the DC offset will govern the tension or tuning of the resonator. The equivalent circuit diagram of this set-up is shown in **Figure 3.4b**. The graphene and the substrate form a parallel plate capacitor with a vacuum and SiO_2 layer as dielectrics stacked in series, for which we can write the capacitance as,

$$C = \left(\frac{1}{C_{vac}} + \frac{1}{C_{SiO_2}}\right)^{-1} = A\epsilon_0 \left(d_{vac} + \frac{d_{SiO_2}}{\kappa_{SiO_2}}\right)^{-1} \quad (3.1)$$

In which A is the area of the parallel plates, ϵ_0 is the permittivity of free space, κ_{SiO_2} is the dielectric constant of SiO_2, and d_{vac} and d_{SiO_2} are the thicknesses of each dielectric layer. When the capacitor is charged, there will be a force between the plates described by

$$F_C = -\frac{\partial U}{\partial x} = -\frac{1}{2}\frac{\partial}{\partial x}(CV^2) \quad (3.2)$$

If we consider an alternating voltage source with a DC offset, $V = V_{DC} + V_{AC}e^{i\omega t}$, the capacitive force can be written as

$$F_c = -\frac{1}{2}\left(V_{DC}^2 + 2V_{DC}V_{AC}e^{i\omega t} + V_{AC}^2 e^{2i\omega t}\right)\left(\frac{\partial C}{\partial x}\right) \tag{3.3}$$

In Eq(3.3), there are three terms that contribute to the capacitive force. The first term, $-\frac{1}{2}V_{DC}^2\left(\frac{\partial C}{\partial x}\right)$, applies a constant force to the graphene. The second term, $-V_{DC}V_{AC}e^{i\omega t}\left(\frac{\partial C}{\partial x}\right)$, applies an alternating force at the drive frequency ω. The third term, $-\frac{1}{2}V_{AC}^2 e^{2i\omega t}\left(\frac{\partial C}{\partial x}\right)$, will apply a force to the graphene at twice the drive frequency, which will not be detected by our experimental measurement scheme.

This capacitive force will pull the graphene towards the substrate and increase the tension in the membrane. For a circular drumhead, the resonance frequency will depend on V_{DC} according to[68]

$$\omega_0^2(V_{DC}) = \left(\frac{\alpha}{R}\right)^2\left(\frac{\sigma_0}{\rho}\right) - \frac{\epsilon_0 V_{DC}^2}{\rho d^3} + \frac{\beta E h \epsilon_0^2 V_{DC}^4}{\rho d^4 T^2} \tag{3.4}$$

In which R is the resonator radius, T is the tension, Eh is the 2D elastic modulus, d is the distance between the membrane and the back gate, and α and β are dimensionless constants. The strength of the V_{DC}^2 term can be larger than the V_{DC}^4 term for applied DC voltages less than 8 V. In smaller resonators we find that the V_{DC}^4 term is mostly dominate and the effects from capacitive softening are not prominent in the measured spectrograph of $\omega_0(V_{DC})$, shown in **Figure 3.5**. We also note in some cases, the amplitude spectrograph is not exactly centered on the $V_{DC} = 0$ V, which is due to contaminants in the graphene membrane that shift the charge neutrality point[42].

We can also thermally tune and drive the resonators by focusing a pump laser onto the membrane with a DC offset and modulating the power. For a constant DC offset power, typically $P_0 \sim 50$ µW, the resonance frequency $\Delta\omega_0$ will shift with the change in membrane temperature ΔT as[55]

$$\Delta\omega_0 = \frac{\alpha Y \omega_0}{2\sigma_0(1-\nu)}\Delta T \tag{3.5}$$

in which α is the thermal expansion coefficient, ν is the Piosson ratio, σ_0 is the initial stress, and Y is the elastic modulus. If we instead we modulate the applied power with a frequency of ω as

$$P = P_0(1 + \cos(\omega t)) \tag{3.6}$$

we can modulate temperature of the membrane and thereby the tension. This causes an out of plane force on the membrane that is likely due to photothermal effects[69,70]. Because the thermal time constant of graphene has been measured to be of order nanoseconds[71], this method can be used to drive the out of plane motion of graphene resonators in the MHz regime near resonance.

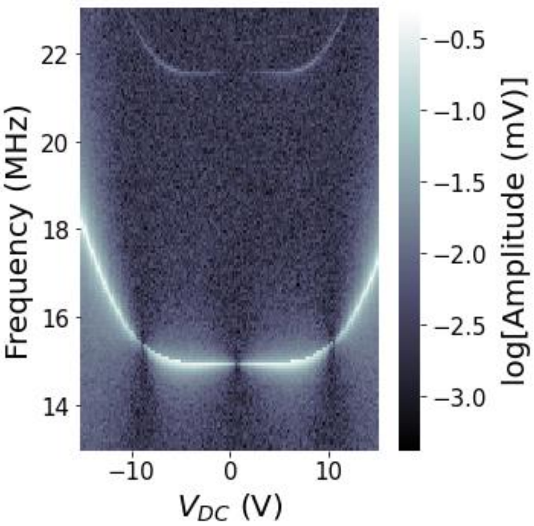

Figure 3.5: Tuning response of graphene resonator to applied electrical DC bias

Spectrograph of circular suspended graphene resonator with applied DC bias from −15 V to 15 V and drive frequency on y axis to show amplitude response of resonator. Fundamental mode is shown to tune from about 15 MHz at 0 V to 18 MHz at ±15 V. A second curve can be observed near 22 MHz, which corresponds to the second order mode of the driven resonator.

3.4 Interference measurement of amplitude and phase and SIM

To read-out the motion of the graphene resonators, we use an optical Fabry-Perot interferometer. In a Fabry-Perot interferometer, the interference signal is measured between an incident beam partially reflected by a semi-transparent mirror, or the suspended graphene, and by a reference mirror below, or the Si/SiO_2 substrate. As the graphene vibrates, the intensity of the interference signal will modulate due to the change in cavity length, or spatial distance between the suspended membrane and the substrate, indicating the amplitude of oscillation[72].

Because we cannot independently move the reference mirror, or the substrate, of the Fabry-Perot interferometer, further calibrations are required to translate the interference signal to an exact distance[73]. However, for this work the exact amplitude is not needed and we instead report amplitude as a voltage corresponding to the interference signal intensity. It is important to note, however, that with an interferometer measurement, we will observe the intensity of the measured reflected signal drop significantly when the distance between the graphene and the substrate are an odd integer multiple of the incident beam wavelength. This can be observed in **Figure 3.5**, as the graphene is tensioned with an applied DC bias and the cavity length is varied.

We implement the Fabry-Perot interferometer with a lab-built optical benchtop set-up. The laser in our interferometer, or the probe laser, is a 633 nm HeNe laser (ThorLabs S015B), which is shown in red in the optical schematic in **Figure 3.6**. The probe laser first travels through a half wave plate ($\lambda/2$) and is then reflected by a polarizing beam splitter (PBS). By adjusting the angle of the half waveplate, we can vary the power of the beam reflected by the PBS. The probe is then circularly polarized with a quarter waveplate ($\lambda/4$), such that upon back reflection, the linear polarization will be rotated $90°$ and can be coupled out of the original beam path through the PBS. The probe then passes through a lens pair to ensure the deflected beam remains centered on the objective. The beam is then focused onto the sample in a vacuum chamber with a spot size of ~ 1 μm through a 40x objective lens (Nikon CFI Plan Flour ELWD 40x/0.6). All measurements in this work were taken at room temperature under vacuum at $\sim 10^{-7}$ torr. The sample vacuum chamber is on a 3D motorized stage to focus and spatially align the sample. The probe is then partially reflected by the graphene and partially by the substrate, as described above for a Fabry-Perot interferometer. The reflected beam passes back through the quarter waveplate, and the resulting linear polarization allows for the beam to be transmitted through PBS and detected by an avalanche photodetector (ThorLabs PDS 10A Si Amplified Detector).

We used a lock-in amplifier (Zurich Instruments HF2) to extract resonator amplitude from the noisy current signal generated by the avalanche photodetector (APD). The lock-in amplifier mixes the input signal with a reference signal and extracts only the portion of the input that oscillates at the reference frequency. This reference frequency was also sent to the drive mechanism of the resonator, either electrically straight to the sample or to an RF generator to modulate the intensity of the pump laser. To drive a resonator electrically, we wire bonded the sample to a PCB board that was electrically connected to the lock in amplifier in the sample vacuum chamber. To drive a resonator optically, we modulated the pump laser intensity, shown in blue in the optical schematic in **Figure 3.6**, by using the lock-in reference signal to drive an acoustic optical modulator (AOM) (AA Opto Electronic MT350-A0.12-VIS). The pump laser, a 445 nm diode laser, was coupled into the probe laser beam path with a dichroic mirror (DCM). With the lock-in reference signal used to drive the resonator, we can also extract the relative phase between the drive and the resonator amplitude.

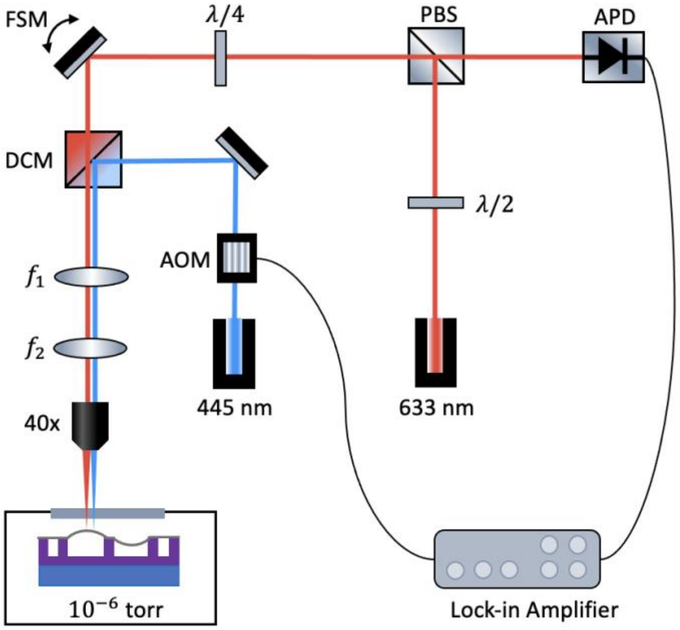

Figure 3.6: Optical pump/probe measurement schematic

Optical drive and measurement scheme. Pump laser path shown in blue starting at the 445 nm laser. Pump is modulated by an acoustic optical modulator (AOM), controlled by a lock-in amplifier, and coupled into the beam path with a dichroic mirror (DCM). The pump then travels through a lens pair, with focal lengths of f_1 and f_2, and is then focused on the sample with a 40x objective lens. The reflected pump signal is coupled back out of the optical path at the DCM. The probe laser path is shown in red starting at the 633 nm laser. The travels through a half wave plate ($\lambda/2$) and is then reflected by a polarizing beam splitter (PBS). The probe is then circularly polarized with a quarter waveplate ($\lambda/4$) and is reflected by a pair of fast scanning mirrors (FSM). The probe is coupled into the beam path with the DCM and passes through the lens pair onto the sample. The reflected probe then passes back through the quarter waveplate and is transmitted by the PBS into an avalanche photodetector (APD). The electronic signal from the APD is detected by the lock-in amplifier.

Along the probe laser path, we incorporated a pair of fast-scanning mirrors (ThorLabs GCM012), which is shown in the top left of **Figure 3.6**. This pair of fast-scanning mirrors (FSM) provided a means to spatially image the amplitude and phase of an area of the membrane, through a technique we refer to as scanning interference microscopy (SIM). SIM has previously been used to spatially image the amplitude and phase of driven MEMS and NEMS resonators, which has been especially important for visualizing higher order modes[64,74]. SIM is essential in our work to measure the amplitude and phase of coupled resonator clusters.

3.5 Phase lag in measurements

In the experimental measurement of the phase, there will be a lag caused by time delays of the optical and electronic signal transmission/transduction from the lock-in reference output to the input, shown in **Figure 3.7**a. The time-delay phase shift on the pump, τ_{force}, is the sum of delays due to the AOM controller, the AOM, and the free-space optical path and transmission cables up to the sample. The total time delay at the lock-in input, $\tau = \tau_{force} + \tau_{response}$, includes delays due to the photodetector, an "on-chip" thermal lag[64] and the free-space optical path and transmission cables from the device to the lock-in. There is also a constant phase lag due to the phase offset of the lock-in and a π phase lag that may arise depending on whether the membrane moves away from or toward the focusing objective[71]. These time delays and offsets will result in a frequency-dependent phase shift according to

$$\Delta(\omega) = \phi_0 - \omega\tau \tag{3.7}$$

Where τ is the total frequency dependent time delay and ϕ_0 is the total constant phase offset. The result of this phase lag is evident in the phase data as a linear offset, shown in **Figure 3.7b**.

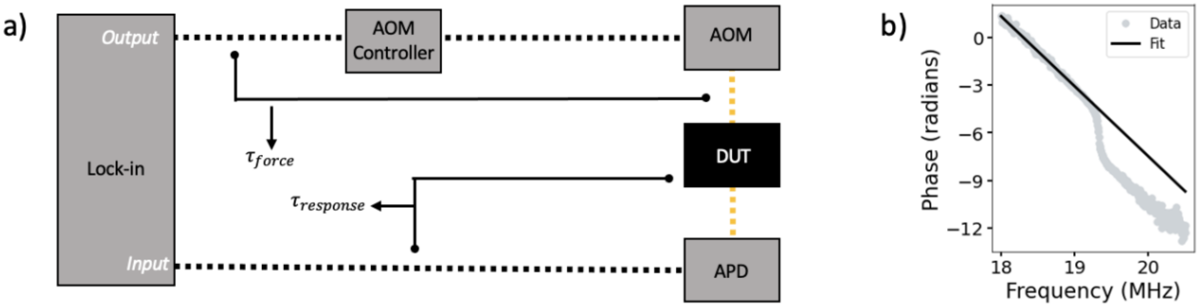

Figure 3.7: Experimental phase lag

a) Diagram of the experimental time delay phase shift. The time delay on the force, τ_{force}, includes delays due to transmission cables, shown as black dashed lines, the AOM controller, the AOM, and the free-space optical path before the device under test (DUT), shown as yellow dashed lines. The phase shift on the response, $\tau_{response}$, includes delays due to free-space optical path after the DUT, the APD, and transmission cables. **b)** Phase spectrum showing linear offset. Measured data shown as grey data points and linear fit to upper portion of plot shown as solid black line.

4 Novel platform for coupled NEMS resonator networks

In this chapter, we present our novel platform of coupled suspended graphene resonators. We show evidence of strong coupling between two and three resonators and higher order mode coupling between two spatially distinct resonators. This platform is the first to our knowledge to host strain induced strong coupling between 2D graphene drumhead resonators and fulfills the need of a scalable platform for NEMS resonator networks.

4.1 Introduction

Networks of coupled NEMS resonators have attracted recent attention for the promise of mechanical computing[31–33] applications and for studying fundamental physics, including metamaterial[24–26,28] and collective dynamics[17,18]. To continue to scale the size and prospects of coupled NEMS resonator networks, we need to develop robust platforms that host strong coupling and are scalable in size and tunability. Suspended graphene resonators offer many critical properties[46,48] that could be essential for achieving large 2D tunable arrays[58], such as intrinsic nonlinearities[68] that enable network dynamics[24,50,51,75] and multiple forms of energy transduction[76] for tuning options that have been demonstrated to scale resonance frequencies up to several hundred percent[42,77]. The persistent option of phototuning[42] has also recently been demonstrated, which opens the possibility for scalable tuning of large-scale graphene networks.

Many coupling schemes have been demonstrated to host tunable strong coupling between resonators by means of parametric[34,41] and electromechanical[35,63] coupling. However, these methods are limited in scalability because they are not persistent and often require individually addressing each resonator, which limits the dimension of scalability in these platforms. One coupling means that is persistent and scalable in 2D is direct mechanical strain coupling though a shared clamping point[19,39,78], bridge[17], or substrate[63]. Mechanical strain coupling has been demonstrated between spatially distinct graphene nanoribbons[36,60] but has been limited to a 1D linear chain. Direct strain coupling has been utilized to achieve a 2D network of coupled pillars[79], hinting that strain coupling may enable other material platforms to scale in 2D as well.

In this work, we present a 2D platform[75] that hosts persistent strain coupling between suspended graphene resonators. We show evidence of strong coupling between two and three resonators of varying sizes and locations, establishing the viability of the platform for diverse array-based resonator applications. Additionally, this platform accommodates rich dynamics with inter-resonator coupling of higher order modes, which we observed between the second order mode of a driven resonator and the fundamental mode of its neighbor. With this platform, we demonstrate a means in which the unique properties of 2D suspended graphene resonators can be accessed for a broad range of large-scale network applications.

4.2 Methods

To optimize the strain coupling between nearest neighbor suspended graphene resonators, we designed a pillar array substrate[75,80–82] as the base structure for the network. Throughout the arrays, we intermittently omitted specific pillars, such that the voids of missing pillars would form areas of larger suspended graphene to create resonators of different sizes and resonator pairs. The shared membrane between pillars provided a mechanism for mechanical strain coupling between spatially distinct resonators.

We chose pillar radii and pitch by using finite element analysis (FEA) to determine the eigenfrequencies of the symmetric (**Figure 4.1a**) and antisymmetric (**Figure 4.1b**) modes of resonator pairs. With the estimated eigenfrequencies, we could predict pillar parameters that would lead to strong coupling between neighboring resonators using the condition[83]

$$Q\left(\frac{\Delta\omega}{2\omega_0}\right) > 1 \qquad (4.1)$$

For which $\Delta\omega$ is the frequency difference between the first and second hybridized modes, ω_0 is the average of the two frequencies, and Q is the quality factor. In this calculation, we conservatively estimate the quality factor to be $Q = 100$ based on previously measured suspended graphene devices[42,55,64,84,85]. We selected a range of pillar radii ($0.25 - 0.75$ µm) and pitches ($1 - 3.75$ µm) for the arrays to be both spread-out enough to host strong coupling and dense enough to allow for successful graphene suspension. We were able to suspend the transferred graphene almost fully on the denser arrays, as in **Figure 4.1c**. Although overall we obtained higher yield on arrays with larger r/a ratios, we also observed certain areas of the

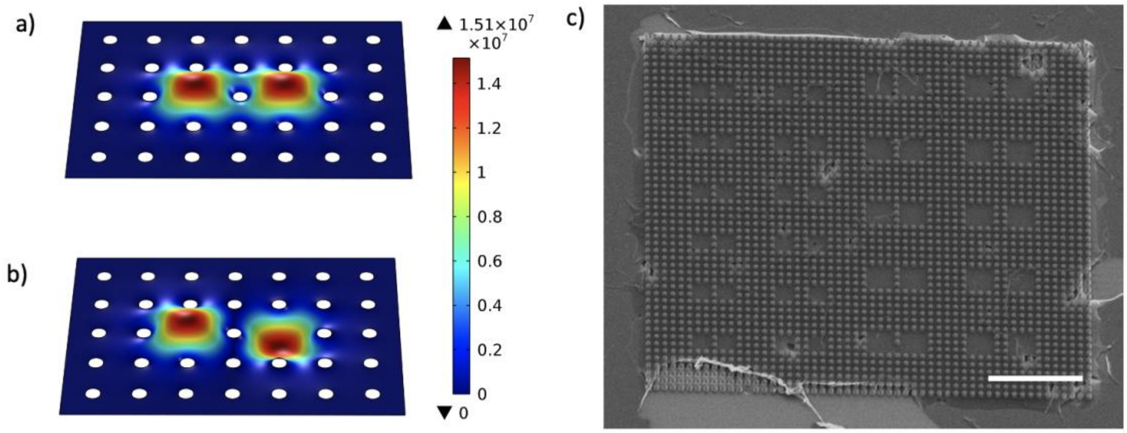

Figure 4.1: Design and fabrication of suspended graphene resonators

FEA simulations of **a)** symmetric and **b)** antisymmetric coupled resonator modes for pillar radius of 0.5 µm and pitch of 3 µm. **c)** SEM of suspended graphene resonators with pillar pitch of 1 µm and radius of 0.25 µm. Scale bar is 10 µm.

sample transfer better than others. As an example, **Figure 4.2a** shows an array with the same dimensions as in **Figure 4.1c** but located in a difference area of the sample and only partially covered with suspended graphene. The largest pitch with suspended graphene devices was 3.75 μm, shown in **Figure 4.2b**, and the largest r/a ratio was $0.5/3$, shown in **Figure 4.2c**.

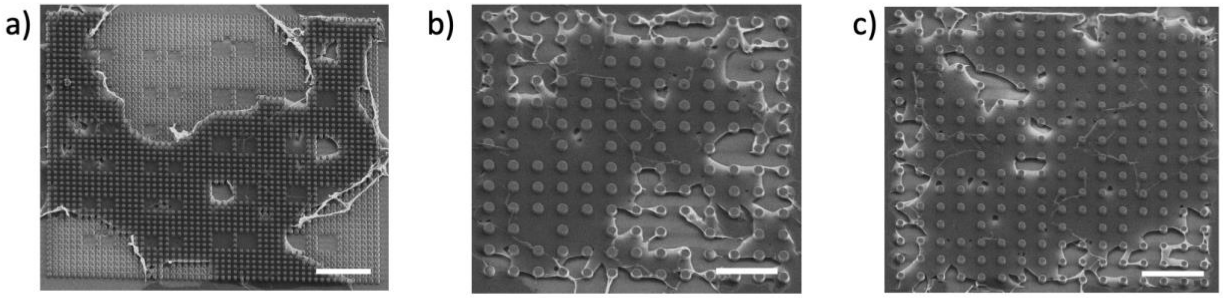

Figure 4.2: SEM images of suspended graphene on pillar arrays

a) Partial suspension of graphene over array with pillar radius of 0.25 μm and pillar pitch of 1 μm. **b)** Suspended graphene over array with pillar radius of 0.75 μm and pillar pitch of 3.75 μm. **c)** Suspended graphene over array with pillar radius of 0.5 μm and pillar pitch of 3 μm. All scalebars are 9 μm.

We used an optical pump/probe method to drive and measure the coupled graphene resonators and employed two methods of tuning to demonstrate the versatility in programming options for this platform. The pump used in our optical pump/probe method was a 445 nm laser modulated with an acousto-optic modulator (AOM) to thermally tension the graphene and drive out of plane motion. The probe was a 633 nm laser, in which the reflected interference signal was measured via lock in detection to extract the corresponding amplitude and phase of an oscillating resonator. Our optical set up also enabled scanning interference microscopy[64] (SIM) with fast scanning mirrors to raster the probe and collect spatial images of local areas of amplitude and phase.

We demonstrated the versatility of tuning options of our suspended graphene platform by employing two types of tuning methods. Our first tuning method was to optically tune the driven resonator only. For this individual tuning, we applied a DC offset to the modulated pump laser to thermally adjust the average tension of the driven graphene resonator. Our second tuning method was to electrically bias the entire sample and universally tune the tension of the suspended graphene, thereby tuning the resonance frequency of all resonators on the substrate. For this method of universal tuning, we applied a DC bias across the graphene and the doped Si sample below[76].

4.3 Results

To measure the coupling strength between two neighboring resonators, we employed our optical tuning method to acquire avoided crossing spectra. We started by aligning both the pump and probe lasers over the resonator region highlighted as R1 in **Figure 4.3a**. To determine the connectivity of this resonator, we measured a spectrograph of the out of plane amplitude of R1 by sweeping the drive frequency and the DC offset of the pump laser. In the resulting spectrograph, shown in **Figure 4.3b**, we observed an avoided crossing of a lower frequency mode, ω_-, and a higher frequency mode, ω_+, at a power offset of 2.8 V. This avoided crossing behavior implied that R1 was coupled with at least one neighboring resonator.

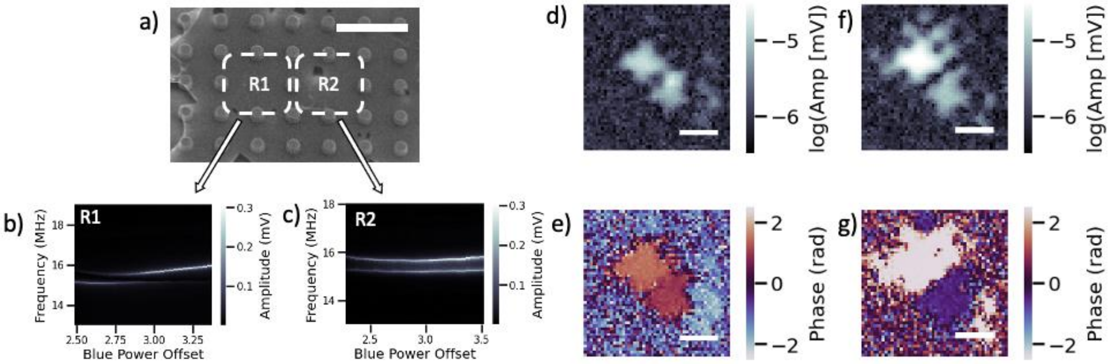

Figure 4.3: Strong coupling between two suspended graphene resonators

a) SEM image of two neighboring coupled resonators, R1 and R2. Scale bar is 6 μm. Avoided crossing with R1 driven for **b)** amplitude of R1 and **c)** amplitude of R2. SIM images of **d)** amplitude and **e)** phase for R1 driven at $\omega_-/2\pi = 15.45$ MHz. SIM images of **f)** amplitude and **g)** phase for R1 driven at $\omega_+/2\pi = 16.21$ MHz. All SIM scale bars are 5 μm.

To confirm that the source of the avoided crossing was mechanical, and to locate the coupled neighboring resonators, we took SIM images at both ω_- and ω_+ with a pump DC offset near the avoided crossing minimum to optimize each amplitude. To analyze the amplitude and phase behavior of R1 and R2 in each mode, we took a line cut of each SIM image through the center of the resonator pair. All errors are calculated standard error from the linecut data. In the ω_- mode, we observed two distinct amplitude peaks, **Figure 4.3d**, that corresponded to the locations of R1 and R2, highlighted in **Figure 4.3a**. Furthermore, we observed that these two regions oscillated near in phase (R1 $= 1.47 \pm 0.03$ rad and R2 $= 1.00 \pm 0.04$ rad), **Figure 4.3e**, which is expected for the lower frequency mode of two coupled resonators. In the ω_+ mode, we again observed two distinct amplitude peaks, **Figure 4.3f**, which corresponded to the same R1 and R2 locations. The two regions oscillated $\sim\pi$ out of phase (R1 $= 2.47 \pm 0.03$ rad and R2 $= -0.51 \pm 0.03$ rad), **Figure 4.3g**, as expected for the higher frequency mode of two coupled resonators.

To verify the coupling between R1 and R2, we measured a corresponding spectrograph of R2 by using the SIM spatial maps to reposition the probe laser over the R2 resonator, while leaving the pump laser stationary to drive R1. In the resulting R2 spectrograph, shown in **Figure 4.3c**, we again observed a lower and higher frequency mode that did not cross, with a minimum mode separation occurring at 2.9 V. This frequency was slightly higher than that for the R1 resonator, which may be due to heating and cooling affects associated with repositioning the probe laser. We also note that the avoided crossing curve shapes and amplitudes were less typical than observed in the R1 spectrograph, which may also be due to the probe repositioning. From the SIM spatial maps and the correlated avoided crossing curves, we conclude that the R1 and R2 resonators are coupled.

To determine the coupling strength, we calculated the minimum mode separation between ω_- and ω_+ as

$$g = \omega_+ - \omega_- = \Delta\omega \qquad (4.2)$$

Based on the R1 avoided crossing spectrograph, we calculated a coupling strength of $g/2\pi \approx 400$ kHz. Because this coupling strength exceeds the linewidths of the two modes (~ 150 kHz), we conclude this resonator pair is strongly coupled.

We measured strong coupling between an additional set of two resonators of different sizes using our universal tuning method. We first positioned the pump and probe laser over R1, highlighted in **Figure 4.4a**. To determine the connectivity of R1, we measured an amplitude spectrograph by sweeping the drive frequency and the universal DC bias, applied across the graphene and the Si substrate. In the resulting spectrograph, shown in **Figure 4.4b**, we observed an avoided crossing of two modes, ω_- and ω_+, at 6.4 V, implying that R1 was strongly coupled to at least one neighboring resonator. In this avoided crossing, we also observed that the ω_- mode tuned very little after the avoided crossing minimum. This behavior could be evidence of phototuning[42], as we may be redistributing charge in the contaminated graphene membrane[86] by applying a gate voltage while exposing the region to the high-powered pump laser.

To confirm mechanical strain coupling between R1 and any neighboring resonators, and to determine the coupled cluster configuration, we took SIM images at ω_- and ω_+ with zero applied voltage to optimize the amplitude of each mode. In the ω_- mode, we observed two distinct amplitude peaks, **Figure 4.4d**, that corresponded to the regions highlighted as R1 and R2 in **Figure 4.4a**. The R1 and R2 resonator regions differed significantly in size with $Area_{R1} \approx 4 \times Area_{R2}$. Because the frequency of the fundamental mode is typically higher for smaller area resonators ($\omega_0 \propto 1/L$ for a square membrane, see Appendix A for experimental data, it is possible that with additional tensioning from the pump laser on R1, the resonance frequency increased enough to match that of R2, resulting in coupling of the two regions. For the ω_- mode, R1 and R2 oscillated near in phase (R1 $= 1.79 \pm 0.07$ rad and R2$= 2.26 \pm 0.02$ rad), **Figure 4.4e**. In the ω_+ mode, we observed two distinct regions of amplitude, **Figure 4.4f**, that corresponded to the same R1 and R2 regions and oscillated $\sim\pi$ out of phase (R1$= 1.53 \pm 0.05$ rad and R2$= -1.82 \pm 0.04$ rad), **Figure 4.4g**. Based on the amplitude and phase behavior of R1 and R2 in each mode, we conclude that the two resonators are coupled.

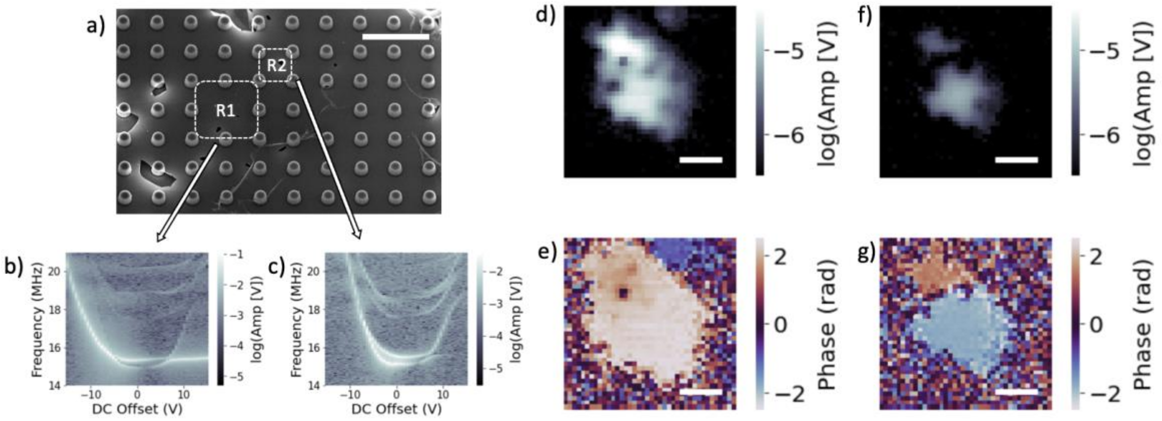

Figure 4.4: Strong coupling between additional set of two resonators

a) SEM image of neighboring coupled resonators, R1 and R2. Scale bar is 6 µm. DC bias gate sweep avoided crossings with R1 driven for **b)** amplitude of R1 and **c)** amplitude of R2. SIM images of **d)** amplitude and **e)** phase for R1 driven at $\omega_-/2\pi = 15.16$ MHz. SIM images of **f)** amplitude and **g)** phase for R1 driven at $\omega_+/2\pi = 15.51$ MHz. All SIM scale bars are 5 µm.

We confirmed the coupling by measuring a corresponding spectrograph of R2, **Figure 4.4c**, which displayed an avoided crossing between 6.4 V and 7.0 V, near to that of R1 with a slight difference likely due to the probe repositioning. Based on the R1 avoided crossing curve, we calculated the coupling strength between R1 and R2 to be $g/2\pi \approx 200$ kHz. With estimated linewidths of ~ 120 kHz at the avoided crossing minimum, we conclude this resonator pair is strongly coupled.

Our pillar platform offers a high potential for 2D scalability, which we demonstrate with evidence of coupling between three adjacent resonators. With the pump and probe lasers aligned over R2, highlighted in **Figure 4.5a**, we swept the drive frequency to locate resonance. In the resulting amplitude curve, shown in **Figure 4.5b** upper, we observed two closely spaced but distinct peaks. To determine whether these two peaks signified hybridized modes, we took SIM spatial images of the amplitude and phase at ω_- and ω_+. In the ω_- mode, we observed three distinct amplitude peaks, **Figure 4.5c**, that were all oscillating near in phase (R1 $= 0.23 \pm 0.13$ rad, R2 $= 0.20 \pm 0.03$ rad, and R3 $= 0.41 \pm 0.04$ rad), **Figure 4.5d**, implying coupling between a total of three resonators. Again, the observed oscillating regions, highlighted as R1, R2, and R3 in **Figure 4.5a**, differed in size with the largest resonator, R2, subject to additional tensioning from the applied pump laser. In the ω_+ mode, we observed three distinct amplitude peaks, **Figure 4.5e**, in the same R1, R2, and R3 regions. However, the two neighboring resonators, R1 and R3, oscillated out of phase with driven R2 resonator (R1 $= -0.23 \pm 0.17$ rad, R2 $= 2.08 \pm 0.02$ rad, and R3 $= -0.62 \pm 0.18$ rad), **Figure 4.5f**.

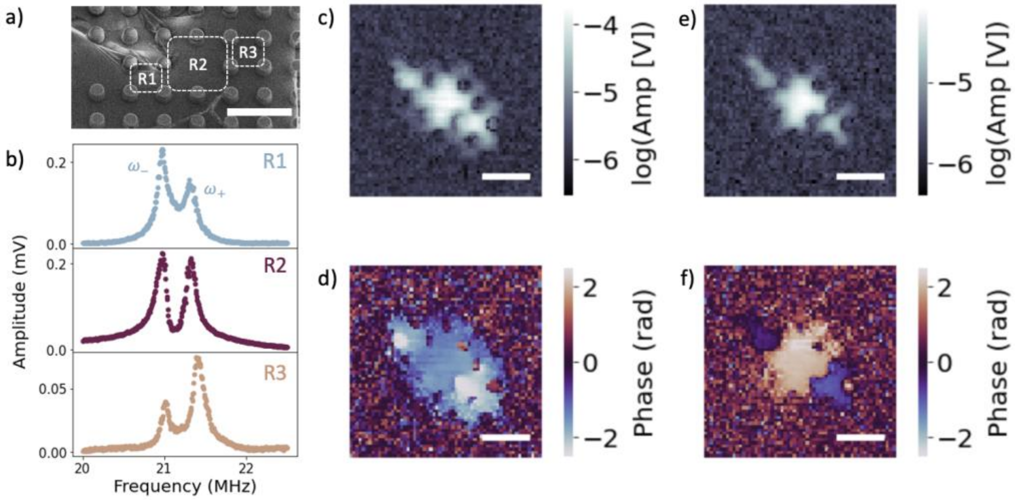

Figure 4.5: Coupling between three resonators

a) SEM image of three coupled resonators, R1, R2, and R3. Scale bar is 5 μm. **b)** Spectra of R1 (upper), R2 (middle), and R3 (lower). SIM images of **c)** amplitude and **d)** phase with R2 driven at $\omega_1/2\pi = 20.99$ MHz. SIM images **e)** amplitude and **f)** phase with R2 driven at $\omega_2/2\pi = 21.45$ MHz. All SIM scale bars are 5 μm.

Typically, we expect three strongly coupled resonators to have three hybridized modes based on the eigenvectors of a linear chain of masses and springs. Therefore, because we only observed two modes in the spectra of the coupled system in **Figure 4.5**, it is possible that there is weak coupling present in the system, or mode splitting that is unresolvable in the spectra[83]. However, by modeling the three drumhead resonators as a linear chain of masses and springs with an applied drive force, we find that it is possible for only two hybridized modes to emerge, even when all three resonators are strongly coupled.

In our linear mass and spring model, each mass had an intrinsic spring and was connected to the nearest neighbor mass through a coupling spring. We set all masses and spring constants to be equal and we set the damping to be one order of magnitude less than the individual resonance frequencies $\omega_0 = \sqrt{k/m}$. We found that when the drive force was applied to one of the edge masses, the eigenvector behavior of three coupled masses emerged; three hybridized modes in which all masses oscillated in phase for the first mode, the outer masses oscillated in phase and the center mass was stationary for the second mode, and finally the outer masses oscillated in phase and the center mass oscillated out of phase for the third mode. Simulated amplitude and phase spectra are shown for the outer masses in **Figure 4.6a,c** and for the middle mass in **Figure 4.6b**.

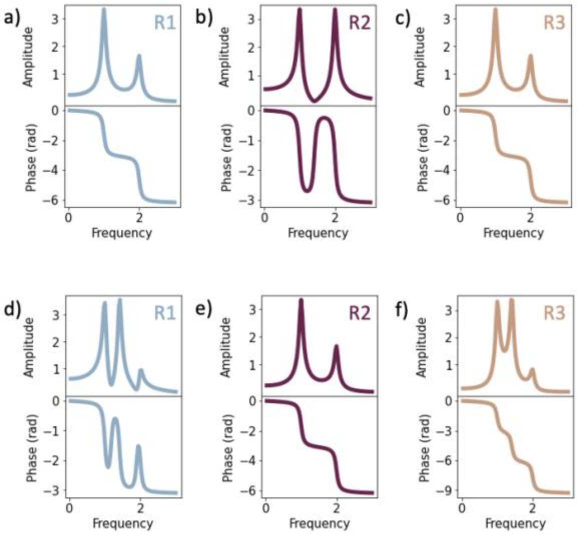

Figure 4.6: Simulated spectra from three coupled resonator model

Simulated amplitude (upper) and phase (lower) spectra for three mass model with $k_1 = k_2 = k_3 = 1$ N/m, $m_1 = m_2 = m_3 = 1$ kg, $c_1 = c_2 = 1$ N/m, $g_1 = g_2 = g_3 = 0.1$ kg/s, and $F = 1$ N. Plotted for the case of the drive force applied to the middle mass for **a)** driven edge mass, **b)** middle mass, and **c)** last edge mass. Simulated amplitude (upper) and phase (lower) spectra for three mass model for the case of the drive force applied to one of the edge masses for **d)** first edge mass, **e)** driven middle mass, and **f)** last edge mass.

With the same parameter values, we repeated this simulation for the drive force applied to the middle mass, as was the case for the coupled system in **Figure 4.5**. In this simulation, we observed only two hybridized modes, in which all masses oscillated in phase for the first mode, and the outer masses oscillated in phase while the middle mass oscillated out of phase for the second mode. This mode behavior persisted provided that the outer two resonators were symmetric in mass and intrinsic spring constant. Simulated amplitude and phase spectra are shown for the outer masses in **Figure 4.6d,f** and for the middle mass in **Figure 4.6e**. This matches the behavior observed in the three measured graphene drumhead resonators in **Figure 4.5**.

We therefore conclude that although only two modes were detected, it is possible that the three measured graphene resonators were strongly coupled.

To confirm this coupling, we measured an amplitude spectrum of R1, shown in **Figure 4.5b** (middle), and R3, shown in **Figure 4.5b** (lower). In all three amplitude spectra, we observe two peaks at about the same ω_- and ω_+ frequencies. We therefore conclude that this cluster of three resonators – R1, R2, and R3 – are weakly to strongly coupled.

Our pillar platform offers unique 2D coupling dynamics between resonators including the inter-resonator coupling of higher order modes. We detected higher order mode coupling by first measuring the amplitude spectrum of R1, highlighted in **Figure 4.7a**. In the spectrum, shown in **Figure 4.7c** (upper), we measured a single peak, ω_0, close to 14 MHz, and two closely paced peaks, ω_- and ω_+, near 17 MHz, implying that coupling may occur at a higher order mode of R1.

To better visualize the spatial dynamics and investigate the possibility of higher order mode coupling, we took SIM images at drive frequencies of ω_0, ω_-, and ω_+. In the ω_0 mode, we observed a region of high amplitude ($\sim 10^{-4}$ V) with near constant phase, **Figure 4.7d,e**, corresponding to the R1 region highlighted in **Figure 4.7a,b**, which we interpret to be the fundamental mode of R1. In the ω_- mode, we observed three

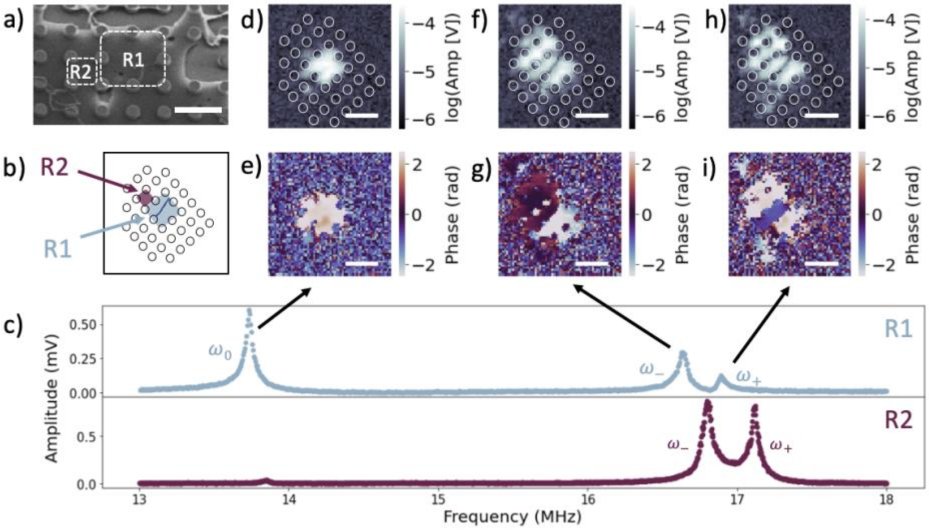

Figure 4.7: Inter-resonator higher order mode coupling

a) SEM image of two coupled resonators, R1 and R2. Scale bar is 4.5 μm. **b)** Dot array rotated at the same angle as SIM images. R1 labeled with blue shading and blue solid line to represent higher order mode boundary. R2 labeled with maroon shading. **c)** amplitude spectrum of R1 plotted with blue data points (upper) and amplitude of R2 plotted with maroon data points (lower). Amplitude peaks labeled as ω_0, ω_-, and ω_+ in R1 spectrum. SIM images of **d)** amplitude and **e)** phase with R1 driven at $\omega_0/2\pi = 13.85$ MHz. SIM images of **f)** amplitude and **g)** phase with R1 driven at $\omega_-/2\pi = 16.74$ MHz. SIM images of **h)** amplitude and **i)** phase with R1 driven at $\omega_+/2\pi = 16.97$ MHz. All SIM scale bars are 8 μm.

distinct regions of amplitude, **Figure 4.7f**. Two of the peak amplitude regions occurred within the R1 boundary, with the resonator boundary shown as a dotted line in **Figure 4.7b** and the mode boundary shown as a solid line. The phase between the two amplitude peaks within the R1 region, **Figure 4.7g**, differed by $\sim\pi$ (left half $= 0.30 \pm 0.10$ rad and right half $= -2.46 \pm 0.07$ rad), as expected for the second order mode of a 2D graphene drumhead resonator[64]. The third amplitude peak corresponded to the region highlighted as R2 in **Figure 4.7a,b**. R2 oscillated near in phase with the left half of the R1 resonator (R2 $= 0.45 \pm 0.38$ rad), **Figure 4.7g**. This phase pattern creates the least amount of curvature in the membrane for the case of coupling a fundamental mode to a second order mode and is therefore expected to correspond to the lower energy state.

In the ω_+ mode, we again observed three distinct amplitude peaks, **Figure 4.7h**. However, in this mode R2 oscillated out of phase, **Figure 4.7i**, with the left half of the R1 resonator and near in phase with the right half (R2 $= 1.96 \pm 0.37$ rad, left half of R1 -0.93 ± 0.07 rad, and right half of R1 $= 2.49 \pm 0.18$ rad). This phase pattern creates more curvature in the membrane and is therefore expected to result in a higher energy state that is excited at a higher frequency. Higher order mode coupling between these two resonators may be possible due to the differing sizes of R1 and R2.

To confirm this coupling, we measured an amplitude spectrum of R2, shown in **Figure 4.7c** (lower). In this spectrum, we observed a small peak ($\sim 4 \times 10^{-5}$ V) near the fundamental mode of R1 and two much larger peaks ($\sim 9 \times 10^{-4}$ V) around ω_- and ω_+, with slight shifts due to heating. Due to this amplitude difference, and the homogeneous phase behavior observed in both the ω_- and ω_+ modes, we consider that the small peak near the fundamental mode of R1 does not correspond to a resonance of R2. We therefore conclude that the mode splitting observed in the spectra around 17 MHz is due to coupling between the second order mode of the driven resonator R1 and the fundamental mode of R2.

4.4 Discussion

In conclusion, we present evidence of strong coupling between sets of two resonators, thereby establishing this graphene network as a platform for coupled NEMS resonators. The additional evidence of coupling between three resonators indicates the 2D scalability potential of this platform.

We demonstrate the tunability of this platform by tensioning the resonators both thermally and electrically to collect avoided crossing spectrographs. The coupling observed between resonators asymmetric in size may be advantageous for tuning neighboring coupled resonators at different rates under a universally applied back gate. This graphene platform also has the potential for scalable phototuning[42], which would enable persistent and individual tensioning of suspended graphene regions without the need for individual back gates. Additionally, because we utilize mechanical strain coupling, if the shared membrane between neighboring resonators were to be tensioned, with any of the discussed methods, we could tune the coupling strength between resonators. Tunable coupling is an essential component for programmable network applications.

The additional evidence of inter-resonator higher order mode coupling highlights the possibility of rich dynamics that are an asset unique to this graphene platform. Coupling between higher order modes of spatially separate resonators can be utilized as means of achieving distinct coupling configurations through a single driven resonator. It could also be utilized as a means of achieving coupling between resonators of different sizes without additional thermal tensioning for the use of asymmetric tuning with a universal back gate.

Although we focused our analysis on strong coupling that led to detectable mode splitting, in the SIM spatial maps we observe additional oscillating regions revealing areas of weak coupling. Weak coupling is an important aspect to consider when designing a NEMS resonator network as it can be essential for realizing many oscillator-based phenomena, such as synchronization and exotic states[18], or can highlight areas of energy leakage in a desired isolated cluster. Although weak coupling is often difficult to measure, as it is not detectable in spectra[83], our SIM spatial imaging technique illuminates weakly coupled regions, allowing us to include weak coupling when modeling detected coupling configurations.

4.5 Conclusion

In conclusion, we have presented evidence of coupling between multiple sets of two resonators, three resonators, and inter-resonator coupling a higher order mode. This 2D suspended graphene platform thus enables rich coupling dynamics through persistent strain coupling with potential for high tunability and scalability due to the unique properties of suspended graphene resonators. With this platform, we can achieve large-scale arrays with persistent coupling for applications such as computing schemes[31–33], experimentation of tunable metamaterial[24,25,27,87], and physical simulation of natural and artificial networks[5,10].

5 Characterization of coupled NEMS resonator networks

In this chapter, we present our characterization technique for spatially mapping all the physical parameters of a coupled resonator network. We apply this technique to characterize single suspended graphene resonators and coupled suspended graphene resonator pairs. With this scalable characterization method, we provide an essential tool for diagnosing the current state of a network. Because a spatial map provides information of both where to tune the network and by how much, this characterization method is an important step towards experimentally realizing programmable NEMS resonator networks.

5.1 Introduction

Interacting many-body systems are abundant in nature at a variety of length scales, from atomic solids to celestial bodies, and comprise a growing number of diverse synthetic systems such as solid-state and optical qubit arrays [8], photonic/phononic crystals[88,89], and neural networks[90]. Thus, synthetic many-body systems are central to numerous hot-topic applications ranging from neuromorphic and quantum computing[91,92] to strongly correlated phases[93] and metamaterials[94]. Consequently, there is a vibrant effort to understand, control, and engineer the collective behavior of these interacting systems. A compelling experimental analog for these assemblies is the programmable network of nanoelectromechanical (NEMS)[95] resonators. In addition to serving as a testbed, a programmable NEMS network would also unlock powerful applications such as reconfigurable phononic crystals and waveguides[24,28], tunable thermal transport [26], and mechanics-based circuits[18], computing and simulation[32,95]. Recent advancements towards realizing NEMS networks include demonstrations of collective phenomena in small-scale modular assemblies[18] and lattices[26,95] and the development of scalable tools to tune the resonance frequency of individual resonators[42] and the coupling between pairs[60].

A fundamental obstacle in the advancement of NEMS networks, and other network platforms, is the lack of tools to accurately characterize and spatially resolve the parameters of each network building block and their interactions. NEMS characterization is traditionally performed by analyzing resonance peaks in displacement spectra. For example, amplitude spectra near resonance can be used to quantify the dissipation and eigenfrequency of single resonators[42] and to ascertain coupling strengths between resonators[41]. However, as the size of the network is expanded—even modestly—it becomes increasingly challenging to deduce the spatial configuration of a coupled network from spectra alone [40], thereby frustrating efforts to characterize and tune specific resonators. Moreover, weak coupling—an essential feature of many collective phenomena[5,18,96]—is challenging to detect spectroscopically because of its small signal and indistinguishable mode splitting[83], while spurious non-mechanical spectral features often confound characterization attempts[18]. In addition, network parameters inferred from spectral data using traditional analysis approaches (*e.g.* non-linear least square) require *a priori* knowledge of the network parameters as input guesses to achieve reasonable model predictions. Even so, correlations and local least-squares minima often lead to large uncertainties in the output parameters[43].

Here we demonstrate a site-specific method to quantify the parameters – elasticity, mass, damping, and coupling – in a nanomechanical network that overcomes the limitations of current approaches. In our method, which we call NetMAP (Network Mapping and Analysis of Parameters), we first employ optical scanning interference microscopy[26,51,64,97] (SIM) to spatially image the amplitude and phase response of hybridized vibrational modes in a network of nanomechanical graphene drumhead resonators. The resulting SIM images provide the spatial address of each resonator in the network, which we use to measure fixed-frequency response vectors. Using just two vectors, we solve the network's reciprocal-space equations of motion to determine all the mechanical parameters of the network without any *a priori* knowledge. The algebraic analysis method of NetMAP can characterize any resonator network, regardless of the underlying physical domain. Moreover, the combination of our graphene resonator arrays, NetMAP, and existing methods to tune resonators[42] establishes a viable platform for programmable nanomechanical networks.

5.2 Mathematical background

In our approach, we model the resonator network as a linear chain of masses and springs, depicted in **Figure 5.1a.** The system of equations describing this model can be organized into matrix form, as described previously in Eq.(2.1), and rewritten below as

$$\boldsymbol{M}\ddot{\vec{x}} + \mathbf{B}\dot{\vec{x}} + \boldsymbol{K}\vec{x} = \vec{F} \qquad (5.1)$$

where $\boldsymbol{M}$, $\boldsymbol{B}$, and $\boldsymbol{K}$, are the mass, damping, and elasticity matrices, respectively. Using $x_n(t) = |Z_n(\omega)|e^{i(\omega t - \phi_n(\omega))}$ as the response of the n^{th} resonator, we can write Eq(5.1) in steady-state form:

$$\boldsymbol{\mathcal{M}}(\omega)\vec{Z}(\omega) = \vec{F} \qquad (5.2)$$

Here ω is the drive frequency of $\vec{F}$, $\boldsymbol{\mathcal{M}}(\omega) \equiv -\omega^2\boldsymbol{M} + i\omega\boldsymbol{B} + \boldsymbol{K}$, and $\vec{Z}(\omega)$ is a vector of the complex responses of each resonator in the network, $Z_n(\omega)$. Our approach determines $\boldsymbol{M}$, $\boldsymbol{B}$, and $\boldsymbol{K}$ by measuring the response vector $\vec{Z}(\omega)$. For finite clusters of size N, $\boldsymbol{\mathcal{M}}(\omega)$ has $4N$ unknown parameters; N masses, N damping constants, N intrinsic springs, $N-1$ coupling springs, and 1 force (assuming one driven resonator). For each measurement of $\vec{Z}(\omega)$, Eq.(5.2) provides $2N$ equations due to the real and imaginary part of each equation of motion. Thus, to determine the unknown parameters of $\boldsymbol{M}$, $\boldsymbol{B}$, and $\boldsymbol{K}$, $\vec{Z}(\omega)$ must be measured at a minimum of two drive frequencies, ω_a and ω_b. When a resonator's motion is undetectable, the number of linear equations is reduced; if the undetectable resonator is in the interior of the cluster, six equations are lost, while if at the edge of the cluster four equations are lost. Therefore, it is important to ensure that all resonators have a measurable amplitude at the two driving frequencies, or to otherwise include measurements at additional driving frequencies.

We combine and reorganize the equations corresponding to $\vec{Z}(\omega_a)$ and $\vec{Z}(\omega_b)$ in Eq.(5.2) to obtain

$$\boldsymbol{\mathcal{Z}}\vec{p} = \vec{0} \tag{5.3}$$

where $\boldsymbol{\mathcal{Z}}$ is a $4N \times 4N$ real-valued matrix of known coefficients determined by ω_a, ω_b, $\vec{Z}(\omega_a)$, and $\vec{Z}(\omega_b)$. The *parameters vector*—$\vec{p}$—is an $4N$-dimensional vector comprised of all the unknown elements of $\boldsymbol{M}$, $\boldsymbol{B}$, $\boldsymbol{K}$, and $\vec{F}$.

To solve Eq.(5.3) for $\vec{p}$, we determine the null space of $\boldsymbol{\mathcal{Z}}$ via singular value decomposition (SVD). We use the `NumPy` SVD package in Python, which outputs normalized values of $\vec{p}$ that can be used to calculate any ratio of interest (*e.g.* the quality factor, coupling strength, etc.) and to plot the predicted $\vec{Z}(\omega)$ to validate against measurement. The normalized values in $\vec{p}$ can be un-normalized by separately determining one parameter. We can also use SVD to solve an overdetermined system of equations if measurements are taken at additional drive frequencies.

5.3 Methods

We demonstrate NetMAP on network clusters of graphene resonators suspended over pillar arrays. We created the arrays by patterning SiO_2/Si substrates using e-beam lithography followed by a dry reactive ion etch (CHF_4), resulting in SiO_2 pillars ~ 600 nm in height. We then suspended commercially grown CVD graphene over the pillar arrays using a wet transfer method[82], resulting in an array of interconnected, suspended graphene resonators, shown in one configuration in **Figure 5.1b**. Additionally, we omit pillars throughout the array to create larger-size resonators and resonator pairs (**Figure 5.1e,c**). The lateral size of the membrane resonators varies from $3 - 6$ µm. The resonators are directly connected by suspended graphene, which provides a mechanism for elastic coupling represented by the coupling spring constants, c_n, in **Figure 5.1a**.

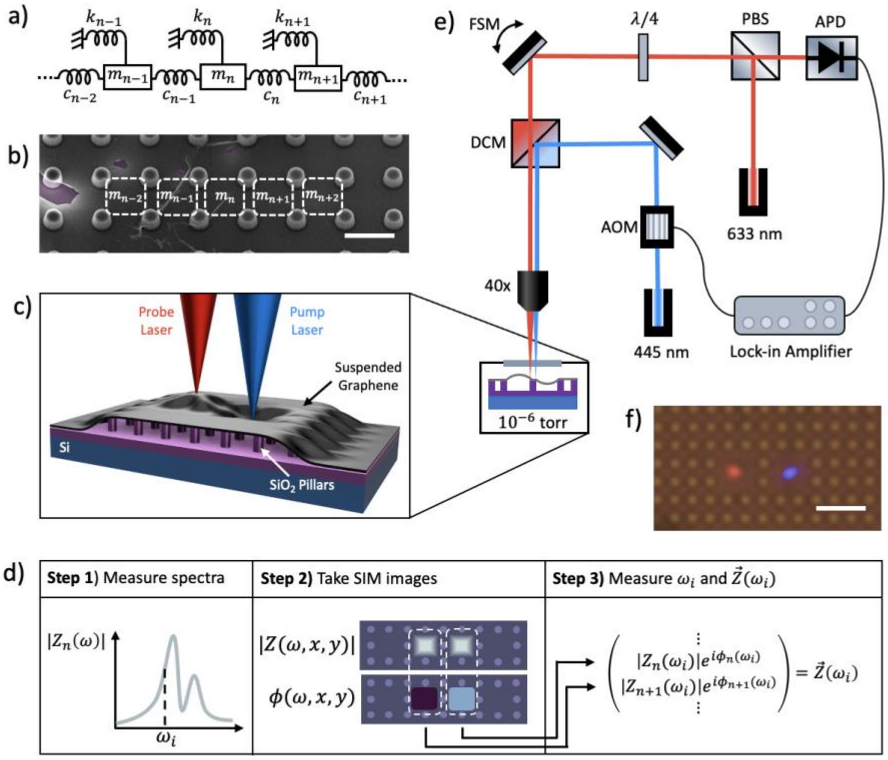
a)
k_{n-1}
k_n
k_{n+1}
m_{n-1}
m_n
m_{n+1}
c_{n-2}
c_{n-1}
c_n
c_{n+1}
b)
m_{n-2}
m_{n-1}
m_n
m_{n+1}
m_{n+2}
c)
Probe Laser
Pump Laser
Suspended Graphene
Si
SiO$_2$ Pillars
10^{-6} torr
e)
FSM
$\lambda/4$
PBS
APD
DCM
AOM
633 nm
40x
445 nm
Lock-in Amplifier
f)
d)
Step 1) Measure spectra
Step 2) Take SIM images
Step 3) Measure ω_i and $\vec{Z}(\omega_i)$
$|Z_n(\omega)|$
ω_i
$|Z(\omega,x,y)|$
$\phi(\omega,x,y)$
$|Z_n(\omega_i)|e^{i\phi_n(\omega_i)}$
$|Z_{n+1}(\omega_i)|e^{i\phi_{n+1}(\omega_i)}$
$= \vec{Z}(\omega_i)$

Figure 5.1: Suspended graphene platform and measurement scheme

a) Linear mass and spring model showing intrinsic springs (k_n), coupling springs (c_n), and masses (m_n). **b)** SEM image of graphene suspended over pillars. Suspended regions between pillars are depicted as a linear chain of masses. Scale bar is $3\ \mu m$. **c)** Cross section view of suspended graphene device showing Si base with SiO$_2$ pillars and suspended graphene. The depicted pump and probe lasers are aligned to drive the right-side resonator and measure the motion of the left-side resonator. **d)** Steps for measuring $\vec{Z}(\omega_i)$ showing (1) an amplitude spectrum of the n^{th} resonator, (2) spatial images of a cluster of two resonators, and (3) the complex response vector of the cluster when driven at ω_i. **e)** Schematic of optical set up showing 445 nm pump laser modulated with an AOM and coupled into the optical path with a dichroic mirror (DCM). The 633 nm probe laser is deflected by a polarizing beam splitter (PBS) and polarized by a quarter waveplate ($\lambda/4$). The probe position is controlled with a fast-scanning mirror (FSM). The reflected probe passes back through the PBS, and the interference signal is detected by an avalanche photodiode (APD) and resolved by a lock-in amplifier. Both the pump and probe lasers are focused onto the sample through a 40x objective lens and the sample is under vacuum at 10^{-6} torr. **f)** Top-down optical image of the sample under vacuum, with pillars seen as small orange dots. Here, the pump (blue) and probe (red) beams are focused onto neighboring resonator regions of suspended graphene, with a scalebar of 6 μm.

With the goal of determining $\vec{p}$ for a local cluster of suspended graphene resonators, we must first construct the matrix $\boldsymbol{\mathcal{Z}}$, which we achieve in three steps (**Figure 5.1d**): (1) Determine the drive frequency ω that provides large signal-to-noise ratio (SNR) for $|Z_n(\omega)|$, (2) quantify the size and spatial configuration of the cluster, and (3) measure $\vec{Z}(\omega_a)$, $\vec{Z}(\omega_b)$ and use ω_a, ω_b, $\vec{Z}(\omega_a)$, $\vec{Z}(\omega_b)$ to construct $\boldsymbol{\mathcal{Z}}$.

The first step is to determine which drive frequencies ω provide a large response signal $|Z_n(\omega)|$, which we achieve by measuring amplitude and phase spectra of the n^{th} resonator and searching for resonance peaks (**Figure 5.1d,** Step 1). To measure the spectra, we position a focused optical pump (445 nm) and probe (633 nm) on the n^{th} resonator. While modulating the pump with an AOM, we measure the corresponding amplitude and phase via interferometry and lock-in amplification (see **Figure 5.1c,e,f**). All measurements are taken in vacuum ($\sim 10^{-7}\ torr$) at room temperature. From the resulting spectra, we locate resonance peaks to determine a range of frequencies that provide a large $|Z_n(\omega)|$. To further increase the signal $|Z_n(\omega)|$, we increase the amplitude of the pump laser until $|Z_n(\omega)|$ is just below the limit of the linear regime. For all further measurements and steps, we fix the coordinates of the pump at this initial position.

Second, we quantify the size N and spatial configuration of the cluster by obtaining images of the mechanical motion of the area surrounding the driven resonator via scanning interferometric microscopy (SIM)[64]. For SIM, we modulate the fixed pump at a value of ω, chosen to correspond to a large signal in the measured amplitude spectrum. We then raster the probe across the sample while recording both amplitude and phase, resulting in two-dimensional spatial images $|Z(\omega, x, y)|$ and $\phi(\omega, x, y)$ (**Figure 5.1d,** Step 2). SIM images are taken over a large enough area to characterize the local vicinity of the driven resonator, typically about 20 µm × 20 µm in size. To quantify N, we use $|Z(\omega, x, y)|$ and $\phi(\omega, x, y)$ to count the number of resonators in the cluster, corresponding to the number of regions that have local amplitude maxima and constant phase. To confirm N and map the spatial configuration of the cluster, we cross-correlate $|Z(\omega, x, y)|$ with an optical brightfield (**Figure 5.1f**) and SEM (**Figure 5.1b**) image to match peak amplitudes with specific areas of the suspended membrane. Our home-built SIM software allows for easy point-and-click positioning of the probe, which we use to collect spectra (step one) for each resonator in the cluster. With a full set of spectra, we determine which frequencies ω result in a largest overall response signal. Moreover, we use the point-and-click positioning feature to finely tune the x-y probe coordinates over each resonator to further maximize the signal.

The third and final step is to measure the components of $\boldsymbol{\mathcal{Z}} -$ constructed with $\omega_a, \omega_b, \vec{Z}(\omega_a), \vec{Z}(\omega_b)$. To obtain the first set $\left(\omega_a, \vec{Z}(\omega_a)\right)$, we position the probe on the n^{th} resonator, but rather than fixing ω_a and measuring $Z_n(\omega_a)$, we use a phase-locked loop (PLL) to monitor the time series of frequency and amplitude, $\Omega_n(\omega_a)$ and $A_n(\omega_a)$, for a fixed phase input of $\phi_n(\omega_a)$. The phase input is determined by the value of the phase spectrum at the target ω_a. We record each time series until the amplitude SNR reaches a predetermined value of $\sim 10^3$, typically resulting in $\sim 10^4$ discrete measurements. We define the SNR as the ratio of the mean of the series to the standard error ($|\bar{A}|/\sigma_{\bar{A}}$). Although the best choice of a target ω_a for high SNR would be at the peak resonance, we chose frequencies slightly off resonance to reduce error from frequency-dependent linear phase lags intrinsic to the optical set up, discussed in **Section 3.5**. Additionally, the phase must be corrected for this lag prior to calculating $Z_n(\omega_a)$**.** We correct the phase by linearly fitting a region of the phase spectrum far off resonance to determine an intercept, ϕ_0, and the time delay slope, τ. We then subtract the quantity $\phi_0 - \omega_i \tau$ from the PLL input phase and calculate a phase error based on the uncertainty in the fitted linear section[98].

$$\sigma_\phi = \sqrt{\frac{1}{N-2}\sum\nolimits_{i=1}^{N}(\phi_i - \phi_0 - \tau\omega_i)^2} \tag{5.4}$$

After repeating this PLL measurement for all N resonators in the cluster, we calculate $(\omega_a, \vec{Z}(\omega_a))$ as $\omega_a = \sum_{n=1}^{N}\frac{\bar{\Omega}_n(\omega_a)}{N}$ and $\vec{Z}(\omega_a) = \{\overline{A_1}e^{i\phi_1(\omega_a)}, \dots, \overline{A_N}e^{i\phi_N(\omega_a)}\}$, in which we use the corrected phase values, $\phi_n(\omega_a)$, and the time series averages, $\bar{\Omega}_n(\omega_a)$ and $\overline{A_n}(\omega_a)$. We repeat this procedure to calculate $\left(\omega_b, \vec{Z}(\omega_b)\right)$, completing all the measurements needed to calculate the components of $\boldsymbol{\mathcal{Z}}$**.**

5.4 Results for resonator clusters of size $N = 1$

As a first application of NetMAP, we determined the mechanical parameters of the simplest network cluster of size $N = 1$, corresponding to a single, uncoupled resonator. We first position the pump and probe over the resonator region highlighted in **Figure 5.2a** and acquire amplitude and phase spectra. The resulting spectra revealed a single peak in the amplitude, shown as grey data points in **Figure 5.2f** (upper), that corresponded to a corrected phase of $\pi/2$ (**Figure 5.2f** (lower), grey)**,** consistent with a single, uncoupled resonator. To confirm the size of this cluster was $N = 1$, we took a SIM scan at 18.81 MHz, resulting in the amplitude and phase spatial maps shown in **Figure 5.2.** In the amplitude map, we observed an amplitude maximum ($\sim 10^{-4}$ mV) within one localized $\sim 6 \times 6\ \mu m^2$ region of the suspended graphene, which matched the size and location of the region highlighted in **Figure 5.2a**. The spatial undulations in the amplitude and phase near the edge of the resonator region are likely due to interactions with the pillars. Outside of the resonator region, the amplitude decreases by more than two orders of magnitude ($\sim 10^{-6}$ mV). Moreover, the resonator region has nearly constant phase ($STD = 0.07$ rad), implying it moves in unison, as expected for the fundamental mode of a single resonator. Away from the resonator, the phase is noisier ($F_0 \sim 74,\ p \sim 10^{-11}$), with an increase in the standard deviation by over an order of magnitude ($STD = 0.6$ rad). Lastly, as seen in the line scans (**Figure 5.2b,c**), the amplitude has one solitary lobe with constant phase. Altogether, we conclude that this local cluster consists of a single, uncoupled resonator.

Given our single-resonator cluster, we next obtained $\omega_a, \omega_b, \vec{Z}(\omega_a)$ and $\vec{Z}(\omega_b)$, needed to compute $\boldsymbol{\mathcal{Z}}$. We chose ω_a and ω_b to be on each side of the resonance peak, corresponding to corrected phase values of $\phi_1(\omega_a) = -0.33 \pm 0.12$ rad and $\phi_1(\omega_b) = -2.78 \pm 0.12$ rad. We completed the PLL measurement when the amplitude SNR reached > 5000. The PLL time series of amplitude and frequency are shown as 2D boxplots for a phase lock of $\phi_1(\omega_a)$ in Figure 2d and for $\phi_1(\omega_b)$ in **Figure 5.2e**. The mean values of amplitude, $\overline{A_1}(\omega_a)$ and $\overline{A_1}(\omega_b)$, and frequency, $\overline{\Omega_1}(\omega_a)/2\pi$ and $\overline{\Omega_1}(\omega_b)/2\pi$, are plotted as diamond points in **Figure 5.2f** (upper), with the color of each point corresponding to the box-and-whisker plots (**Figure 5.2d,e**). Errors are calculated standard error. The corrected phase values, $\phi_1(\omega_a)$ and $\phi_1(\omega_b)$, and mean values of frequency, $\overline{\Omega_1}(\omega_a)/2\pi$ and $\overline{\Omega_1}(\omega_b)/2\pi$, are plotted as diamond points in **Figure 5.2f**

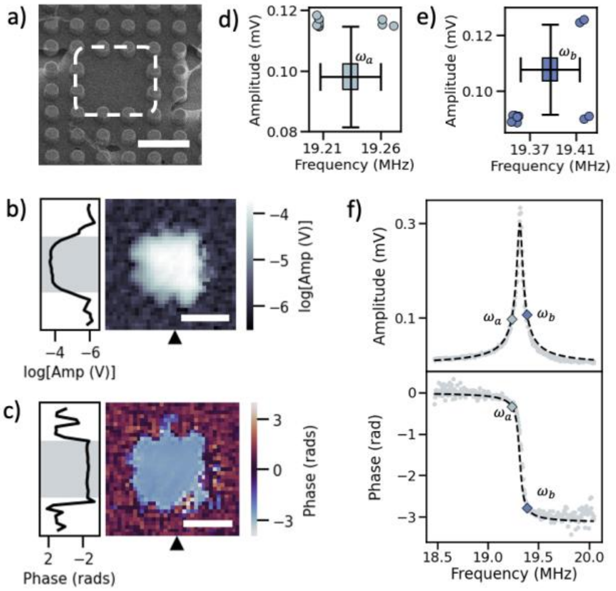

Figure 5.2: NetMAP analysis of first N = 1 cluster

a) SEM of driven uncoupled resonator, with pillar radii of 0.5 µm and pillar pitch 2 µm. Scale bar is 4 µm. **b)** Amplitude and **c)** phase spatial maps at a drive frequency of 18.81 MHz, scale bars are 5 µm. Phase spatial map shows uncorrected wrapped phase values. Black triangles on the bottom axis indicate the location of the vertical line scan on the left-side axis. 2D boxplot of PLL measurement distribution of frequency and amplitude for **d)** phase lock of $\phi_1(\omega_a) = 1.84$ rad and **e)** phase lock of $\phi_2(\omega_b) = -1.28$ rad. 2D boxplots shows median, upper, and lower quartile ranges with whiskers that extend to include 1.5 IQR. Plotted circles represent datapoints that were outliers in both frequency and amplitude. **f)** Amplitude and corrected phase spectra of driven resonator. The diamond points in the amplitude spectrum (upper) correspond to the mean PLL measurements of amplitude ($\overline{A_1}(\omega_a) = 0.09827 \pm 0.00002$ mV and $\overline{A_1}(\omega_b) = 0.10758 \pm 0.00002$ mV) and frequency ($\overline{\Omega_1}(\omega_a)/2\pi = 19.2337 \pm 0.00003$ MHz and $\overline{\Omega_1}(\omega_b)/2\pi = 19.3876 \pm 0.00004$ MHz), where the uncertainties are standard error. The diamond points in the phase spectrum (lower) correspond to the locked phase values, $\phi_1(\omega_a)$ and $\phi_1(\omega_b)$, and the mean frequency values, $\overline{\Omega_1}(\omega_a)/2\pi$ and $\overline{\Omega_1}(\omega_b)/2\pi$. The black dotted line represents $|Z_1(\omega)|$ and $\phi_1(\omega)$ generated from the normalized $\vec{p}$.

(lower). Using these measurements, we obtain $\omega_a = \overline{\Omega_1}(\omega_a)$, $\omega_b = \overline{\Omega_1}(\omega_b)$, $\vec{Z}(\omega_a) = \{\overline{A_1}(\omega_a)e^{i\phi_1(\omega_a)}\}$, and $\vec{Z}(\omega_b) = \{\overline{A_1}(\omega_b)e^{i\phi_1(\omega_b)}\}$.

To solve for the parameters vector, $\vec{p}$, we populate matrix $\boldsymbol{\mathcal{Z}}$ with coefficients of the experimentally measured $\omega_a, \omega_b, \vec{Z}(\omega_a)$ and $\vec{Z}(\omega_b)$. For a single-resonator cluster, the reduced system of equations, $\boldsymbol{\mathcal{Z}}\vec{p} = \vec{0}$, is

$$\begin{pmatrix} -\omega_a^2 Re[Z_1(\omega_a)] & -\omega_a Im[Z_1(\omega_a)] & Re[Z_1(\omega_a)] & -1 \\ -\omega_a^2 Im[Z_1(\omega_a)] & \omega_a Re[Z_1(\omega_a)] & Im[Z_1(\omega_a)] & 0 \\ -\omega_b^2 Re[Z_1(\omega_b)] & -\omega_b Im[Z_1(\omega_b)] & Re[Z_1(\omega_b)] & -1 \\ -\omega_b^2 Im[Z_1(\omega_b)] & \omega_b Re[Z_1(\omega_b)] & Im[Z_1(\omega_b)] & 0 \end{pmatrix} \begin{pmatrix} m \\ b \\ k \\ f \end{pmatrix} = \begin{pmatrix} 0 \\ 0 \\ 0 \\ 0 \end{pmatrix} \tag{5.5}$$

Given $N = 1$, $\vec{p}$ has four unknowns: $m, b, k,$ and f. We applied SVD to solve Eq(5.5) for $\vec{p}$, with the normalized values of $\vec{p}$ and associated errors listed in **Table 5.1.** We propagated the errors in $\vec{p}$ by sampling from Gaussian mean distributions of the two phases, mean drive frequencies, and mean amplitudes to generate hundreds of variations of $\boldsymbol{\mathcal{Z}}$. We then used SVD to solve for $\vec{p}$ corresponding to each $\boldsymbol{\mathcal{Z}}$, resulting in distributions of each output parameter, see Appendix B for error distribution discussion.

Mechanical Parameter	**NetMAP**	**Unity LS**
k [N/m]	1	1
m [10^{-17} kg]	6.790 ± 0.002	6.785
b [10^{-11}kg/s]	2.388 ± 0.643	2.283
F [10^{-7} au]	8.713 ± 0.286	8.107
Amplitude R^2	0.98	0.97
Phase R^2	0.97	0.99

Table 5.1: First set of normalized values of $\vec{p}$ from NetMAP and Unity LS for $N = 1$ Cluster

To assess how accurately the resulting $\vec{p}$ characterized the single resonator, we compared the normalized values to expected values. The spring constant of suspended multi-layer graphene[48] is $\sim 1 - 5$ N/m, so normalizing $\vec{p}$ by $k_1 = 1$ N/m provides order-of-magnitude estimates of all other parameters. We can estimate the mass of the resonator by using the area density of pristine graphene ($\rho = 0.75$ mg/m^2) and an approximated area based on the suspended region highlighted in **Figure 5.2a**, which gives a mass of 2.7×10^{-17} kg. While this mass estimate is lower than the value in **Table 5.1**, graphene contamination can increase the mass[99,55] by $\sim 10\,\times$, putting the predicted m within the expected range. In addition, we estimated the damping of the resonator by fitting the amplitude spectra to find the full width half max ($FWHM$) and the center frequency (ω_0). Using the fitted values, along with an estimation of $k = 1$ N/m, we estimate the damping to be $b = 1.92 \times 10^{-11}$ kg/s, which agrees with the value in **Table 5.1**. Additional details of these order-of-magnitude estimates can be found in Appendix C.

To evaluate the predictive power of the NetMAP results, we used $\vec{p}$ to calculate $|Z_1(\omega)|$ and $\phi_1(\omega)$ and compared the results to the experimental spectra. The $\vec{p}$-calculated $|Z_1(\omega)|$ and $\phi_1(\omega)$ are shown as black dashed lines overlayed on the spectra (**Figure 5.2f)** and the resulting R^2 values are listed in **Table 5.1**. We see that, despite building the analytical spectra from just two data points, the prediction agrees well with the data, accounting for a minimum of 97% of variation. Therefore, the normalized $\vec{p}$ can predict the cluster response exceptionally well across the tested frequency range.

As an additional validation, we compared the NetMAP $\vec{p}$ to that obtained from non-linear least-squares fitting with order of magnitude initial guesses (Unity LS), which is perhaps the most common means of characterizing resonant systems. The fit parameter estimates obtained using `Lmfit` in Python are listed in **Table 5.1**, see Appendix C for more Unity LS details. To compare the predicted $\vec{p}$ from each method, we employ a two-tailed t-test with the Unity LS parameters as reference. We find the damping b $(p = 0.87)$ agrees between both approaches but the mass $m\,(p = 0.004)$ and force $F\,(p = 0.03)$ do not agree. However, the mass from Unity LS still falls within the expected range and the force only differs by 7%. We also find that the $\vec{p}$ from Unity LS had similar predictive power when compared with the experimental spectra (see **Table 5.1**). Thus, we conclude that both methods are comparable for characterizing this system of a single resonator cluster.

To further demonstrate NetMAP, we characterized an additional cluster of size $N = 1$. We characterized the cluster by aligning the pump and probe over the resonator highlighted in **Figure 5.3a** and acquired amplitude and phase spectra. The resulting spectra had a single peak in the amplitude, gray data points in **Figure 5.3f** (upper), and a corresponding phase that crossed through $\pi/2$ at resonance, gray data points in **Figure 5.3f** (lower), consistent with a single, uncoupled resonator. To confirm the cluster size of $N = 1$, we took a SIM scan at $f = 17.64$ MHz, with the resulting amplitude spatial map shown in **Figure 5.3b** and phase in **Figure 5.3c**. In this scan we observed a single region of peak amplitude that had a constant phase, indicating that the cluster consisted of a single, uncoupled resonator. This region also corresponded in size and location to the driven resonator highlighted in **Figure 5.3a**.

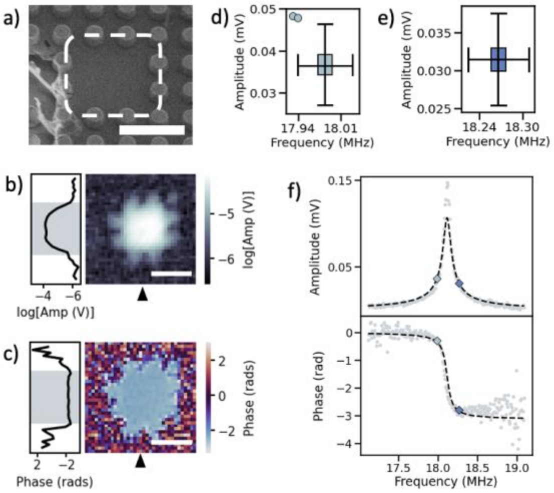

Figure 5.3: NetMAP analysis of second $N = 1$ cluster

a) SEM of driven uncoupled resonator, with pillar radii of 0.5 µm and pillar pitch 2 µm. Scale bar is 4 µm. **b)** Amplitude and **c)** phase spatial maps at a drive frequency of 17.64 MHz, scale bars are 5 µm. Phase spatial map shows uncorrected wrapped phase values. Black triangles on the bottom axis indicate the location of the vertical line scan on the left-side axis. 2D boxplot of PLL measurement distribution of frequency and amplitude for corrected phase lock values of **d)** $\phi_1(\omega_a) = -0.30$ rad and **e)** $\phi_2(\omega_b) = -2.79$ rad. 2D boxplots shows median, upper, and lower quartile ranges with whiskers that extend to include 1.5 IQR. Plotted circles represent datapoints that were outliers in both frequency and amplitude. **f)** Amplitude and corrected phase spectra of driven resonator. The diamond points in the amplitude spectrum (upper) correspond to the mean PLL measurements of amplitude ($\overline{A_1}(\omega_a) = 0.03684 \pm 0.00001$ mV and $\overline{A_1}(\omega_b) = 0.03146 \pm 0.00001$ mV) and frequency ($\overline{\Omega_1}(\omega_a) = 17.98422 \pm 0.00005$ MHz and $\overline{\Omega_1}(\omega_b) = 18.26637 \pm 0.00007$ MHz). The diamond points in the phase spectrum (lower) correspond to the locked phase values, $\phi_1(\omega_a)$ and $\phi_1(\omega_b)$, and the mean frequency values, $\overline{\Omega_1}(\omega_a)$ and $\overline{\Omega_1}(\omega_b)$. The black dotted line represents $|Z_1(\omega)|$ and $\phi_1(\omega)$ generated from the normalized $\vec{p}$.

We next measured $\omega_a, \omega_b, \vec{Z}(\omega_a)$ and $\vec{Z}(\omega_b)$, with target values of ω_a and ω_b to be on either side of the resonance peak, **Figure 5.3f** (upper). We used the corrected phase spectra, **Figure 5.3f** (lower), to map the chosen values of ω_a and ω_b to phase values for the PLL. The measured PLL time series of amplitude, $A(\omega_{a,b})$, and frequency, $\Omega(\omega_{a,b})/2\pi$, are shown as 2D boxplots in **Figure 5.3d,e**. Using the mean values of amplitude, $\overline{A}(\omega_a)$ and $\overline{A}(\omega_b)$, and frequency, $\overline{\Omega}(\omega_a)$ and $\overline{\Omega}(\omega_b)$, we obtain $\omega_a = \overline{\Omega}(\omega_a)$, $\omega_b = \overline{\Omega}(\omega_b)$, $\vec{Z}(\omega_a) = \{\overline{A}(\omega_a)e^{i\phi(\omega_a)}\}$, and $\vec{Z}(\omega_b) = \{\overline{A}(\omega_b)e^{i\phi(\omega_b)}\}$.

We then populated the matrix $\boldsymbol{\mathcal{Z}}$ with coefficients of the experimentally measured $\omega_a, \omega_b, \vec{Z}(\omega_a)$ and $\vec{Z}(\omega_b)$ and solved for the parameters vector $\vec{p}$. The resulting values are normalized to k are listed in **Table 5.1.** We found that each predicted parameter in $\vec{p}$ was consistent with the expected ranges discussed for the previous $N = 1$ cluster. Moreover, by comparing the analytical $\vec{Z}_1(\omega)$ and $\vec{Z}_2(\omega)$ generated from $\vec{p}$ to experimental spectra, we found that the model can account for 95% of the variation in the data, with R^2 values listed in **Table 5.2**. We also compared the results from NetMAP to those from Unity LS and found that m $(p = 0.35)$, b $(p = 0.91)$, and F $(p = 0.41)$ all agree. We therefore conclude that NetMAP is proficient in characterizing the local cluster.

Mechanical Parameter	**NetMAP**	**Unity LS**
k [N/m]	1	1
$m \times 10^{-17}$ [kg]	7.718 ± 0.010	7.709
$b \times 10^{-11}$[kg/s]	4.595 ± 2.814	4.293
$F \times 10^{-7}$ [N]	5.581 ± 0.527	6.017
Amplitude R^2	0.94	0.95
Phase R^2	0.97	0.97

Table 5.2: Results for additional $N = 1$ cluster from NetMAP and Unity LS

5.5 Results for resonator clusters of size $N = 2$

We next tested NetMAP on a system with more degrees of freedom, on a cluster size of $N = 2$. To begin, we positioned the pump and probe over the resonator region highlighted as R1 in **Figure 5.4a** and acquired amplitude and phase spectra. The resulting amplitude spectrum (**Figure 5.4f** (upper), grey data points) revealed two closely spaced peaks, each corresponding to a corrected phase of $\sim\pi/2$ (**Figure 5.4f** (lower), grey), indicative of the two hybridized modes of a pair of coupled resonators[83]. To test if the spectral features correspond to a resonator pair, we took a SIM scan across the region at a frequency below the first peak ($f_1 = 21.51\ MHz$). The resulting spatial maps (**Figure 5.4b,c**) show two distinct high-intensity amplitude regions with nearly constant phase, as highlighted in the line profiles (**Figure 5.4f)**. The first high-amplitude region was centered in a $6 \times 6\ \mu m^2$ region, which matched the size and location of the driven resonator R1 shown in **Figure 5.4a**. The second region matched the size and location of a $3 \times 3\ \mu m^2$ membrane highlighted as R2 in **Figure 5.4a**. The mean phases of R1 and R2 differed by 0.12 rad, or ~6.9°, (p~0.001), indicating they move in near unison, in accord with expectations for the symmetric mode of a coupled pair[64]. We search for the asymmetric mode with an additional SIM scan at a frequency above the second spectral peak ($f_2 = 22.55\ MHz$). In the resulting amplitude map and cross-section (**Figure 5.4d**), we see two regions with high amplitude situated at the same locations as R1 and R2 in **Figure 5.4a,b**. The phase map and profile (**Figure 5.4e**) reveal the phase in each region is relatively uniform, but the regions differ from each other by $\sim\pi$ rad, as expected for the asymmetric mode. From the spectra and SIM data, we conclude that the R1 and R2 resonators form a coupled pair.

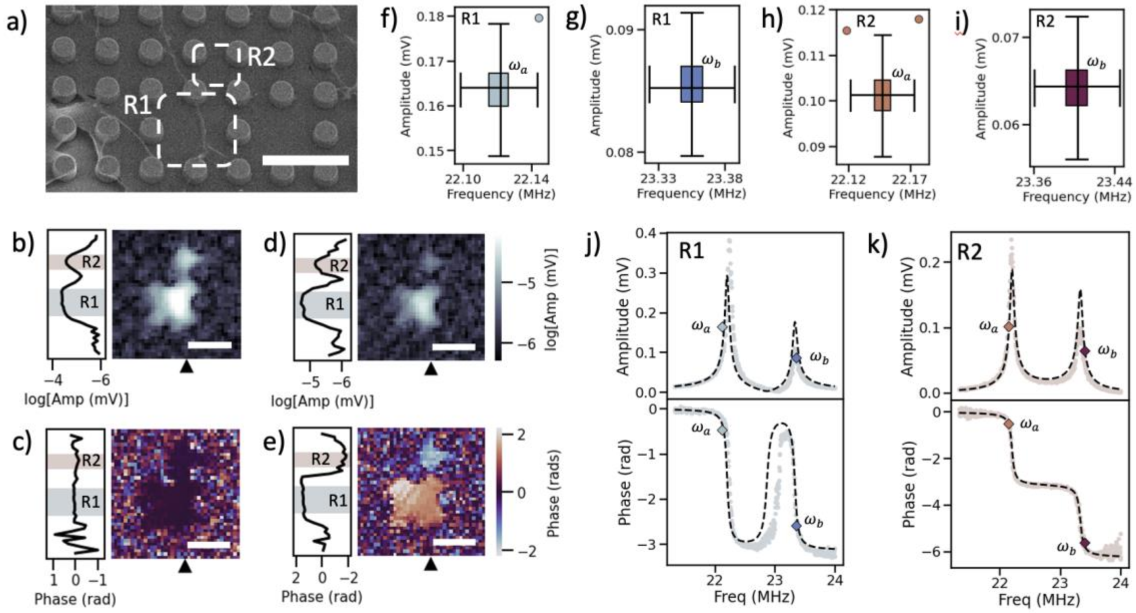

Figure 5.4: NetMAP analysis of first $N = 2$ cluster

a) SEM of driven resonator, R1, and neighboring coupled resonator, R2. Pillar radii are 0.75 µm and pillar pitch is 3 µm, scale bar is 6 µm. **b)** Amplitude and **c)** phase spatial maps taken at a drive frequency of $f_1 = 21.51$ MHz, scale bars are 5 µm. **d)** Amplitude and **e)** phase spatial maps taken at a drive frequency of $f_2 = 23.36$ MHz, scale bars are 5 µm. **c)** and **e)** phase spatial maps show uncorrected wrapped phase values. Black triangles on the bottom axes indicate the location of the vertical line scan on the left-side axis. 2D boxplots of PLL measurement distributions of frequency and amplitude for a phase lock of **f)** $\phi_1(\omega_a) = -0.47 \pm 0.06$ rad, **g)** $\phi_1(\omega_b) = -2.59 \pm 0.06$ rad, **h**) $\phi_2(\omega_a) = -0.51 \pm 0.2$ rad, and **i)** $\phi_2(\omega_b) - 5.61 \pm 0.2$. **j)** Amplitude (upper) and corrected phase (lower) of R1. Diamond points in the amplitude plot correspond to PLL measurements of amplitude ($\overline{A_1}(\omega_a) = 0.16368 \pm 0.00005$ mV and $\overline{A_1}(\omega_b) = 0.08560 \pm 0.00003$ mV) , and frequency ($\overline{\Omega_1}(\omega_a)/2\pi = 22.1208 \pm 0.00008$ MHz and $\overline{\Omega_1}(\omega_b)/2\pi = 23.3554 \pm 0.0001$ MHz). Diamond points in the phase plot correspond to the phase lock values, $\phi_1(\omega_a)$ and $\phi_1(\omega_b)$, and the mean frequency values, $\overline{\Omega_1}(\omega_a)/2\pi$ and $\overline{\Omega_1}(\omega_b)/2\pi$. The black dotted lines represent $|Z_1(\omega)|$ and $\phi_1(\omega)$ generated from the normalized $\vec{p}$. **k)** Amplitude (upper) and corrected phase (lower) of R2. Diamond points in the amplitude plot (upper) correspond to PLL measurements of amplitude ($\overline{A}_2(\omega_a) = 0.10146 \pm 0.00003$ mV and $\overline{A_2}(\omega_b) = 0.06420 \pm 0.00002$ mV) , and frequency ($\overline{\Omega_2}(\omega_a)/2\pi = 22.14721 \pm 0.00007$ MHz and $\overline{\Omega_2}(\omega_b)/2\pi = 23.4029 \pm 0.0001$ MHz). Diamond points in the phase plot (lower) correspond to the phase lock values, $\phi_2(\omega_a)$ and $\phi_2(\omega_b)$, and the mean frequency values, $\overline{\Omega_2}(\omega_a)/2\pi$ and $\overline{\Omega_2}(\omega_b)/2\pi$. The black dotted lines represent $|Z_2(\omega)|$ and $\phi_2(\omega)$ generated from the normalized $\vec{p}$.

To measure $\omega_a, \omega_b, \vec{Z}(\omega_a)$ and $\vec{Z}(\omega_b)$ for the coupled pair, we first aligned the probe over R2 and took spectra (**Figure 5.4i**). Using the R1 and R2 spectra, we chose a target value of ω_a below the symmetric mode peak and ω_b above the antisymmetric mode peak. We then positioned the probe over R1 and acquired two PLL time-series measurements at corrected phase values of $\phi_1(\omega_a)$ and $\phi_1(\omega_b)$. We completed each PLL measurement when the amplitude SNR reached ~ 3000. The R1 PLL data are shown as 2D boxplots for phase lock values of $\phi_1(\omega_a)$ in **Figure 5.4f** and $\phi_1(\omega_b)$ in **Figure 5.4g**. The mean values of amplitude, ($\overline{A_1}(\omega_a)$ and $\overline{A_1}(\omega_b)$), and frequency ($\overline{\Omega_1}(\omega_a)/2\pi$ and $\overline{\Omega_1}(\omega_b)/2\pi$), are plotted as diamond points in **Figure 5.4j** (upper), with the color of each point corresponding to the 2D boxplots (**Figure 5.4f,g**). The corrected phase values, $\phi_1(\omega_a)$ and $\phi_1(\omega_b)$, and mean values of frequency, $\overline{\Omega_1}(\omega_a)/2\pi$ and $\overline{\Omega_1}(\omega_b)/2\pi$, are plotted as diamond points in **Figure 5.4j** (lower). We repeated PLL measurements for the second resonator by placing the probe over R2, the pump fixed over R1, with corrected phase values of $\phi_2(\omega_a)$ and $\phi_2(\omega_b)$. The R2 PLL results are shown as 2D boxplots for phase lock values of $\phi_2(\omega_a)$ in **Figure 5.4h**, and $\phi_2(\omega_b)$ in **Figure 5.4i**.The mean values of amplitude, $\overline{A_2}(\omega_a)$ and $\overline{A_2}(\omega_b)$, and frequency, $\overline{\Omega_2}(\omega_a)/2\pi$ and $\overline{\Omega_2}(\omega_b)/2\pi$, are plotted as diamond points in **Figure 5.4k** (upper), with the color of each point corresponding to the 2D boxplots (**Figure 5.4h,i**). The corrected phase values, $\phi_2(\omega_a)$ and $\phi_2(\omega_a)$, and mean values of frequency, $\overline{\Omega_2}(\omega_a)/2\pi$ and $\overline{\Omega_2}(\omega_b,t)/2\pi$, are plotted as diamond points in **Figure 5.4k** (lower). We used these measurements to calculate $\omega_a = \left(\frac{1}{2}\right)(\overline{\Omega_1}(\omega_a) + \overline{\Omega_2}(\omega_a))$ and $\vec{Z}(\omega_a) = \{\overline{A_1}(\omega_a)e^{i\phi_1(\omega_a)}, \overline{A_2}(\omega_a)e^{i\phi_2(\omega_a)}\}$, and similarly to calculate ω_b and $\vec{Z}(\omega_b)$.

To solve for the parameters vector, $\vec{p}$, we populate $\boldsymbol{\mathcal{Z}}$ with coefficients of the experimentally measured values of ω_a, ω_b, $\vec{Z}(\omega_a)$, and $\vec{Z}(\omega_b)$. For a cluster size for $N = 2$, $\vec{p}$ has eight unknown components, $\vec{p} = \{m_1, m_2, b_1, b_2, k_1, k_2, c_1, F\}$ and $\boldsymbol{\mathcal{Z}}$ is an 8×8 matrix. We applied SVD to solve Eq (5.3) for $\vec{p}$, with values normalized by k_1 listed in **Table 5.3**. Errors are calculated as described above for the $N = 1$ cluster (see Appendix B for error distributions and discussion). With the k_1 normalization, the intrinsic spring k_2 is also within the expected range of $1 - 5$ N/m. If we assume R1 and R2 to have equal masses and intrinsic springs, we estimate $c_1 = 0.05$ N/m (see Appendix C for estimation discussion), which agrees with the value c_1 from **Table 5.3.** The damping constants b_1 and b_2 agree within error with the damping predicted above for the $N = 1$ case, which we expect considering that both clusters are on the same sample and tested under the same vacuum[100]. In addition, based on the areas of R1 and R2 and the area density of pristine graphene ($\rho = 0.75\ \mathrm{mg/m^2}$), we predict the mass of each resonator to be $m_1 = 2.7 \times 10^{-17}$ kg and $m_2 = 6.75 \times 10^{-18}$ kg. Accounting for contamination, both m_1 and m_2 estimates in **Table 5.3** are plausible. We note that while the area of R1 is larger than that of R2, the NetMAP prediction of $m_1 < m_2$ may account for the effective mass of each resonator or may be due to differences in local temperatures due to the optical probe position and PLL-related error.

Mechanical Parameter	**NetMAP**	**Unity L-S**
k_1 [N/m]	1 ± 0.074	1
k_2 [N/m]	1.784 ± 0.044	1.655
c_1 [N/m]	0.069 ± 0.002	0.057
$m_1 [10^{-17}$ kg]	5.263 ± 0.365	5.289
m_2 [10^{-17} kg]	8.975 ± 0.219	8.165
b_1 [10^{-11} kg/s]	1.424 ± 1.667	1.530
b_2 [10^{-11} kg/s]	5.405 ± 4.625	4.846
F [10^{-6} au]	1.501 ± 0.651	1.358
R1 Amplitude R^2	0.73	0.89
R1 Phase R^2	0.83	0.99
R2 Amplitude R^2	0.85	0.85
R2 Phase R^2	0.996	0.996

Table 5.3: Normalized values of $\vec{p}$ from NetMAP and Unity LS for $N = 2$ cluster

To evaluate the predictive power of $\vec{p}$, we compared the analytical $\vec{Z}_1(\omega)$ and $\vec{Z}_2(\omega)$ generated from $\vec{p}$ to experimental spectra using R^2. The analytical responses are shown as black dashed lines overlayed on the spectra in **Figure 5.4j,k** and the resulting R^2 values are listed in **Table 5.3**. Because the $\vec{p}$-calculated responses in the model account for at least 70% of variability in all the experimental spectra (all R^2 values are greater that 0.7), we conclude that the $\vec{p}$-calculated responses can accurately predict the experimental spectral response of the cluster over the tested range.

To further evaluate the utility of our approach, we benchmark the NetMAP predicted $\vec{p}$ against results from Unity LS, see **Table 5.3**. Although our approach does not require *a priori* information and only uses two vector data points, as opposed to LS which uses thousands of spectral points and requires initial guesses, the two approaches agree but only with precise order-unity *a priori* parameter estimates for LS. Using order-unity guesses informed by the NetMAP $\vec{p}$ (*e.g.* $m_1 = m_2 = 10^{-17}$ kg) and omitting LS error (see SI), the two approaches agree on the vales $m_1 (p = 0.94)$, b_1 $(p = 0.95)$, b_2 $(p = 0.90)$, and F $(p = 0.83)$. Although the values disagree for k_2 $(p = 0.003)$, c_1 $(p = 0, t_0 = 7)$, and m_2 $(p = 0.0002)$, each value predicted by LS was still within the expected range discussed above and only differed from the NetMAP $\vec{p}$ by at most $8 - 21\%$. We also found that LS resulted in some higher R^2 values, although this is to be expected considering NetMAP does not utilize the full spectra.

The agreement between NetMAP and unity LS is sensitive to the LS input guess solutions. For example, by increasing the input guesses for mass only (*e.g.* $m_1 = m_2 = 10^{-16}$ kg), LS yields a predicted k_2 about $1000 \times$ lower than the expected $1 - 5$ N/m and a predicted m_2 about $10 \times$ less than expected for pristine graphene (see Appendix C for LS results), as well as poor fits with some $R^2 < 0$. This result highlights the susceptibility of LS to correlation errors because while individually k_2 and m_2 are far from the expected values, the ratio of $\sqrt{\frac{k_2}{m_2}}$ gives an expected resonance frequency of ~ 16 MHz, within 7 MHz of the observed amplitude peaks. These correlated values, which are prevalent in our model, result in many possible solutions for least squares fitting, making this method reliant on the input guess solutions to find the residual minimum that is closest to the actual values. Combining NetMAP with LS fitting by inputting $\vec{p}$ as guess solutions may be an effective strategy to fit parameter values as close to the actual values as possible. Given that our approach is not sensitive to input guesses, NetMAP provides a robust means to obtain physically accurate network parameters without any *a priori* knowledge of those parameters.

We characterized an additional $N = 2$ cluster by again aligning the pump and probe over the region highlighted as R1 in **Figure 5.5a** and taking amplitude and phase spectra. The amplitude spectrum, gray data points in **Figure 5.5j**, revealed two peaks that corresponded to phase changes that pass through $\sim\pi/2$ on resonance. To test whether these peaks correspond to the hybridized modes of a coupled pair, we took an SIM scan at $f = 15.45$ MHz, **Figure 5.5b,c**, and another at $f = 16.21$ MHz, **Figure 5.5d,e**. In the first scan, we saw two distinct high intensity area regions with nearly constant phase across each individual resonator. The first 6 × 6 μm region matched the size and location of the driven resonator, R1 highlighted in **Figure 5.5a**. The neighboring 6 × 6 μm region matched the size and location of the resonator to the right of R1, labelled as R2 in **Figure 5.5a**. Although we noticed smaller neighboring regions of amplitude maxima and constant phase, because we only observe two peaks in the amplitude spectra, we approximate other membrane motion to be due to weak coupling. We therefore approximate this system to be an $N = 2$ cluster.

To measure $\omega_a, \omega_b, \vec{Z}(\omega_a)$ and $\vec{Z}(\omega_b)$, we chose a target value of ω_a below the symmetric mode peak and ω_b above the antisymmetric mode peak, shown for R1 in **Figure 5.5j** (upper) and for R2 in **Figure 5.5k** (upper). We used the corrected R1 phase spectra, **Figure 5.5j** (lower), to map the chosen ω_a and ω_b to phase values of $\phi_1(\omega_a)$ and $\phi_1(\omega_b)$. Because the R2 phase spectrum off resonance was too noisy to accurately fit to a linear model, we corrected the R2 phase values with the R1 fit values of ϕ_0 and τ. With the probe positioned over R1, we acquired PLL time-series measurements for the two phase values, shown as 2D boxplots in **Figure 5.5f,g**. We repeated these PLL measurements for the second resonator by using the corrected R2 phase spectra, **Figure 5.5k** (lower), to map ω_a and ω_b to phase values of $\phi_2(\omega_a)$ and $\phi_2(\omega_b)$. We positioned the probe over R2, fixed the pump over R1, and acquired PLL time-series measurements for each phase, shown as 2D boxplots **Figure 5.5h,i**. We then used the PLL measurements to calculate $\omega_a = \left(\frac{1}{2}\right)(\overline{\Omega_1}(\omega_a) + \overline{\Omega_2}(\omega_a)), \vec{Z}(\omega_a) = \{\overline{A_1}(\omega_a)e^{i\phi_1(\omega_a)}, \overline{A_2}(\omega_a)e^{i\phi_2(\omega_a)}\}$, $\omega_b = \left(\frac{1}{2}\right)(\overline{\Omega_1}(\omega_b) + \overline{\Omega_2}(\omega_b))$, and $\vec{Z}(\omega_b) = \{\overline{A_1}(\omega_b)e^{i\phi_1(\omega_b)}, \overline{A_2}(\omega_b)e^{i\phi_2(\omega_b)}\}$.

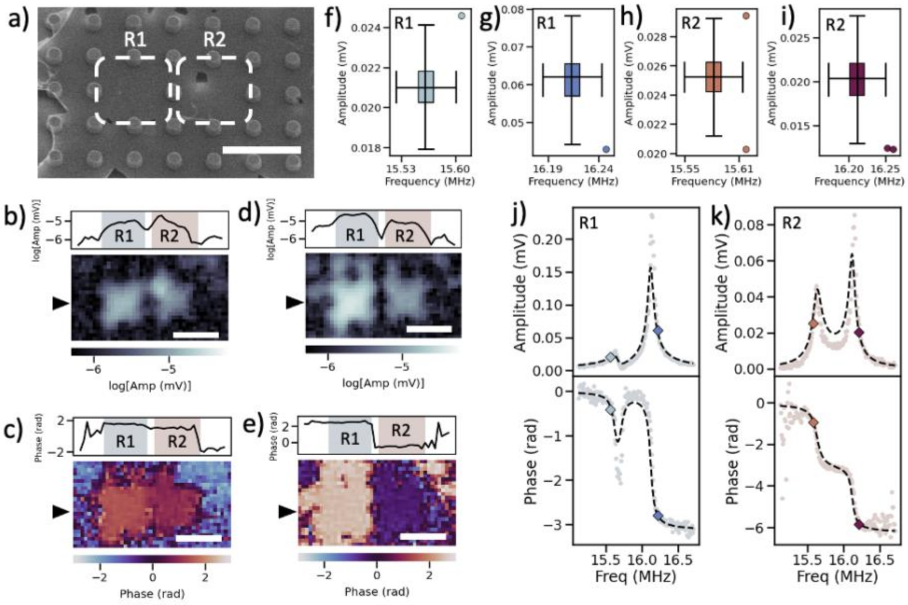

Figure 5.5: NetMAP analysis of second $N = 2$ cluster

a) SEM of driven resonator, R1, and neighboring coupled resonator, R2. Pillar radii are 0.5 µm and pillar pitch is 3 µm, scale bar is 6 µm. **b)** Amplitude and **c)** phase spatial maps taken at a drive frequency of $f_1 = 15.45$ MHz, scale bars are 5 µm. **d)** Amplitude and **e)** phase spatial maps taken at a drive frequency of $f_2 = 16.21$ MHz, scale bars are 5 µm. **c)** and **e)** phase spatial maps show uncorrected wrapped phase values. Black triangles on the left-side axes indicate the location of the vertical line scan on the left-side axis. 2D boxplots of PLL measurement distributions of frequency and amplitude for a phase lock of **f)** $\phi_1(\omega_a) = -0.41 \pm 0.15$ rad, **g)** $\phi_1(\omega_b) = -2.79 \pm 0.15$ rad, **h**) $\phi_2(\omega_a) = -0.93 \pm 0.81$ rad, and **i)** $\phi_2(\omega_b) = -5.85 \pm 0.81$. **j)** Amplitude (upper) and corrected phase (lower) of R1. Diamond points in the amplitude plot correspond to PLL measurements of amplitude ($\overline{A_1}(\omega_a) = 0.021010 \pm 0.000007$ mV and $\overline{A_1}(\omega_b) = 0.060903 \pm 0.000020$ mV) , and frequency ($\overline{\Omega_1}(\omega_a) = 15.56192 \pm 0.00009$ MHz and $\overline{\Omega_1}(\omega_b) = 16.21389 \pm 0.0004$ MHz). Diamond points in the phase plot correspond to the phase lock values, $\phi_1(\omega_a)$ and $\phi_1(\omega_b)$, and the mean frequency values, $\overline{\Omega_1}(\omega_a)$ and $\overline{\Omega_1}(\omega_b)$. The black dotted lines represent $|Z_1(\omega)|$ and $\phi_1(\omega)$ generated from the normalized $\vec{p}$. **k)** Amplitude (upper) and corrected phase (lower) of R2. Diamond points in the amplitude plot (upper) correspond to PLL measurements of amplitude ($\overline{A_2}(\omega_a) = 0.025206 \pm 0.000008$ mV and $\overline{A_2}(\omega_b) = 0.020166 \pm 0.000007$ mV) , and frequency ($\overline{\Omega_2}(\omega_a) = 15.58158 \pm 0.00007$ MHz and $\overline{\Omega_2}(\omega_b) = 16.21161 \pm 0.00004$ MHz). Diamond points in the phase plot (lower) correspond to the phase lock values, $\phi_2(\omega_a)$ and $\phi_2(\omega_b)$, and the mean frequency values, $\overline{\Omega_2}(\omega_a)$ and $\overline{\Omega_2}(\omega_b)$. The black dotted lines represent $|Z_2(\omega)|$ and $\phi_2(\omega)$ generated from the normalized $\vec{p}$.

Using the calculated values of ω_a, ω_b, $\vec{Z}(\omega_a)$, and $\vec{Z}(\omega_b)$, we populated the matrix $\boldsymbol{\mathcal{Z}}$ and solved for the parameters vector $\vec{p}$. We applied SVD to solve $\boldsymbol{\mathcal{Z}}\vec{p} = \vec{0}$ for the eight unknown components of $\vec{p}$, which are normalized by k_1 and listed in Table **5.4**. We find that the values of k_2, c_1, m_1, m_2, b_1, and b_2 are all within the expected ranges discussed in the main text. Moreover, we observe that this set of parameters has predictive power over the experimentally measured spectral range, with R1 and R2 amplitude R^2 values ≥ 0.77 and the phase R^2 values ≥ 0.92 (See **Table 5.4**).

Mechanical Parameter	NetMAP	Unity LS
k_1 [N/m]	1 ± 0.163	1
k_2 [N/m]	0.923 ± 0.299	0.664
c_1 [N/m]	0.021 ± 0.006	0.021
$m_1 \times 10^{-17}$[kg]	10.035 ± 1.544	10.039
$m_2 \times 10^{-17}$[kg]	9.695 ± 3.134	7.032
$b_1 \times 10^{-11}$ [kg/s]	4.336 ± 4.00	4.476
$b_2 \times 10^{-11}$ [kg/s]	7.396 ± 5.546	4.311
$F \times 10^{-6}$ [N]	0.883 ± 0.355	0.910
R1 Amplitude R^2	0.88	0.90
R1 Phase R^2	0.97	0.98
R2 Amplitude R^2	0.77	0.35
R2 Phase R^2	0.92	0.93

Table 5.4: Normalized values of $\vec{p}$ from NetMAP and Unity LS for second $N = 2$ cluster

We benchmarked NetMAP results against those form least squares fitting and found that all values agree within error for k_2 ($p = 0.38$), c_1($p = 0.99$), m_1 ($p = 0.998$), m_2 ($p = 0.40$), b_1 ($p = 0.97$), b_2 ($p = 0.58$), and F ($p = 0.94$). However, the predicted power of the Unity LS is poor for the R2 amplitude, as the model only accounts for 35% of variation in the experimental data (See **Table 5.4**). However, the method that had the best predictive power over the tested experimental range, was when we used LS to fit the vector weights corresponding to the two smallest singular values, with R1 and R2 amplitude and phase R^2 values all ≥ 0.92.

5.6 Discussion

Thus far, we have reported solutions to $\boldsymbol{\mathcal{Z}}\vec{p} = \vec{0}$ that belong to a one-dimensional (1D) null-space. However, the null-space can be higher dimensional, and considering the full null-space basis may result in a $\vec{p}$ that is more physically accurate. In practice, we characterize the null-space dimension by the number of singular values λ such that $\lambda \ll 1$. For the $N = 1$ clusters (**Figure 5.2** and **Figure 5.3**), we had only one candidate singular value ($\lambda \sim 10^{-9}$), so the null-space was 1D. However, the $N = 2$ clusters (**Figure 5.4** and **Figure 5.5**) has three potential singular values (for the first $N = 2$ cluster – $\lambda_1 \sim 10^{-4}$, $\lambda_2 \sim 10^{-6}$, and $\lambda_3 \sim 10^{-8}$), so the null-space could be up to 3D, leading to multiple effective parameter combinations that could reconstruct the measured complex amplitudes, *e.g.* $\vec{p} = \alpha_1\vec{p}_1 + \alpha_2\vec{p}_2 + \alpha_3\vec{p}_3$. In the case of a higher-dimension null-space, we can obtain $\vec{p}$ by specifying additional constraints, such as the estimated masses of each resonator. Alternatively, we could avoid providing *a priori* information about the network parameters by LS fitting to full spectra to solve for the weights of each vector (*i.e.* α_i) for a facile means to account for higher-dimensional null-spaces without requiring additional knowledge of network parameters, see Appendix C for α_i LS applied to first $N = 2$ cluster.

The combination of SIM and algebraic solving in the NetMAP approach provides a means to spatially map and quantify the mechanical elements of a resonator network, and as such is a powerful and vital tool for programming resonator networks for future applications.

The spatial information provided by SIM is essential for NetMAP because it provides the size and resonator configuration needed to model the cluster. Since weak coupling is difficult or impossible to detect using the spectra alone[83]—*e.g.* when spectral peaks cannot be resolved because of dissipative broadening—spectroscopy cannot reliably be used to determine model size. Considering this shortfall, SIM is a uniquely useful tool because it detects all resonators with motion in the cluster, regardless of the coupling strength, and therefore quantifies the model size. However, to uniquely define $\boldsymbol{\mathcal{Z}}$ and thereby solve $\vec{p}$, NetMAP requires knowledge of both the cluster size and the exact lateral positions of each resonator in the cluster, including the driven resonator. Spectroscopy alone does not provide spatially resolved information as it cannot be used to distinguish which resonators out of many participate in the hybridized modes. An additional valuable feature of SIM is that it provides the spatial coordinates of all resonators and the force, and thus enables the algebraic characterization method. Moreover, although we have constructed $\boldsymbol{\mathcal{Z}}$ with PLL measurements, it is possible to build $\boldsymbol{\mathcal{Z}}$ directly from SIM amplitude and phase images, where $Z_i(\omega)$ is calculated from spatial averaging over a given resonator. This fully SIM-based route eliminates the need for PLL measurements and isn't susceptible to PLL drift noise but reduces the SNR for the same measurement time.

To program a cluster or entire network of nanomechanical resonators (see **Figure 5.1a**), it is imperative to know the properties of each resonator node (*i.e.* k_n, m_n, b_n, c_n) in its most recent state. As a concrete example, to program a network as a phononic crystal[26,25] the node resonance frequencies ($\omega_n \equiv \sqrt{k_n/m_n}$) and coupling ($c_n$) must be finely tuned. But to adjust ω_n to a desire value, the current values of k_n and m_n for each resonator must be known before they can be appropriately tuned. This knowledge is especially important when the tuning method is irreversible, such as the additive or subtractive tuning of resonator mass[101]. Although ω_n can be determined with least squares fitting, correlations in the model make it difficult to decouple the individual values of k_n and m_n, and, as discussed above, fitting does not provide spatial information, further obfuscating the node properties. The phononic crystal must also have precisely tuned coupling between resonators. Typically, the coupling strength of simple $N = 2$ systems is inferred from avoided-crossing signatures in gate-tuned spectrographs[19,63]. However, for larger systems (*i.e.* $N \geq 3$) this approach does not directly provide the coupling constants c_n and cannot indicate the corresponding spatial location of the spring analogs. In contrast, NetMAP directly quantifies normalized physical parameters of each node, including k_n, m_n, and c_n, and characterizes the spatial ordering. The normalized values of $\vec{p}$ can be unnormalized by taking a separate measurement of a single parameter, such as measuring k_n with AFM[48]. Therefore, by spatially resolving the network parameters, NetMAP will enable the programming of our network platform for on-demand tailored phononic crystals, engineered defects[27] , or control of wave propagation[25].

While we have limited our use of NetMAP to cluster sizes of $N = 1$ and $N = 2$, it can also be used to efficiently map larger clusters and entire networks. For a given cluster of size N, the edge coupling spring constants vanish (c_{n-1}~0 and c_{n+N+1}~0), leaving $4N$ unknown parameters in $\vec{p}$. Regardless of N, NetMAP requires a minimum of two response measurements (at ω_a and ω_b) per resonator to assemble $\boldsymbol{\mathcal{Z}}$, which will be a $4N \times 4N$ matrix. Given the dimensions of $\boldsymbol{\mathcal{Z}}$**,** the number of SVD-specific operations[102] needed to obtain $\vec{p}$ will scale efficiently with polynomial time, $O(N^3)$. After using NetMAP to characterize each cluster, we can assemble a map of the entire network composed of neighboring clusters separated by coupling springs of $c_n = 0$. With a full picture of the network, we can modify the edge c_n values to form larger clusters or link clusters into a single, fully interconnected network.

We used NetMAP to characterize one-dimensional suspended graphene resonator networks, but the technique can be applied to higher-dimensional systems and a variety of resonator network analogs. this technique readily scales to networks in two and three dimensions and with more complex coupling beyond nearest-neighbor that we assume in our model. In these cases, depending on the exact geometry of the cluster, it is likely that that more than two complex response vectors must be measured to solve for the unknown parameters. Provided it is possible to obtain spatially resolved amplitude and phase responses for a cluster, as we do here with SIM, our algebraic characterization method can be applied to a range of steady-state linear resonator platforms, such as alternative geometries of MEMS/NEMS arrays[28,79] , optical lattices[93], LRC-based electronic circuits, and biological networks. A modified version of NetMAP will also be relevant to quantum analogs, such as chains of trapped ions[8], 2D superconducting qubit arrays[91] and could be useful for programming the initial state for quantum computational tasks.

5.7 Conclusion

In conclusion, we use NetMAP to spatially map and quantify all the physical parameters in local suspended graphene resonator clusters of sizes $N = 1$ and $N = 2$. By combining spatially resolved measurements of the resonator building blocks and an algebraic solution of the network equations of motion, NetMAP provides a novel means of characterization that overcomes the weaknesses of current spectroscopic techniques, thereby enabling a programmable resonator network. Programmable NEMS networks will enable applications such as modeling natural systems, realizing mechanical computing schemes[32,31,35,103], integrating into quantum information circuits[52], and exploring new physics such as phononic metamaterials and exotic states[28,18,25].

6 Conclusion

6.1 Remarks regarding future directions

In this work, we show the viability of suspended graphene to enable rich coupling dynamics and demonstrate a compatible analysis tool that will enable precise tuning of each network parameter. Future work towards realizing programmable nanomechanical networks will be to expand the size of the networks and to demonstrate scalable tuning. Our graphene platform provides access to a tuning method that will be essential to achieving these next steps. With phototuning, we can precisely align the resonance frequencies of a local network cluster to host coupling between a large cluster of resonators. We can then use phototuning to increase the tension of the suspended membrane connecting two adjacent resonators to adjust the coupling strength between nodes. This scalable and persistent tuning method would open the door to reconfigurable phononic circuits with components that can be tuned *in situ*, like the transistor.

In addition to providing a network platform, our novel pillar structure, discussed in Chapter IV, can also be used as a method to suspend large areas of graphene. Graphene suspended over a pillar array can be released to form a large resonator or multiple resonators with specific configurations. While we have preliminarily experimented with using a focused ion beam (FIB) to cut and release the graphene from the pillars, further work is required to explore the dimensions that can be obtained with this method.

Our NetMAP network analysis method, presented in Chapter V, fills a key gap of spatially mapping the active nodes of a NEMS network and the corresponding physical parameters. The next question to be answered with this work is that of accuracy, which is already underway through a design of experiment (DOE) approach applied to a simulated mass and spring model. Although we apply NetMAP only to analyze our graphene NEMS network, this method can be applied to analyze any network, provided there is a means of spatially measuring the amplitude and phase of each node. Further work may expand the scope of NetMAP with characterization of additional network platforms, including networks of electrical components or chains of trapped ions.

6.2 Resolution

This work lays the foundation for achieving programmable nanomechanical 2D networks. We began Chapter II by discussing a linear mass and spring model commonly used to capture the dynamics of NEMS resonators, which is a necessary component of characterizing our suspended graphene network platform. In Chapter III, we outlined the experimental fabrication and measurement techniques used in this work to create our suspended graphene platform and measure the network oscillations. We then presented our novel device platform in Chapter IV, that enables rich coupling dynamics between distinct suspended graphene resonators. Finally, in Chapter V, we examined a network characterization method applied to spatially map the mechanical parameters of suspended graphene networks.

Overall, this work paves the way for graphene resonators to be a competitive contender in the pursuit of NEMS resonator networks. Our pillar platform, discussed in Chapter IV, is the first to our knowledge to enable coupling between 2D suspended graphene resonators, filling a key gap of achieving a persistently coupled network that is scalable in size in two dimensions. Together with our NetMAP characterization method, we offer the foundation to build and characterize the previously unattainable 2D network of graphene resonators. This foundation directly enables near-term access to exciting applications, such as mechanical computing, reconfigurable waveguides, and tunable metamaterial, and provides model platform that can be used to simulate many-body systems impacting a range of fields including quantum mechanics, astronomy, biology, sociology, economics.

APPENDIX A

RESONANCE FREQUENCY DEPENDENCE ON DRUMHEAD SIZE

In **Figure A.1**, we show a box and whisker plot of the resonance frequency of 107 individual circular graphene resonators. We observe a decreasing trend in the resonance frequency from drumheads with diameters of 4.4 μm to 9.4 μm, whereas drumheads with diameters from 9.4 μm to 16.6 μm have resonance frequencies that are indistinguishable (based on Tukey-Kramer HSD comparison of means). This data set is part of a larger study of dissipation dilution in graphene NEMS resonators. Through this large-scale study, we develop a technique to increase the quality factor of graphene drumheads to greater than $Q > 10^5$.

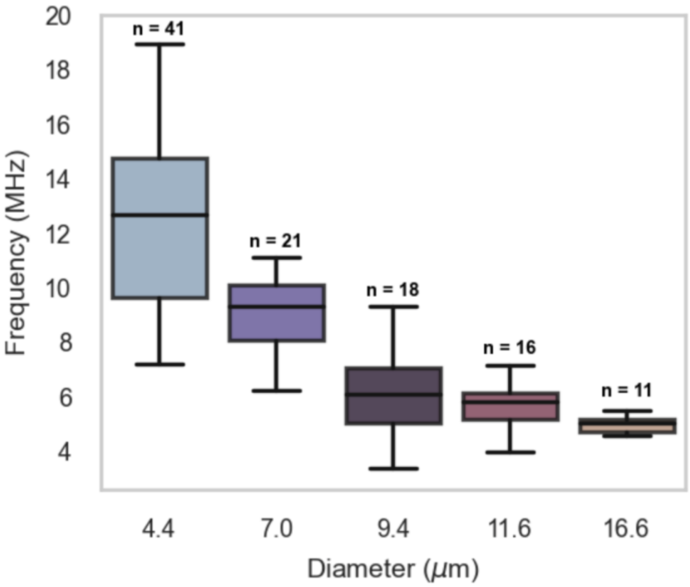

Figure A.1: Resonance frequencies of drumhead resonators

Box and whisker plot of resonance frequency of drumhead resonators of diameters ranging from 4.4 μm to 16.6 μm. Each boxplot is labeled with the number of resonators in each distribution as n. Data reproduced from co-authored manuscript in progress.

APPENDIX B
ERROR DISTRIBUTIONS OF NetMAP PARAMETERS

To assess the precision of NetMAP, we solve for $\vec{p}$ with a distribution of $\boldsymbol{\mathcal{Z}}$ matrices and calculate the standard deviation of each output parameter. For the single resonator cluster, we randomly sampled ω_i and $Z_1(\omega_i)$, for $(i = a, b)$, from normal distributions with a standard deviation equal to the standard error of the PLL time series $\Omega_1(\omega_i, t)$ and $|Z_1(\omega_i, t)|$. We randomly sampled $\phi_1(\omega_i)$ from a normal distribution with the standard deviation equal to the uncertainty calculated in equation Eq(5.4 **)**. We then used these randomly sampled values to populate $\boldsymbol{\mathcal{Z}}$ and applied SVD to solve for $\vec{p}$. We repeated this procedure $n = 1000$ times to obtain distributions of each output parameter (m, b, F). For the $N = 1$ cluster, the SVD solver always normalized to the spring constant k, so this method did not provide an error for the spring constant. We then removed all solutions that were unphysical or deficient, i.e solutions in which the output parameters did not have a homogenous sign or the R^2 values were negative, and were left with distributions of $n = 859$ for each output parameters, with the results shown in **Figure B.1a-c**. We quote the standard deviation of each distribution as the error on the parameter value in **Table 5.1** of the main text. To assess the predictive power of each output parameter set, we used each output $\vec{p}$ to calculate $\overrightarrow{Z_n}(\omega)$ and compared the result to the experimental spectra of amplitude and phase to calculate distributions of the R^2 values, shown in **Figure B.1d**.

We repeated this procedure to calculate the errors for the output parameters of the $N = 2$ cluster. We produced a normal distribution to randomly sample ω_i with a standard deviation equal to standard errors of the R1 and R2 frequency time series, $\Omega_1(\omega_i, t)$ and $\Omega_2(\omega_i, t)$, added in quadrature. We randomly sampled the amplitudes and phases for each resonator, $Z_1(\omega_i)$ and $Z_2(\omega_i)$, using the same procedure described for the $N = 1$ cluster above. We then use these randomly sampled values to populate $\boldsymbol{\mathcal{Z}}$, used SVD to solve for $\vec{p}$, and repeated the procedure $n = 5000$ times. We then removed all non-physical solutions, resulting in distributions of $n = 253$ shown for each parameter $(m_1, m_2, b_1, b_2, k_1, k_2, k_{12}, F)$ in **Figure B.1e-i**. We again assessed the predictive power of each output $\vec{p}$ by comparing calculated $\overrightarrow{Z_n}(\omega)$ and to the experimental spectra of the R1 and R2 amplitude and phase to obtain distributions of R^2 values, shown in **Figure B.1j**.

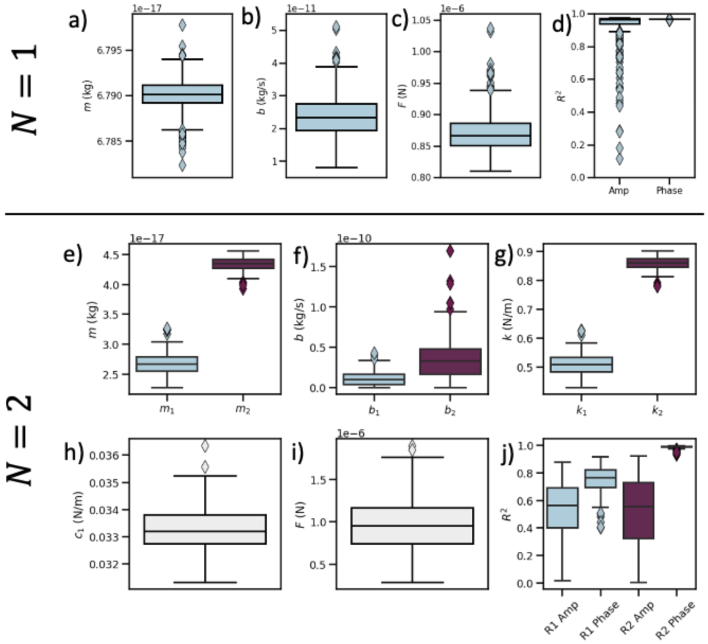

Figure B.1: NetMAP parameter errors for $N = 1$ cluster

Error distributions as box and whisker plots showing median, upper, and lower quartile ranges with whiskers that extend to include 1.5 IQR. Quoted errors are standard deviations. Error distributions for $N = 1$ cluster parameters shown as light blue boxes with **a)** $m = (6.790 \pm 0.001) \times 10^{-17}$ kg , **b)** $b_1 = (2.4 \pm 0.6) \times 10^{-11}$ kg/s, **c)** $F = (8.7 \pm 0.3) \times 10^{-6}$ N. **d)** $N = 1$ cluster distributions of R^2 values for amplitude ($R^2 = 0.94 \pm 0.08$) and phase ($R^2 = 0.968 \pm 0.001$). Error distributions for $N = 2$ cluster with R1 distributions shown as light blue boxes and R2 distributions shown as maroon boxes for **e)** $m_1 = (5.2 \pm 0.4) \times 10^{-17}$ kg and $m_2 = (8.5 \pm 0.2) \times 10^{-17}$ kg, **f)** $b_1 = (2.4 \pm 1.9) \times 10^{-11}$ kg/s and $b_2 = (6.7 \pm 4.5) \times 10^{-11}$ kg/s, **g)** $k_1 = 1.00 \pm 0.08$ N/m and $k_2 = 1.69 \pm 0.05$ N/m. Error distributions for $N = 2$ cluster of **h)** $\mathrm{c}_1 = 0.065 \pm 0.002$ N/m and **i)** $F = (1.9 \pm 0.7) \times 10^{-6}$ N. **j)** $N = 2$ cluster distributions of R^2 values with R1 distributions shown as light blue boxes for amplitude ($R^2 = 0.51 \pm 0.20$) and phase ($R^2 = 0.75 \pm 0.08$). R2 distributions are shown as maroon boxes for amplitude ($R^2 = 0.51 \pm 0.25$) and phase ($R^2 = 0.988 \pm 0.008$).

APPENDIX C

SUPPLEMENTARY INFORMATION REGARDING NetMAP EVALUATION

To evaluate the stability of the PLL measurements over time, we replot the data that is displayed as 2D boxplots in **Figure 5.2d,e** as a function of data point number. The PLL measurements of amplitude (upper) and frequency (lower) are plotted for phase lock values of $\phi_1(\omega_a)$, **Figure C.1a**, and $\phi_1(\omega_b)$, **Figure C.1b.** We observe that the frequency does not drift significantly in either PLL measurement. We do observe a slight increase in amplitude in the $\phi_1(\omega_b)$ PLL measurement, **Figure C.1b** (upper), which could be due to a shift up in the resonance frequency due to heating.

In the main text, we evaluate the accuracy of the NETMAP calculated $\vec{p}$ by comparing each calculated value to expected values. To estimate the expected value of the damping, b, we fit the amplitude spectra to a built-in Lmfit model, DampedOscillatorModel, which has three fit parameters: A, ω_0 , and σ. Because there are low correlations between each parameter, the resulting values have low error. From the model equation and fit parameters σ and ω_0, we estimate the damping based on

$$2\sigma\omega_0 = \frac{b}{m}$$

We divide both sides by $\omega_0^2 = \frac{k}{m}$, where ω_0 is the fitted center frequency.

$$b = \frac{2k\sigma}{\omega_0}$$

With fitted values of $\omega_0 = 2\pi \times (19.32 \text{ MHz})$ and $\sigma = 1.16 \times 10^{-3}$, along with the approximated value of $k = 1$ N/m, we estimate the damping to be $b = 1.92 \times 10^{-11}$ kg/s.

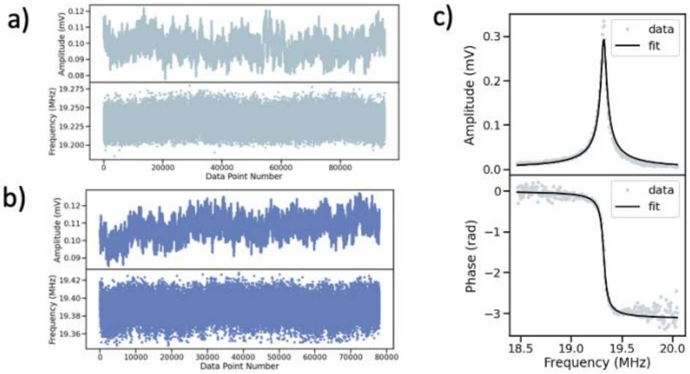

Figure C.1: Additional figures for $N = 1$ cluster

PLL measurements of amplitude and frequency plotted by data point number for corrected phase lock values of **a)** $\phi_1(\omega_a) = -0.33$ rad shown in light blue and **b)** $\phi_1(\omega_b) = -2.78$ rad shown in dark blue. **c)** least square fit result shown as solid black line over spectra data of amplitude (upper) and phase (lower) shown as gray data points.

To further validate NETMAP, we compare the NETMAP output parameters to those from least-squares fitting with unity order of magnitude guesses, Unity LS. The fit result of Unity LS, listed in **Table 5.1** in the main text, is shown in **Figure C.1c** as a solid black line overlayed on the experimental spectra. To compare each output parameter from NetMAP and LS, we perform a two tailed t-test, using the LS values as reference because the LS errors for each parameter value were large (up to 3000%). We suspect these large errors are due to the high correlations of multiple parameter pairs in our model. We also compared values by using a percent difference, which we calculate by taking the absolute value of the difference between the two values to be compared and dividing by the smaller of the two values for an upper bound estimate.

To observe the stability of the PLL measurements over time, we replot the data that is displayed as 2D boxplots in **Figure 5.4f-i**, as a function of data point number. The R1 PLL measurements are shown for phase lock values of $\phi_1(\omega_a)$, **Figure C.2a**, and $\phi_1(\omega_b)$, **Figure C.2b**. The R2 PLL measurements are shown for phase lock values of $\phi_2(\omega_a)$, **Figure C.2c**, and $\phi_2(\omega_b)$, **Figure C.2d**. With this representation, we see that the frequency is mostly stable for the $\phi_1(\omega_a)$, $\phi_1(\omega_b)$, and $\phi_2(\omega_a)$ phase locks. However, we do see an increasing trend for the $\phi_2(\omega_b)$ phase lock, which implies that these data are likely affected by the experimental phase lag during the PLL measurement and may account for error in the calculation of $\vec{p}$.

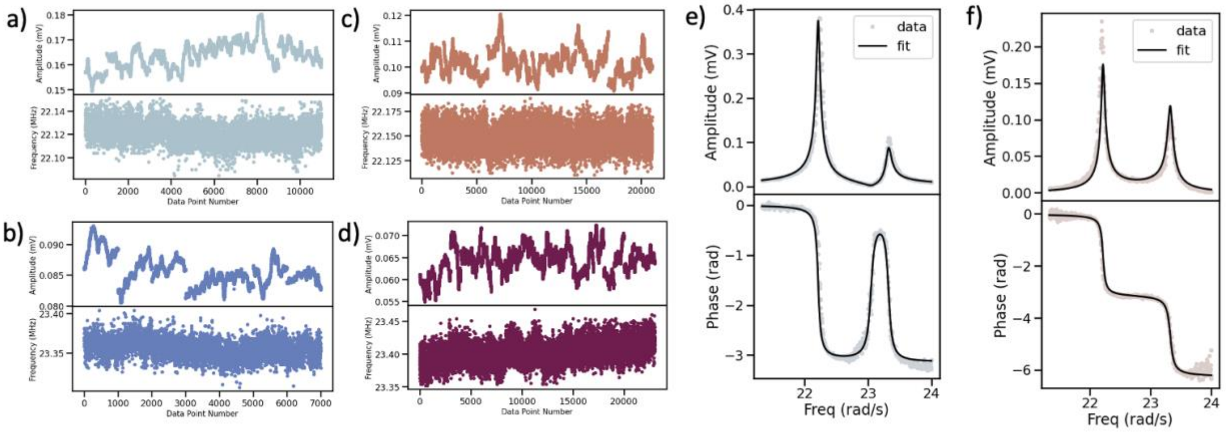

Figure C.2: Additional figures for $N = 2$ cluster

PLL measurements of amplitude and frequency plotted by data point number for corrected phase lock values of **a)** $\phi_1(\omega_a) = -0.47$ rad shown in light blue, **b)** $\phi_1(\omega_b) = -2.59$ rad shown in dark blue, **c)** $\phi_2(\omega_a) = -0.51$ rad shown in orange, **d)** $\phi_2(\omega_b) = -5.61$ rad shown in maroon. Least squares fit results shown as black solid lines over **e)** R1 amplitude (upper) and phase (lower) shown as gray data points and **f)** R1 amplitude (upper) and phase (lower) shown as light orange data points.

In the main text, we evaluate the accuracy of the NETMAP calculated $\vec{p}$ by comparing each calculated value to expected values. To estimate the expected value of the coupling strength, we start with the equation[83]

$$\Delta\omega = \sqrt{\frac{(c/m_1)(c/m_2)}{\omega_1\omega_2}}$$

In this equation, $\omega_1 = \sqrt{\frac{k_1+c}{m_1}}$, $\omega_2 = \sqrt{\frac{k_2+c}{m_2}}$, and $\Delta\omega$ is approximated to be the difference between the antisymmetric mode frequency and the symmetric mode frequency, $\Delta\omega = \omega_A - \omega_S$. We simplify this equation by assuming the two resonators have equal mass, m, and equal intrinsic spring constants, k. We then normalize by the eigenfrequency of the uncoupled resonators, $\omega_0 = \sqrt{\frac{k}{m}}$.

$$\frac{\Delta\omega}{\omega_0} = c\sqrt{\frac{1}{k(k+c)}}$$

We can then solve for c, in which we define $\Omega = \frac{\Delta\omega}{\omega_0}$,

$$c = \frac{1}{2}\left(k\Omega^2 \pm \sqrt{(k\Omega^2)^2 + (2k\Omega)^2}\right)$$

We used the `SciPy find_peaks` function in Python to estimate $\Delta\omega = 1.1$ MHz and $\omega_0 = \omega_S + \frac{\Delta\omega}{2} = 22.8$ MHz. Using these values and approximating $k = 1$ N/m, we obtain an estimate of $c = 0.05$ N/m.

To further validate NETMAP, we compare the NETMAP output parameters to those from Unity LS. The fit result of Unity LS, used for comparison in the main text, is shown as a solid black line overlayed on the experimental spectra, gray or light orange data points, in **Figure C.2e,f**.

To highlight the sensitivity of LS to input guesses, we also performed LS with increasing our input guess of the two masses from $m_1 = m_2 = 10^{-17}$ kg to 10^{-16} kg. For this fit, we saw order of magnitude or more differences in the output values of k_2, c_1, m_2, b_2, and F that do not fall within the expected ranges discussed in the main text, see **Table C.1**. While individually k_2 and m_2 are far from the expected values, the ratio of $\sqrt{\frac{k_2}{m_2}}$ gives an expected resonance frequency of ~ 16 MHz, within 7 MHz of the observed amplitude peaks. These correlated quantities, which are prevalent in our model, result in many possible solutions for least squares fitting, making this method reliant on the input guess solutions to find the residual minimum that is closest to the actual values. Combining NetMAP with LS fitting by inputting $\vec{p}$ as guess solutions (see SI for resulting $\vec{p}$ and R^2 values) may be an effective strategy to fit parameter values as close to the actual values as possible.

As a final comparison, we used LS to fit the vector weights of the two smallest singular values. In practice, we characterize the null-space dimension by the number of singular values λ such that $\lambda \ll 1$. For the $N = 1$ cluster, (**Figure 5.2**), we had only one singular value ($\lambda \sim 10^{-9}$), so the null-space was 1D. However, the $N = 2$ cluster (**Figure 5.4**) had three potential singular values ($\lambda_1 \sim 10^{-4}$, $\lambda_2 \sim 10^{-6}$, and $\lambda_3 \sim 10^{-8}$). We applied the α_i LS approach to the two smallest singular values of the $N = 2$ system and found that all output values still fall within the expected ranges and the corresponding R^2 did not change significantly, see **Table C.1**.

Mechanical Parameter	**LS with guess of $\boldsymbol{m_1 = m_2 = 10^{-16}}$kg**	$\boldsymbol{\alpha_i}$ **LS**
k_1 [N/m]	1	1
k_2 [N/m]	0.004	1.686
c_1 [N/m]	0.004	0.065
$m_1 \times 10^{-17}$[kg]	5.022	5.247
$m_2 \times 10^{-17}$[kg]	0.038	8.481
$b_1 \times 10^{-11}$ [kg/s]	1.452	2.250
$b_2 \times 10^{-11}$ [kg/s]	0.022	5.149
$F \times 10^{-6}$ [N]	0.112	1.790
R1 Amplitude R^2	-0.27	0.79
R1 Phase R^2	0.99	0.84
R2 Amplitude R^2	0.78	0.67
R2 Phase R^2	0.996	0.995

Table C.1: LS with alternate guess solutions and LS to solve for vector weights for $N = 2$ cluster

References

1. Néda, Z., Ravasz, E., Vicsek, T., Brechet, Y. & Barabási, A. L. Physics of the rhythmic applause. *Phys Rev E Stat Phys Plasmas Fluids Relat Interdiscip Topics* **61**, 6987–6992 (2000).

2. Osipov, G., Kurths, J. & Zhou, C. *Synchronization in Oscillatory Networks*. *Magnetic Phase Transitions* (Springer Berlin Heidelberg, 1983).

3. Huygens, C. The Timepiece. *Adrian Vlaqc* (1658).

4. Moiseff, A. & Copeland, J. Firefly synchrony: A behavioral strategy to minimize visual clutter. *Science (1979)* **329**, 181 (2010).

5. Winfree, A. T. Biological rhythms and the behavior of populations of coupled oscillators. *J Theor Biol* **16**, 15–42 (1967).

6. Levy, R., Hutchison, W. D., Lozano, A. M. & Dostrovsky, J. O. High-frequency synchronization of neuronal activity in the subthalamic nucleus of Parkinsonian patients with limb tremor. *Journal of Neuroscience* **20**, 7766–7775 (2000).

7. Wiesenfeld, K., Colet, P. & Strogatz, S. H. Synchronization Transitions in a Disordered Josephson Series Array. *Phys Rev Lett* **76**, 404–407 (1996).

8. Zhang, J. *et al.* Observation of a many-body dynamical phase transition with a 53-qubit quantum simulator. *Nature* **551**, 601–604 (2017).

9. Michaels, D. C., Matyas, E. P. & Jalife, J. Mechanisms of sinoatrial pacemaker synchronization: A new hypothesis. *Circ Res* **61**, 704–714 (1987).

10. Motter, A. E., Myers, S. A., Anghel, M. & Nishikawa, T. Spontaneous synchrony in power-grid networks. *Nat Phys* **9**, 191–197 (2013).

11. Skardal, P. S. & Arenas, A. Control of coupled oscillator networks with application to microgrid technologies. *Sci Adv* **1**, 1–7 (2015).

12. Chen, W. *et al.* Scalable and Programmable Phononic Network with Trapped Ions. *Nat Phys* (2023) doi:10.1038/s41567-023-01952-5.

13. Dermott, S. F. How Mercury got its spin. *Nature* **429**, 814–815 (2004).

14. Pikovsky, A. & Rosenblum, M. Dynamics of globally coupled oscillators: Progress and perspectives. *Chaos* **25**, (2015).

15. Ramana Reddy, D. V., Sen, A. & Johnston, G. L. Experimental evidence of time-delay-induced death in coupled limit-cycle oscillators. *Phys Rev Lett* **85**, 3381–3384 (2000).

16. Vladimirov, A. G., Kozyreff, G. & Mandel, P. Synchronization of weakly stable oscillators and semiconductor laser arrays. *Europhys Lett* **61**, 613–619 (2003).

17. Shim, S.-B., Imboden, M. & Mohanty, P. Synchronized Oscillation in Coupled Nanomechanical Oscillators. *Science* **316**, 95–99 (2007).

18. Matheny, M. H. *et al.* Exotic states in a simple network of nanoelectromechanical oscillators. *Science* **363**, eaav7932 (2019).

19. Doster, J., Hoenl, S., Lorenz, H., Paulitschke, P. & Weig, E. M. Collective dynamics of strain-coupled nanomechanical pillar resonators. *Nat Commun* **10**, 5246 (2019).

20. Hatanaka, D., Darras, T., Mahboob, I., Onomitsu, K. & Yamaguchi, H. Broadband reconfigurable logic gates in phonon waveguides. 32–34 (2017).

21. Kittel, C. *Introduction to Solid State Physics*. (Wiley & Sons, Inc., 1996).

22. Mohammadi, S. & Adibi, A. On chip complex signal processing devices using coupled phononic crystal slab resonators and waveguides. *AIP Adv* **1**, (2011).

23. Sun, C. Y., Hsu, J. C. & Wu, T. T. Resonant slow modes in phononic crystal plates with periodic membranes. *Appl Phys Lett* **97**, (2010).

24. Hatanaka, D., Bachtold, A. & Yamaguchi, H. Electrostatically Induced Phononic Crystal. *Phys Rev Appl* **11**, 1 (2019).

25. Wang, Y., Lee, J., Zheng, X.-Q., Xie, Y. & Feng, P. X.-L. Hexagonal Boron Nitride Phononic Crystal Waveguides. *ACS Photonics* (2019) doi:10.1021/acsphotonics.9b01094.

26. Cha, J. & Daraio, C. Electrical tuning of elastic wave propagation in nanomechanical lattices at MHz frequencies. *Nat Nanotechnol* **13**, 1016–1020 (2018).

27. Hatanaka, D., Mahboob, I., Onomitsu, K. & Yamaguchi, H. Phonon waveguides for electromechanical circuits. *Nat Nanotechnol* **9**, 520–524 (2014).

28. Cha, J., Kim, K. W. & Daraio, C. Experimental realization of on-chip topological nanoelectromechanical metamaterials. *Nature* **564**, 229–233 (2018).

29. Phys, A., Dong, S. & Hu, Q. Direction-reversible asymmetric transmission with tunable chiral metamaterial. **191701**, (2022).

30. Chen, Y. *et al.* Nonreciprocal Wave Propagation in a Continuum-Based Metamaterial with Space-Time Modulated Resonators. *Phys Rev Appl* **11**, 1 (2019).

31. Vodenicarevic, D., Locatelli, N., Abreu Araujo, F., Grollier, J. & Querlioz, D. A Nanotechnology-Ready Computing Scheme based on a Weakly Coupled Oscillator Network. *Sci Rep* **7**, 44772 (2017).

32. Csaba, G. & Porod, W. Coupled oscillators for computing: A review and perspective. *Appl Phys Rev* **7**, (2020).

33. Coulombe, J. C., York, M. C. A. & Sylvestre, J. Computing with networks of nonlinear mechanical oscillators. *PLoS One* **12**, 1–13 (2017).

34. Okamoto, H. *et al.* A strongly coupled Λ-type micromechanical system. *Appl Phys Lett* **108**, 1–5 (2016).

35. Faust, T., Rieger, J., Seitner, M. J., Kotthaus, J. P. & Weig, E. M. Coherent control of a classical nanomechanical two-level system. *Nat Phys* **9**, 485–488 (2013).

36. Zhang, Z. Z. *et al.* Coherent phonon dynamics in spatially separated graphene mechanical resonators. *Proc Natl Acad Sci U S A* **117**, 5582–5587 (2020).

37. Stannigel, K. *et al.* Optomechanical quantum information processing with photons and phonons. *Phys Rev Lett* **109**, 1–5 (2012).

38. Safavi-Naeini, A. H. & Painter, O. Proposal for an optomechanical traveling wave phonon-photon translator. *New J Phys* **13**, (2011).

39. Gajo, K., Schüz, S. & Weig, E. M. Strong 4-mode coupling of nanomechanical string resonators. *Appl Phys Lett* **111**, (2017).

40. Lin, S. *et al.* Realization of programmable nanomechanical lattice with both nearest-neighboring and next-nearest-neighboring couplings. *Appl Phys Lett* **117**, (2020).

41. Okamoto, H. *et al.* Coherent phonon manipulation in coupled mechanical resonators. *Nat Phys* **9**, 480–484 (2013).

42. Miller, D., Blaikie, A. & Alemán, B. J. Nonvolatile Rewritable Frequency Tuning of a Nanoelectromechanical Resonator Using Photoinduced Doping. *Nano Lett* **20**, 2378–2386 (2020).

43. Ransnas, L. A. & Motulsky, H. J. Fitting curves nonlinear regression : a practical and nonmathematical review. *FASEB J* **1**, 365–374 (1987).

44. Carter, B. *et al.* Spatial mapping and analysis of graphene nanomechanical resonator networks. *ArXiv* (2023) doi:10.48550/arXiv.2302.03680.

45. Geim, A. K. Graphene : Status and Prospects. **324**, 1530–1534 (2009).

46. Lee, C., Wei, X., Kysar, J. W. & Hone, J. Measurement of the elastic properties and intrinsic strength of monolayer graphene. *Science* **321**, 385–388 (2008).

47. Bunch, J. S. *et al.* Impermeable atomic membranes from graphene sheets. *Nano Lett* **8**, 2458–2462 (2008).

48. Frank, I. W., Tanenbaum, D. M., van der Zande, A. M. & McEuen, P. L. Mechanical properties of suspended graphene sheets. *Journal of Vacuum Science & Technology B: Microelectronics and Nanometer Structures* **25**, 2558 (2007).

49. Davidovikj, D. *et al.* Nonlinear dynamic characterization of two-dimensional materials. *Nat Commun* **8**, 1–7 (2017).

50. Mathew, J. P., Patel, R. N., Borah, A., Vijay, R. & Deshmukh, M. M. Dynamical strong coupling and parametric amplification of mechanical modes of graphene drums. *Nat Nanotechnol* **11**, 747–751 (2016).

51. De Alba, R. *et al.* Tunable phonon-cavity coupling in graphene membranes. *Nat Nanotechnol* **11**, 741–746 (2016).

52. Lee, J., LaHaye, M. D. & Feng, P. X. L. Design of strongly nonlinear graphene nanoelectromechanical systems in quantum regime. *Appl Phys Lett* **120**, (2022).

53. Weber, P., Güttinger, J., Noury, A., Vergara-Cruz, J. & Bachtold, A. Force sensitivity of multilayer graphene optomechanical devices. *Nat Commun* **7**, 1–8 (2016).

54. Shin, D. H. *et al.* Graphene nano-electromechanical mass sensor with high resolution at room temperature. *iScience* **26**, 105958 (2023).

55. Blaikie, A., Miller, D. & Alemán, B. J. A fast and sensitive room-temperature graphene nanomechanical bolometer. *Nat Commun* **10**, 4726 (2019).

56. Geim, A. K. & Novoselov, K. S. The rise of graphene. *Nat Mater* **6**, 183–191 (2007).

57. Balandin, A. A. Thermal properties of graphene and nanostructured carbon materials. *Nat Mater* **10**, 569–581 (2011).

58. Van Der Zande, A. M. *et al.* Large-scale arrays of single-layer graphene resonators. *Nano Lett* **10**, 4869–4873 (2010).

59. Wang, Z. *et al.* Scalable high yield exfoliation for monolayer nanosheets. 6–13 (2023) doi:10.1038/s41467-022-35569-8.

60. Luo, G. *et al.* Strong indirect coupling between graphene-based mechanical resonators via a phonon cavity. *Nat Commun* **9**, 3–8 (2018).

61. Kumar, M. & Bhaskaran, H. Ultrasensitive Room-Temperature Piezoresistive Transduction in Graphene-Based Nanoelectromechanical Systems. *Nano Lett* **15**, 2562–2567 (2015).

62. Dolleman, R. J. *et al.* High-Frequency Stochastic Switching of Graphene Resonators Near Room Temperature. *Nano Lett* **19**, 1282–1288 (2019).

63. Šiškins, M. *et al.* Tunable Strong Coupling of Mechanical Resonance between Spatially Separated FePS3 Nanodrums. *Nano Lett* **22**, 36–42 (2022).

64. Miller, D. & Alemán, B. Spatially resolved optical excitation of mechanical modes in graphene NEMS. *Appl Phys Lett* **115**, (2019).

65. Schmid, S., Villanueva, L. G. & Roukes, M. L. *Fundamentals of Nanomechanical Resonators*. *Fundamentals of Nanomechanical Resonators* (Springer International Publishing, 2016). doi:10.1007/978-3-319-28691-4.

66. Wah, T. Vibration of Circular Plates. *J Acoust Soc Am* **34**, 275–281 (1962).

67. Williams, K. R., Gupta, K. & Wasilik, M. Etch rates for micromachining processing **-** Part II. *Journal of Microelectromechanical Systems* **12**, 761–778 (2003).

68. De Alba, R. *et al.* Temperature-dependence of stress and elasticity in wet-transferred graphene membranes. *J Appl Phys* **123**, 1–8 (2018).

69. Barton, R. A. *et al.* Photothermal self-oscillation and laser cooling of graphene optomechanical systems. *Nano Lett* **12**, 4681–4686 (2012).

70. Metzger, C., Favero, I., Ortlieb, A. & Karrai, K. Optical self cooling of a deformable Fabry-Perot cavity in the classical limit. *Phys Rev B Condens Matter Mater Phys* **78**, 1–12 (2008).

71. Dolleman, R. J. *et al.* Optomechanics for thermal characterization of suspended graphene. *Phys Rev B* **96**, 1–8 (2017).

72. Karabacak, D., Kouh, T. & Ekinci, K. L. Analysis of optical interferometric displacement detection in nanoelectromechanical systems. *J Appl Phys* **98**, (2005).

73. De Alba, R., Wallin, C. B., Holland, G., Krylov, S. & Ilic, B. R. Absolute deflection measurements in a micro- and nano-electromechanical Fabry-Perot interferometry system. *J Appl Phys* **126**, (2019).

74. Wang, Z., Lee, J. & Feng, P. X. L. Spatial mapping of multimode Brownian motions in high-frequency silicon carbide microdisk resonators. *Nat Commun* **5**, (2014).

75. Midtvedt, D., Isacsson, A. & Croy, A. Nonlinear phononics using atomically thin membranes. *Nat Commun* **5**, 1–6 (2014).

76. Bunch, J. S. *et al.* Electromechanical resonators from graphene sheets. *Science (1979)* **315**, 490–493 (2007).

77. Ye, F., Islam, A. & Zhang, T. Ultrawide Frequency Tuning of Atomic Layer van der Waals Heterostructure Electromechanical Resonators. (2021) doi:10.1021/acs.nanolett.1c00610.

78. Karabalin, R. B., Cross, M. C. & Roukes, M. L. Nonlinear dynamics and chaos in two coupled nanomechanical resonators. *Phys Rev B Condens Matter Mater Phys* **79**, 1–5 (2009).

79. Doster, J. *et al.* Observing polarization patterns in the collective motion of nanomechanical arrays. *Nat Commun* **13**, 1–7 (2022).

80. Chaste, J. *et al.* Intrinsic Properties of Suspended MoS2on SiO2/Si Pillar Arrays for Nanomechanics and Optics. *ACS Nano* **12**, 3235–3242 (2018).

81. Zhang, Q.-H. *et al.* Graphene-Based Nanoelectromechanical Periodic Array with Tunable Frequency. *Nano Lett* (2021) doi:10.1021/acs.nanolett.1c01866.

82. Reserbat-Plantey, A. *et al.* Strain superlattices and macroscale suspension of graphene induced by corrugated substrates. *Nano Lett* **14**, 5044–5051 (2014).

83. Novotny, L. Strong coupling, energy splitting, and level crossings: A classical perspective. *Am J Phys* **78**, 1199–1202 (2010).

84. Miller, D. & Alemán, B. Shape tailoring to enhance and tune the properties of graphene nanomechanical resonators. *2d Mater* **4**, (2017).

85. Miller, D., Blaikie, A., Carter, B. & Alemán, B. Engineering the Modal Shape of Graphene Nanoelectromechanical Systems using Focused Ion Beam Milling. in *IEEE 13th Nanotechnology Materials and Devices Conference (NMDC)* (2018).

86. Ju, L. *et al.* Photoinduced doping in heterostructures of graphene and boron nitride. *Nat Nanotechnol* **9**, 348–352 (2014).

87. Kirchhof, J. N. *et al.* Tunable graphene phononic crystal. 1–29.

88. Deymier, P. A. *Acoustic metamaterials and phononic crystals*. (Springer-Verlag Berlin Heidelberg, 2013).

89. Joannopoulos, John D., Johnson, Steven G., Winn, Joshua N., Meade, R. D. *Photonic crystals: molding the flow of light*. (Princeton University Press, 2008).

90. Hopfield, J. J. Neural networks and physical systems with emergent collective computational abilities. *Proc Natl Acad Sci U S A* **79**, 2554–2558 (1982).

91. Arute, F. *et al.* Quantum supremacy using a programmable superconducting processor. *Nature* **574**, 505–511 (2019).

92. Mead, C. Neuromorphic Electronic Systems. *Proceedings of the IEEE* **78**, 1629–1636 (1990).

93. Bloch, I. Ultracold quantum gases in optical lattices. *Nat Phys* **1**, 23–30 (2005).

94. Tong, X. C. *Functional Metamaterials and Metadevices*. (Springer Nature, 2018).

95. Bilal, O. R., Foehr, A. & Daraio, C. Reprogrammable Phononic Metasurfaces. *Advanced Materials* **29**, 91125 (2017).

96. Ashwin, P. & Burylko, O. Weak chimeras in minimal networks of coupled phase oscillators. *Chaos* **25**, (2015).

97. Davidovikj, D. *et al.* Visualizing the Motion of Graphene Nanodrums. *Nano Lett* **16**, 2768–2773 (2016).

98. Taylor, J. R. *An Introduction to Error Analysis*. (University Science Books, 1997).

99. de Alba, R. *et al.* Temperature-dependence of stress and elasticity in wet-transferred graphene membranes. *J Appl Phys* **123**, 095109 (2018).

100. Barton, R. A. *et al.* High, size-dependent quality factor in an array of graphene mechanical resonators. *Nano Lett* **11**, 1232–1236 (2011).

101. de Jong, M. H. J., Wolde, M. A. ten, Cupertino, A., Steeneken, P. G. & Norte, R. A. Mechanical dissipation by substrate-mode coupling in SiN resonators. *Appl Phys Lett* **032201**, (2022).

102. Trefethen, L. N. & Bau III, D. *Numerical linear algebra*. (Society for Industrial and Applied Mathematics, 1997).

103. Kumar, A. & Mohanty, P. Autoassociative Memory and Pattern Recognition in Micromechanical Oscillator Network. *Sci Rep* **7**, 1–9 (2017).